



HAL
open science

New materials, new sensing and new manufacturing methods manufacturing methods

Luc Thorel, Jose Estaire, Stefano Muraro, Huan Wang, Tristan Quinten,
Amin Askarinejad, Zheng Li

► To cite this version:

Luc Thorel, Jose Estaire, Stefano Muraro, Huan Wang, Tristan Quinten, et al.. New materials, new sensing and new manufacturing methods manufacturing methods. D09.03, université gustave eiffel. 2022, <https://kp.project-geolab.eu/joint-research-activities/>. hal-04437913

HAL Id: hal-04437913

<https://univ-eiffel.hal.science/hal-04437913v1>

Submitted on 5 Feb 2024

HAL is a multi-disciplinary open access archive for the deposit and dissemination of scientific research documents, whether they are published or not. The documents may come from teaching and research institutions in France or abroad, or from public or private research centers.

L'archive ouverte pluridisciplinaire **HAL**, est destinée au dépôt et à la diffusion de documents scientifiques de niveau recherche, publiés ou non, émanant des établissements d'enseignement et de recherche français ou étrangers, des laboratoires publics ou privés.

Deliverable D09.03

**New materials, new sensing
and new manufacturing
methods**

**Version 0.2
26 July 2022**



GEO LAB

Project Information

Project acronym	GEOLAB	
Project title	Science for enhancing Europe's Critical Infrastructure	
Grant agreement number	101006512	
Start date / Duration	1 February 2021	48 months
Project partners	Deltares, TU Delft, ETHZ, UM/ZAG, TUDa, NGI, CEDEX, Uni Eiffel, UCAM, KPMG	

Document Information

Work Package title	JRA2: Innovation of the research infrastructure	
Deliverable title	D09.03 New materials, new sensing and new manufacturing methods	
Document type	Report	
Doc. version & WP no.	0.2	WP 09
Lead author(s)	Luc Thorel (Uni Eiffel)	
Contributing author(s)	Jose Estaire (Cedex), Stefano Muraro, Huan Wang, Tristan Quinten, Amin Askarinejad (TU Delft), Zheng Li (Uni Eiffel),	
Reviewer(s)	Sam Stanier (UCAM)	
Release date	April 2022	

Classification – This report is:

Draft
 X
 Final
 Public
 X
 Restricted
 Confidential

Revision history

Version	Release Date	Status	Distribution
0.2	13 th May 2022	Draft	Ton Peters (Deltares), Sam Stanier (UCAM)
1.0		Final	Project officer

Acknowledgment

This project has received funding from the European Union's Horizon 2020 research and innovation programme under Grant Agreement No. 101006512.



Disclaimer

This document reflects only the author's view and not those of the European Commission (EC). The EC and GEOLAB projects partners are not responsible for any use that may be made of the data and information it contains and do not accept liability for loss or damage suffered by any third party as a result of using this data and information.

Executive Summary

Materials, Sensing and Manufacturing are important parameters for developing physical models. Here the novelties in the three fields are explored, particularly concerning 3D Printing.

Before starting the redaction of this report, an inquiry has been developed, thanks to our TU Delft colleagues, and transmitted to the whole GEOLAB community for feeding the most important points to be developed. This induced the structure in three parts more or less independent.

The 1st topic “New materials for critical infrastructures” has been led by Cedex; the second one, devoted to “New sensing” was directed by TUDelft, when the third one, directed by Uni Eiffel, illustrates “3D printing or additive manufacturing for physical modelling.

CONTENTS

Executive Summary	3
1 Introduction	9
1.1 About GEOLAB	9
1.2 Joint Research Activities (JRA).....	10
2 New materials for critical infrastructures	11
2.1 Introduction	11
2.2 Capabilities for testing in the GEOLAB Network.....	12
2.3 Some examples of new materials.....	13
2.4 Procedures to test new materials.....	14
3. New sensing	15
3.1. Shape-Acceleration Array system (SAA).....	15
3.2. Miniature pore pressure transducers without pre-saturation.....	16
3.3. Multifunctional sensor: miniature pore pressure and 3 axis accelerometers.....	17
3.4. Optical fibre pore pressure sensor.....	19
3.5. Wireless sensing systems	21
3.6. Non-contact measuring by Particle Image Velocimetry (PIV) method	22
3.7 Ballast particles with triaxial accelerometer embedded – cedex track box.....	23
Improvement CTB ballast particle project	24
4 3D Printing (3DP) or Additive Manufacturing for physical modelling	25
4.1 Introduction	25
4.2 3D printing techniques.....	26
4.2.1. Binder jetting	26
4.2.2. Directed Energy Deposition (DED).....	26
4.2.3. Material extrusion	26
4.2.4. Material jetting.....	27
4.2.5. Powder Bed Fusion (PBF).....	27
4.2.6. Sheet lamination	28
4.2.7. Vat photopolymerization.....	28
4.2.8. Conclusions.....	29
4.3. Granular material printing	29
4.3.1. Study on the mechanical behaviour of granular materials	30
4.3.2. Study on the hydraulic behaviour of granular materials	40
4.3.3. Conclusion	44
4.4. Clay printing	45
4.4.1. Innovative Sample Preparation	45
4.4.2. Conclusion	49
4.4 Rock type material printing.....	50
4.4.1. Porosity and permeability	51
4.4.2. Crack propagation	52
4.4.3. Stress distribution.....	52
4.4.4. Rock joint.....	52
4.4.5. Small scale models.....	53
4.4.6. Conclusions.....	54
4.5 Concrete printing.....	55

5	Conclusion.....	57
6	Acknowledgements.....	58
7	References	58

List of Tables

Table 2-1	Secondary materials susceptible to be used in CI.....	11
Table 2-2	Experience in GEOLAB facilities with new materials.....	12
Table 4-1	Summary of grain generation methodologies investigated in Hanaor et al. (2016)	39

List of Figures

Figure 3-1.	The Shape-Acceleration Array (SAA) (http://www.geo-observations.com/shape-arrays)	16
Figure 3-2.	Druck PDCR 81 pore water pressure transducer (Cabrera, M. 2016).....	16
Figure 3-3.	P306-A pore pressure transducer	17
Figure 3-4.	Illustrations of: (a) accelerometer chip (ADXL327) and two reference orientations with respect to gravity; (b) water pressure electronic sensor (MPX4250A) and its connection to the porous stone; (c) final assembly of the mobile sensor	17
Figure 3-5.	(a) Fixed sensors' installation pattern; (b) schematic representation of the MS installation steps; (c) installation pattern of 10 MS sensors along the centreline of the LT.....	18
Figure 3-6.	Resultant acceleration and pore water pressure evolution recorded by Sensors MS03 and MS08 during one liquefaction triggering test.....	19
Figure 3-7.	Test setup, model pile and capillary tube.....	19
Figure 3-8.	Pressure optical fibres (after Pinet 2009)	19
Figure 3-9.	Results of pore pressure measurements as a function of model time. The rectangle shows the time span of pile driving.	20
Figure 3-10.	Development of excess pore pressure in the vicinity of the pile.	21
Figure 3-11.	System overview of wireless sensor network (https://shamatec.com/wireless-sensing/).....	21
Figure 3-12.	A novel high-speed wireless data acquisition system (WDAS) developed at the University of Western Australia : (a) drum centrifuge; (b) the tool table actuator; (c) WDAS units (Gaudin et al. 2009)	22
Figure 3-13.	Principles of PIV analysis (White and Take 2002)	22
Figure 3-14.	The application of PIV in the centrifuge test and typical results (Sinha et al. 2021)	23
Figure 3-15	Ballast particles instrumented with accelerometers.....	24
Figure 4-1	Comparison of industrial techniques for in terms of cost vs quantity (Hubs, 2022).....	25
Figure 4-2	Close image of the as-build material surface showing the printing layers and the unmelted particles. Interlayers are separated of a distance of 200 μm (Margerit et al., 2020).	26
Figure 4-3	Removing a finished SLS 3D printed part (Ultimaker, 2022)	27
Figure 4-4	3D printing principle with SLS (Jaber et al., 2020)	28
Figure 4-5	A model printed in resin on an SLA printer (Ultimaker, 2022)	28
Figure 4-6	Uses of AM processes (from Laverne et al., 2019)	29
Figure 4-7	The impact of particle shape on mechanical response: (a) Sketch of a triaxial test procedure; (b) the change of stress-strain response from single spheres to dimers consisting of two rigidly connected spheres; (c) the rugged, nonlinear relationship between shape and stiffness for particles made from three adjoined spheres (Miskin and Jaeger ,2013)......	30
Figure 4-8	The study on different 3D printing materials: (a) gypsum spheres; (b) photopolymer spheres; (c) Inter-particle friction testing setup; (d) Rockwell testing setup (Kittu et al. 2019).	31
Figure 4-9	The study on particle shape: (a) Photo of 3D-printed particles; (b) Triaxial test set-up; (c) Ensemble-averaged stress–strain curves at confining pressure of 80 kPa; (d) Definition of yield stress and strain; (e) Energy loss during the final conditioning (Athanassiadis et al. 2014).	32
Figure 4-10	micro-CT scanning and 3D printed Hostun sand: (a) micro-CT and image processing of sand particle; (b) real (left) and printed (right) grain; (c) 3D printed grains (Gupta et al. 2019).....	33
Figure 4-11	Oedometer test using the printed particles: (a) 3D view of the reconstructed image slack and the stress-	

strain response of oedometer test; (b) particle displacement from image analysis (Gupta et al. 2019)..... 33

Figure 4-12 PolyJet 3D printing process (Adamidis et al.2019). 34

Figure 4-13 Triaxial test results using the printed grains: (a) axial strain-stress ratio response; (b) axial strain-volumetric strain response (Adamidis et al. 2019). 34

Figure 4-14 Natural and 3D printed angular and rounded particles (Ahmed and Martinez 2021). 35

Figure 4-15 Comparison of shape factors for natural and printed grains (Ahmed and Martinez 2021). 35

Figure 4-16 Drained triaxial test results on a–d natural angular sand and e–h 3D printed angular sand (Ahmed and Martinez 2021)..... 36

Figure 4-17 Drained triaxial test results on a–d natural round sand and e–h 3D printed angular sand (Ahmed and Martinez 2021)..... 36

Figure 4-18 Printed particles of different shapes and materials in Ahmed and Martinez (2020) 36

Figure 4-19 Small-strain moduli for specimens of a, b, c spheres and d, e, f angular and rounded natural and additive manufactured particles (Ahmed and Martinez 2020) 37

Figure 4-20 Grains simulated using the FSO method (Hanaor et al. 2016) 37

Figure 4-21 Grains simulated using the CRI method (Hanaor et al. 2016) 38

Figure 4-22 Grains simulated using the DPA method (Hanaor et al. 2016)..... 38

Figure 4-23 Grains from FSO method 39

Figure 4-24 Grains from CRI method 39

Figure 4-25 Grains from DPA method..... 39

Figure 4-26 Triaxial shear behaviour of printed grains: (a) printed grains; (b) stress ratio, axial strain; (c) volume strain, axial strain (Hanaor et al. 2016)..... 40

Figure 4-27 Outline of steps used to obtain soil-like prototypes and sample measurements (Dal Ferro and Morari 2015) 40

Figure 4-28 Soil samples and hydraulic test results: (a) Three-dimensional representations of original and printed soil samples; (b) comparison of hydraulic conductivity of original and printed samples (Dal Ferro and Morari 2015). 41

Figure 4-29 Laboratory setup and printed particles for hydraulic conductivity measurements: (a) experimental setup; (b) printed particles (Adamidis et al. 2019) 41

Figure 4-30 Hydraulic conductivity measurements and its variation with scale factor: (a) hydraulic conductivity measurements; (b) comparison to the predictions of the formulas of Hazen and Kozeny-Carman (Adamidis et al. 2019). 42

Figure 4-31 The printed grains and the test setup: (a)-(d) Cumulative distributions of classical shape indices of printed grains; (e) Snapshots of printed grains; (f) Schematic of the modified TST-55 permeameter for experiments (Wei et al. 2021)..... 42

Figure 4-32 experimental water permeability coefficients as a function of porosity; (b) relations between C_{k-c} and porosity for S_0 calculated from STLs (void symbols) or volume equivalent spheres (solid symbols). Values for fibrous and granular beds, uniform spheres, and peat beds are from Li and Gu (2005), Carman (1937), and Mathvan and Viraraghavan (1992), respectively; (c) relations between porosity and water permeability coefficients with lines for the proposed equation and data points for experimental data. The color orange and purple denote natural Ottawa sand and LBS particles. The unit of c_0 is cm; (d) comparisons between experimental results and predictions of modified Kozeny-Carman equation, including two natural LBS (Taylor et al., 2017) and Ottawa sand (Schroth et al., 1996) particles..... 43

Figure 4-33 Granular particles and the test setup: (a) the four different shape particles; (b) the dry granular flow and particle-laden fluid flow test setups (Hafez et al. 2021). 43

Figure 4-34 The influence of particle shape on clogging: (a) clogging probability; (b) discharge volume; (c) bridge topology from CT scan (Hafez et al. 2021). 44

Figure 4-35. Construction of the heterogeneous model: (a) container box with the porous stone and the grid, process of placing the strings of slurries into the container and (b) Heterogeneous physical model (Garzon et al., 2015) 45

Figure 4-36 Real and discretized liquid limit field in soil sample: (a) realisation of the random field for a liquid limit whose mean is 205% and coefficient of variation is 50% with correlation lengths of 12 cm in x and y directions and 4 cm in the z direction; (b) discretisation of the liquid limit field in terms of soil type (Pua and Caicedo, 2020).... 46

Figure 4-37. 3D printer for clay slurry: (a) photograph of the experimental set-up (b) heterogeneous model constructed with the 3D clay printer (Pua and Caicedo, 2020) 46

Figure 4-38 View of the printed layer for $z = 14$ cm and the corresponding layer generated numerically (Pua and Caicedo, 2020)..... 47

Figure 4-39. Consolidation set-up using a flexible membrane (Pua and Caicedo, 2020) 47

Figure 4-40 Characterisation of the variability of the physical model: (a) set-up for measuring soil impedance with detail of needle tip; (b) set-up for measuring undrained strength (Pua and Caicedo, 2020)..... 48

Figure 4-41 Map of: (a) electrical resistivity of the heterogeneous model; (b) undrained strength of the heterogeneous model (Pua and Caicedo, 2020)..... 48

Figure 4-42 Sample characterization: (a) T-bar penetrometer and frame used for determining the undrained shear strength with depth; (b) T-bar readings with depth for the layered soil sample 49

Figure 4-43 : Different geometries built by the FDM technique of 3DP and tested by Jiang and Zhao, 2015 to characterize them mechanically. 50

Figure 4-44 : a) Compression specimens built by 3DP based on sand; b) corresponding SEM image in order to characterize the porosity of the specimens (from Gomez et al., 2019). 51

Figure 4-45 Networks of fractures obtained from 3D printing by the FDM technique (from Ishutov et al., 2014). 51

Figure 4-46 Comparison between crack propagation in a resin, in a sandstone rock, and in resin specimens built by 3DP (from Zhou et al., 2019)..... 52

Figure 4-47 Visualization of the stress distribution in slices of test specimens in photoelastic material, constructed by 3DP. An example of a heterogeneous specimen (50 x 50 5 50 mm) is shown on the right of the figure (from Ju et al., 2014). 52

Figure 4-48 A surface of a rock joint being 3DP printed (from Jiang. et al., 2016b)..... 53

Figure 4-49 Experimental apparatus: (a) Scheme; (b) real configuration (Gutierrez-Oribio et al., 2022)..... 53

Figure 4-50 Scale model built by 3DP of a tunnel. The block is printed with a gypsum-based material, and the coating is PLA (from Song et al., 2018). 54

Figure 4-51. Samples of 1cm^3 used to characterize the joint aperture “e” (top) and SEM images (bottom), from Jaber et al.(2020) 54

Figure 4-52 The rise in large-scale additive manufacturing for construction applications since the concept inception in 1997 (Buswell et al., 2018)..... 55

Figure 4-53 Yhnova, the 3D printed house under construction in Nantes (CNRS, 2022) 56

Figure 4-54 Printed and unreinforced concrete bridge on left (ETH Zurich, 2021). Artificial reef on right (XtreeE, 2017). 56

List of Abbreviations	
AI	Artificial Intelligence
CI	Critical Infrastructure
CA	Consortium Agreement
DOI	Digital Object Identifiers
DEM	Discrete Element Modeling
DMP	Data Management Plan
ERA	European Research Area
FAIR	Findable, Accessible, Interoperable and Reusable
IAB	International Advisory Board
ICT	Information and Communication Technology
IP	Intellectual Property
JIP	Joint Industry Project
JRA	Joint Research Activitie(s)
MT	Management Team
NA	Networking Activitie(s)
NG	Next Generation
PGA	Participants General Assembly
RI	Research Infrastructure
SME	Small and Medium Enterprise(s)
TA	Transnational Access
TRL	Technology Readiness Level
USP	User Select Panel

1 Introduction

1.1 About GEOLAB

The existing Critical Infrastructure (CI) of Europe in the water, energy, urban and transport sector is facing major challenges because of pressures such as climate change, extreme weather, geo-hazards, aging and increased usage in combination with pivotal changes in the CI to meet long-term societal goals (e.g. energy transition). To address these challenges, scientific research and innovative solutions are needed that can only be achieved by an interdisciplinary, cross-boundary approach and by equipping expert teams with the most advanced suite of physical research infrastructure available that allows them to work across spatial scales, explore different theories that describe the pressures and adopt innovative techniques for solutions.

The GEOLAB Research Infrastructure (RI) consists of 11 unique installations in Europe aimed to study subsurface behavior and the interaction with structural CI elements (e.g. a bridge) and the environment. The overarching aim of GEOLAB is to integrate and advance these key national research infrastructures towards a one-stop-shop of excellent physical research infrastructure for performing ground-breaking research and innovation to address challenges faced by the Critical Infrastructure of Europe.

During the Joint Research Activities (JRA), the capabilities of the integrated GEOLAB RI services are improved beyond present state-of-the-art. Topics are: (1) Harmonizing operation (2) Advancing physical modelling of the impact of climate change, aging and extreme events on CI; (3) Development of 3D-4D measurement techniques; (4) Application of new materials and new sensing techniques; (5) Data management of performed experiments for future re-use.

During Transnational Access (TA), users outside the consortium gain access to the GEOLAB installations to perform research and innovation. The scientific research community will use the enhanced capabilities of GEOLAB from the JRA to perform ground-breaking experiments. For CI managers and policy makers, the activities will result in a more comprehensive understanding of the challenges facing CI and evidence to base decision making upon. The construction industry will use GEOLAB to proof innovative solutions for the CI and so gain more leadership in the industrial and enabling technologies.

There will be close interaction with Small and Medium-sized Enterprises (SME) that develop user-friendly engineering software from numerical modelling advances which are validated in the TA projects. We will explicitly challenge SME on sensing, new materials and other niches for innovative solutions, which will have spinoff in other fields of application, contributing to the competitiveness of Europe.

Networking Activities (NA) are another core element of GEOLAB, culminating in workshops and other outreach events that foster a digital and In Real Life community, thereby providing a productive channel to communicate with different stakeholder groups.

The GEOLAB consortium is a collaboration of renowned organizations coordinated by Deltares (the Netherlands). Other consortium partners are: CEDEX Spain, NGI Norway, University of Cambridge (United Kingdom), Delft University of Technology (the Netherlands), University of Maribor (Slovenia), Technical University Darmstadt (Germany), ETH Zürich (Switzerland), Université Gustave Eiffel (France) and KPMG Future Analytics (Ireland).

More information: www.project-geolab.eu.

1.2 Joint Research Activities (JRA)

The Joint Research Activities (JRA) are an essential element of GEOLAB and contribute significantly to the declared overarching goal of the project by aiming for the following subordinate goals:

- Synergetic integration of experimental research infrastructure in the disciplines of subsurface behaviour (soil mechanics and hydrogeology), engineering (geotechnical, structural, engineering geology and environmental) and data science (ICT, advanced data analyses and virtual access)
- Improvement of physical modelling and measurements techniques beyond present state-of-the-art that allow for studying complex and interdisciplinary effects.
- Provision of guidance on and integration of data management methods (standardization); set-up of an open access database of well-documented experiments for efficient data exchange between installations and re-use of experiment data sets.

Consequently, JRAs are crucial to create synergy and stimulate innovation of the GEOLAB RI beyond present state-of-the-art. In alignment with the previously mentioned subordinate goals, JRAs comprise the following components:

- JRA1 “Guidance” improves and harmonizes the operation of our installations by conducting an inventory of the installations and development of GEOLAB user’s manual, among others.
- **JRA2 “Innovation”** enhances the capabilities of GEOLAB by: (a) advancing physical modelling of the impact of climate change, aging and extreme events on CI; (b) developing 3D-4D measurement laboratory and field techniques; (c) using new materials and applying new sensing techniques.
- JRA3 “Data management” offers virtual access to a database of performed experiments that is suitable for future re-use of data and easy comparison across installations.

GEOLAB will disseminate achievements of the JRA work packages through journals publications, national and international conferences, workshops, as well as through other communication channels such as social media, website and personal contacts. The results of JRA1 “Guidance” will be published on the project website as valuable information to potential new users, new generation (NG) researchers, other laboratories and academia. JRA2 “Innovation” will display advances of the GEOLAB infrastructure and demonstration projects that highlight the interaction between physical and numerical models and between physical models and the environment. Finally, JRA3 “Data management” offers virtual access to a database of performed experiments that will become available to all stakeholders to allow for re-use of data.

The current report on **New materials, new sensing and new manufacturing methods** contributes to **JRA2 “Innovation”**, informing the development of new investigation methods and innovative solutions based on the current challenges faced by society, RI owners and users, as well as on available technologies ready for adoption in GEOLAB facilities. New measurement techniques and transformative use of sensing networks can provide substantial advancement in experimental methods and improve the quality of the obtained data, information and results. Ultimately, high-density measurements and advances in physical modelling techniques, provide more, and possibly unexpected, insights into the behaviour of Europe's CI. The topics covered are very large, particularly if ones would include application of innovative technology, recommendations on how to test the application or how to use to enhance the GEOLAB RI. This is why the choice of the authors was to focus on three items, namely: 1) new materials, based on an inquiry done inside the GEOLAB group; 2) New sensing, using the experience of the experimentalist authors and the possible adaptability of existing sensors; 3) New manufacturing, limited to 3D Printing, which is a world by itself.

A lot of other items could have been included in such a deliverable, like smart materials, self-healing materials, Structural health monitoring, data driven maintenance, data and forecasting models, prefabricated retrofitting and nature base solution. Unfortunately, if all those topics present a real interest, it was not possible to include them in this deliverable.

2 New materials for critical infrastructures

Supervised by Jose ESTAIRE, Cedex

2.1 Introduction

Material Engineering is an Engineering branch devoted to the research in the development of new materials and their applications. New materials have been among the greatest achievements of every age and they have been central to the growth, prosperity, security, and quality of life of humans since the beginning of history. It is always new materials that open the door to new technologies and opportunities.

New materials have different properties (strength, deformability, weight, electrical properties, and resistance to heat or corrosion) very related with their chemical structure. Those properties make them valuable and useful for new applications, in this case, for new civil engineering applications.

On other hand, the use of secondary materials (considered as new materials) for critical infrastructures is aligned with the European policies of the circular economy. The valorization of secondary materials or wastes into new construction products is a good way to boost the principles of the circular economy by reducing the use of natural materials and landfilling.

Table 2-1 shows some of examples of secondary materials that can be used in Critical Infrastructures as construction materials. This list is in accordance with the European Standard Committees for aggregates (CEN/TC 154) and compiled at technical specification CEN/TS 17438 and with the Working Group 7 (WG 7-Alternative Materials) of CEN/TC 396 of Earthworks.

Table 2-1 Secondary materials susceptible to be used in CI

Group	Source	Class	Specific material
A	Construction and demolition recycling industries	A1	Reclaimed asphalt
		A2	Reclaimed concrete
		A3	Reclaimed bricks, masonry
		A4	Hydraulically bound and unbound materials
		A5	Mix of A1, A2, A3 and A4
		A6	Reclaimed railway ballast
B	Municipal solid waste incineration industry	B1	Municipal incinerator bottom ash1 (excluding fly ash) (MIBA)
		B2	Municipal incinerator fly ash (MIFA)
C	Coal power generation industry	C1a	Coal fly ash - siliceous
		C1b	Coal fly ash - calcareous
		C2	Fluidized bed combustion fly ash (FBCFA)
		C3	Boiler slag
		C4a	Coal bottom ash-siliceous
		C4b	Coal bottom ash-calcareous
		C5	Fluidized bedcombustion bottom ash (FBC bottom ash)
D	Iron and steel industry	D1	Granulated blast furnace slag (GBS) (vitrified)
		D2	Air-cooled blast furnace slag (ABS) (crystallized)
		D3	Basic oxygen furnace slag (converter slag, BOS)
		D4	Electric arc furnace slag (from carbon steel production, EAFC)
		D5	Electric arc furnace slag (from stainless/high alloy steel production, EAFS)
		D6	Secondary metallurgical slags SMS
E	Non ferrous industry	E1	Copper slag
		E2	Ferromolybdenum Slag
		E3	Zinc slag
		E4	Phosphorous slag

		E5	Lead slag
		E6	Ferrochromium slag
F	Foundry industry	F1	Foundry sand
		F2	Foundry cupola furnace slag
G	Mining and quarry industry	G1	Red coal shale Burned colliery spoil after burning
		G2	Refuse from hard coal mining (black coal shale). Unburned colliery spoil from hard coal mining
		G3	Pre-selected all-in from quarry/mining
		G4	Spent Oil Shale
H	Excavated natural materials	H1a	Tunnel arisings from hard rocks traditional method
		H1b	Tunnel arisings from hard rocks with TBM
		H1c	Tunnel arising from Soft material Slurry shield
		H1d	Tunnel arising from Soft material Earth pressure
		H2a	Dredge spoil - cohesive
		H2b	Dredge spoil - granular
		H3	Reclaimed natural soil
I	Other combustion residues	I1	Paper sludge ash
		I2	Sewage sludge incineration ash (municipal)
		I3	Biomass Ash
		I4	Oil Shale Ash
J	Miscellaneous	J1	Crushed Glass
		J2	Cement and lime kiln dust
		J3a	Shredded tyres
		J3b	Tyre bales
		J4a	FGD artificial gypsum
		J5b	Industrial artificial gypsum
J6	Marginal material (local experience)		

2.2 Capabilities for testing in the GEOLAB Network

GEOLAB testing facilities are able to test these new materials to fulfill the past and new requirements of Critical Infrastructures, as shown in Table 2-2 that collects the experience in this field.

Table 2-2 Experience in GEOLAB facilities with new materials

Testing facility	Physical model scale	New materials
TU Delft Geotechnical centrifuge	Small	---
Schofield Centre (UCAM)	Small	---
Uni-Eiffel Geo-Centrifuge	Small	Biocalcification Bio-inspired materials Geofoam
Geo-Centrifuge (Deltares)	Small	---
Beam and Drum Centrifuge (ETH)	Small	Biocalcification Bio-inspired materials Geofoam Soil mixing
Large-scale triaxial apparatus	Small	Bio-inspired materials,

		Lightweight Expandable Clay Aggregates (LECA), Geosynthetics Geofoam, Soil mixing, Self-healing materials, Biocalcification, Saturated clays consolidated by electro-osmosis, Alternative (secondary, waste) materials
TU Delft Large Scale Geotechnical Physical Modelling Facility	Medium	---
GeoModel Container	Medium	Geosynthetics
CEDEX Track Box	Large	Prototype of new sleepers Prototype of modular slab track Innovations in Pad design Recycled ballast New materials for sub-ballast layer: LECA (lightweight expanded clay aggregates) and slug material
TUDa Geotechnical Test Pit	Large	HydroxyPropyl MethylCellulose (HPMC) Biocalcification
Geo-Test Sites	Full	---

2.3 Some examples of new materials

Geofoam is expanded polystyrene (EPS) or extruded polystyrene (XPS) manufactured into large lightweight blocks. The blocks vary in size but are often 2 m × 0.75 m × 0.75 m. The primary function of geofoam is to provide a lightweight void fill below various civil engineering structures (highway, bridge approach, embankment or parking lot). EPS Geofoam minimizes settlement on underground utilities. Geofoam is also used in much broader applications, including lightweight fill, green roof fill, compressible inclusions, thermal insulation, and (when appropriately formed) drainage.

Geofoam shares principles with geocombs (previously called ultralight cellular structures) which has been defined as "any manufactured material created by an extrusion process that results in a final product that consists of numerous open-ended tubes that are glued, bonded, fused or otherwise bundled together". The cross-sectional geometry of an individual tube typically has a simple geometric shape (circle, ellipse, hexagon, octagon, etc.) and is on the order of 25 mm across. The overall cross-section of the assemblage of bundled tubes resembles a honeycomb that gives it its name. Presently, only rigid polymers (polypropylene and PVC) have been used as geocomb material.

On other hand, **biocalcification** is a process in which calcite is formed in soil or civil structures due to action of microbes, especially urease-producing organisms. This phenomenon, known as microbiologically induced calcite precipitation (MICP), is dependent on the urease enzyme activity, and a large number of soil microorganisms are found to contribute to the process. Undesirable effects of biofilm formation resulting in biodeterioration in civil works have gained attention and have been extensively studied. However, the calcite precipitation for strengthening cement concrete, plugging of sand, remediation of cracks in granite and ornamental stone have proved to be successful (Sarda et al., 2009).

And finally, **LECA** is a lightweight aggregate that is manufactured from clay heated in rotary kilns. During the manufacturing process, the clay expands making the grains to have a heterogeneous structure, formed by a rigid outer shell and a very porous core that gives it its characteristic lightness. Some of these voids are accessible, so they can be saturated, and others are inaccessible.

As it is a manufactured product, its characteristics (grain weight density, diameter, shell thickness) can vary depending on the specifications that are desired for the final use of the material. In civil engineering, the main applications are related to its use as a light fill in geotechnical works and in the manufacture of lightweight concrete.

LECA has been used successfully as a geotechnical fill in Europe for more than 40 years. Lehnert et al. (2004) compiled numerous cases in which this product was used in abutment fills, embankments on soft soils or fillings attached to existing embankments. Some other guides (Exca, 2015; Arlita, 2017) summarized some of the many applications of this product in geotechnical engineering. In this type of work, one of the main precautions to consider is the maximum load applied to the filling, generally not greater than 150 kPa, to limit grain breakage. Another of the main uses of LECA is the manufacture of lightweight concretes (those with a weight density lower than 2000 kg/m³ are usually considered as such (Ministerio de Fomento, 2008). Rashad (2018) compiled the main characteristics of both LECA used in concrete manufacturing and the concrete manufactured with LECA.

2.4 Procedures to test new materials

The first step in testing these new materials should be to perform the CEN standardized laboratory tests which are compulsory or recommended for the desired application. Usually, these standardized tests are focused in obtaining intrinsic characteristics of the materials, such as grain size distribution, weight density, strength, deformability and others. If the materials, either new or usual, fulfill all the CEN standard requirements it is understood these materials will have a good performance inside the civil engineering structure. So, if the “new materials” fulfill all the requirements, their use in civil engineering construction should be allowed.

However, in many cases, those standardized laboratory tests were developed for the usual materials which make them not completely suitable for these new materials. In these cases, some modifications in the laboratory procedures should be done to accommodate them to the material specific characteristics. This implies, in many cases, not to completely fulfill the standard requirements so further steps must be done.

Those second and further steps are usually to carry out what is called “performance testing” that can be defined as “the practice of evaluating how a system or a material performs in terms of responsiveness and stability under a particular workload”.

In this context, the GEOLAB testing facilities are very suitable to carry out those “performance tests” in which the new materials will be subjected to the normal working conditions. The interpretation of the test results and the comparison with tests performed with usual materials will show the capabilities of these new materials to be used in CI.

3. New sensing

Supervised by Stefano Muraro and Amin Askarinejad, Technical University of Delft.

The capability to assess the performance of critical infrastructure to anthropogenic and environmental loads through physical modelling strongly relies on accurate actuation mechanisms capable of accurately reproducing complex loading histories. At the same time, understanding the complex soil behaviour and its interaction with structures can only be achieved through the interpretation of physical quantities (e.g. forces, displacements, acceleration, pressure, strains, etc.), measured from sensors implemented in tests. In recent years, sensing techniques have been advancing significantly towards smaller, compact, integrated, wireless and non-interacting. In the following, some selected examples of innovative sensors related to different applications of physical modelling in geotechnical engineering are provided, specifically:

- **Shape arrays** are chains of rigid elements connected by flexible joints which can be instrumented with various types of sensors. Benefiting from their design, shape arrays are ideally suited for field applications where measurements over long distances are required.
- **Miniature sensors** are much smaller in size compared with their bulkier counterparts, owing to advances in silicon hardware, sensing technologies and manufacturing capabilities. These miniature sensors offer the same functionality as their bulkier counterparts and thereby offer users the possibility to minimize unwanted interaction between the sensor and the surrounding medium.
- **Multifunctional sensors** use a single casing to house several (types of) sensors. This allows measuring several physical quantities in one discrete point.
- **Fibre-optic sensors** use fibre optics technology to conduct measurements or to relay signals from a remote sensor. The signals are interpreted by an optical interrogator, which converts the signals into the appropriate physical unit. Due to their small size, high accuracy and reliable performance in challenging environments, the demand for fibre-optic sensors in the field of physical modelling is rising.
- **Wireless sensing systems** possess the same functionalities as their wired counterparts but eliminate the need to maintain a wired connection between the sensor and data acquisition system (DAQ). The possibility to transmit data wirelessly mitigates the risk of cable damage. Furthermore, it allows for more flexible sensor placement and eliminates the risk of sensor/sample disturbance due to the physical connection to the DAQ. For some physical modelling applications, the use of wireless sensing systems is therefore the preferred solution.
- **Non-contact measuring systems** allow users to measure various physical quantities without direct interaction with the object of interest. An example of this technology is Particle Image Velocimetry (PIV).
- **Ballast particles** with triaxial accelerometer embedded, a specific development from Cedex track box.

3.1. Shape-Acceleration Array system (SAA)

Zheng Li, University Gustave Eiffel.

The Shape-Acceleration Array (SAA) is a new type of sensor developed very recently (Figure 3-1). It contains an array of rigid segments separated by joints that move in any direction but do not twist. The SAA takes advantage of developments in Micro-Electro-Mechanical Systems (MEMS) technologies (Geotechnical Observations Ltd. & Measurand Inc., 2018). MEMS gravity sensors are used to measure tilt in two directions, while processors transform the position of each joint to produce shape and change of shape. This sensor array is capable of simultaneously measuring 3D ground deformations and 3D soil vibrations up to a depth of one hundred meters. The significance of the SAA is its wireless data transmission and the accuracy of the deformation measurement. The SAA is capable of measuring in situ (field) 3D ground deformation every 0.305 meters and 3D soil vibration at 2.4 m intervals. The system accuracy of the SAA can reach ± 1.5 mm per 30 m based on the study from a large number of datasets. This sensor array can be installed both vertically, similar to the traditional inclinometer casing, and horizontally. Installation and removal of SAA are extremely simple because it does not require the joining of individual sensors in the field and the single wire output from an SAA means there is very little wiring work during installation.

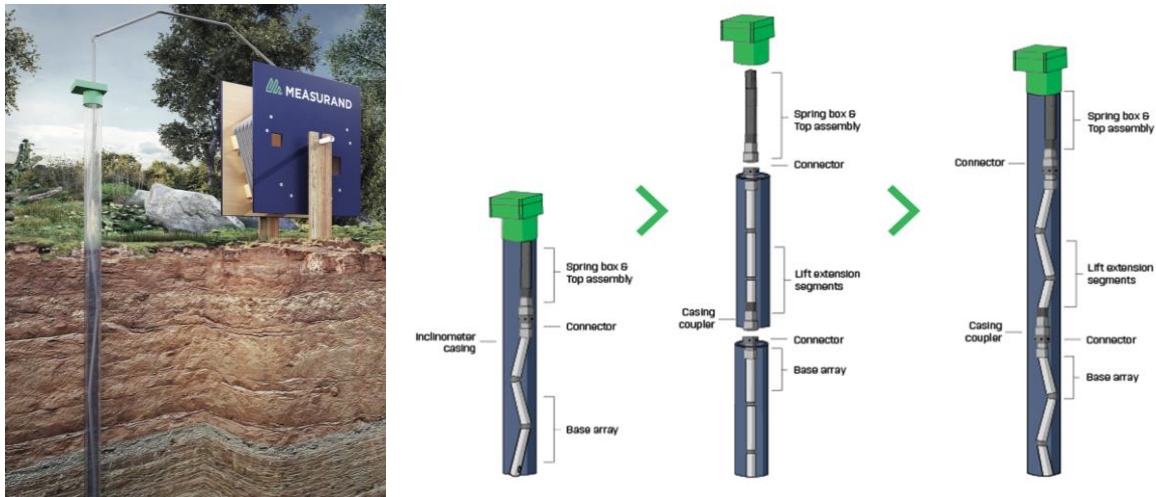


Figure 3-1. The Shape-Acceleration Array (SAA) (<http://www.geo-observations.com/shape-arrays>)

The SAA can be used in vertical, horizontal and circular orientations. For inclined and near-vertical orientations (< 60 degrees to the vertical), SAA will record three-dimensional coordinates of each joint and for horizontal arrays, settlement can be recorded. For the application in circular orientations, it can be used for measuring convergence in tunnels and sewers. SAA sensor has already been applied in the field quasi-static measurement, such as monitoring the soil deformation of the bridge abutment (Abdoun et al., 2008). SAA can also be used in measuring the dynamic response of soil movement under earthquakes (Xu et al., 2020).

3.2. Miniature pore pressure transducers without pre-saturation

Zheng Li, University Gustave Eiffel.

Over the past 30 years, the PDCR-81 (Figure 3-2) pore pressure transducer (PPT) has been a standard instrument for measuring pore pressures in centrifuge experiments.

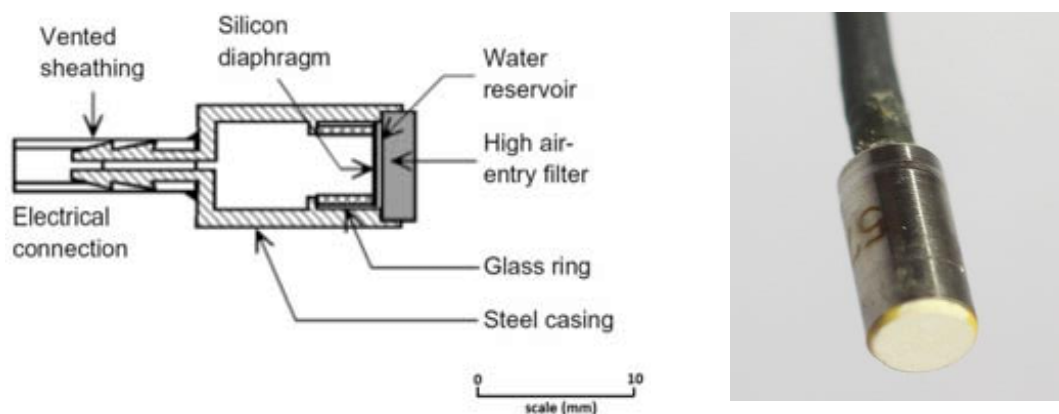


Figure 3-2. Druck PDCR 81 pore water pressure transducer (Cabrera, M. 2016)

For a typical PPT used in soil testing, a porous filter is normally realized inside the sensor to remove the influence of soil effective stresses on the recorded output. However, the response of diaphragm PPTs is affected by the presence of these filters, through which pore fluid will flow in to deflect the sensing diaphragm (Stringer et al., 2014). To reduce the influence of the filter, a perfect pre-saturation is required. However, in the large-scale test, e.g. 1g shaking table or centrifuge test, it is almost impossible to have a pre-saturation of the filters once they are instrumented in the model. Therefore, it is of great interest to develop a new type of pore-pressure sensor which requires no pre-saturation process. Recently, a double diaphragm type of pore water pressure transducer P306-A was developed by SSK, Co., Ltd. (Figure 3-3). Instead of using a porous stone as the filter, this type of pore pressure transducer uses a layer of grease to protect the sensitive measuring cell. The great advantage of this pore pressure sensor is its simplicity of use without a pre-saturation process. P306-A has been widely used for model experiments in various fields such as liquefaction tests, centrifuge tests and wave pressure measurements (Ueda et al. 2019;

Higo et al. 2015).

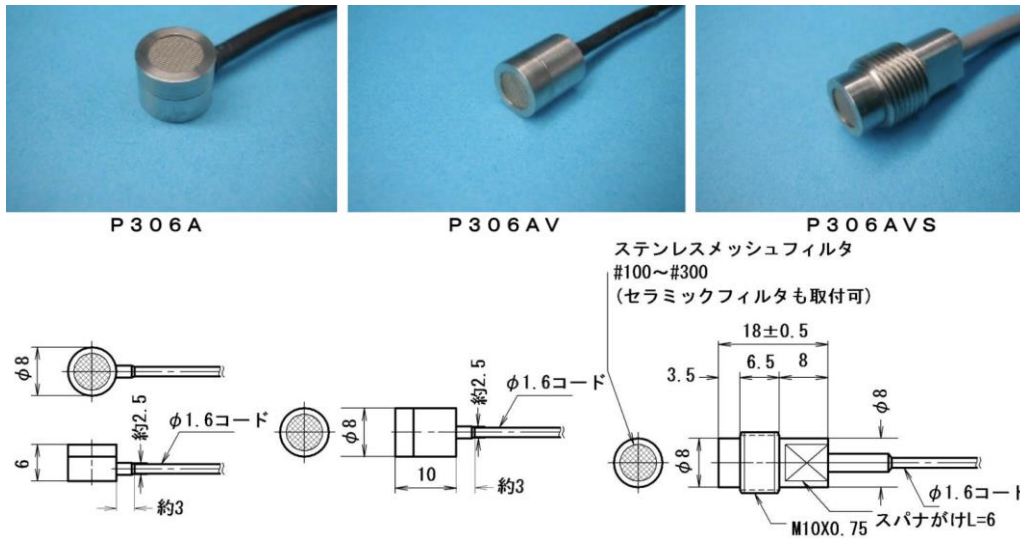


Figure 3-3. P306-A pore pressure transducer

3.3. Multifunctional sensor: miniature pore pressure and 3 axis accelerometers

Amin Askarinejad, Technical University of Delft.

Maghsoudloo et al. (2021) developed integrated miniature pore water pressure and a 3-axis accelerometer to detect the onset of static liquefaction in submerged sandy slopes. These sensors were called Mobile Sensors (MS) in this publication. The accelerometer (Figure 3-4 (a)) can record an acceleration range of $2g$ ($-1g \leq Acc \leq 1g$) $\pm 0.005g$, and the pore water pressure sensor (Figure 3-4 (b)) can measure up to 50 kPa with a resolution of ± 0.075 kPa. Figure 3-4 (c) shows a schematic view of this miniature sensor, in which the Z-direction is normal to the circular surface of the porous stone, the Y-direction is parallel to the data cable and the X-direction is perpendicular to both Y and Z.

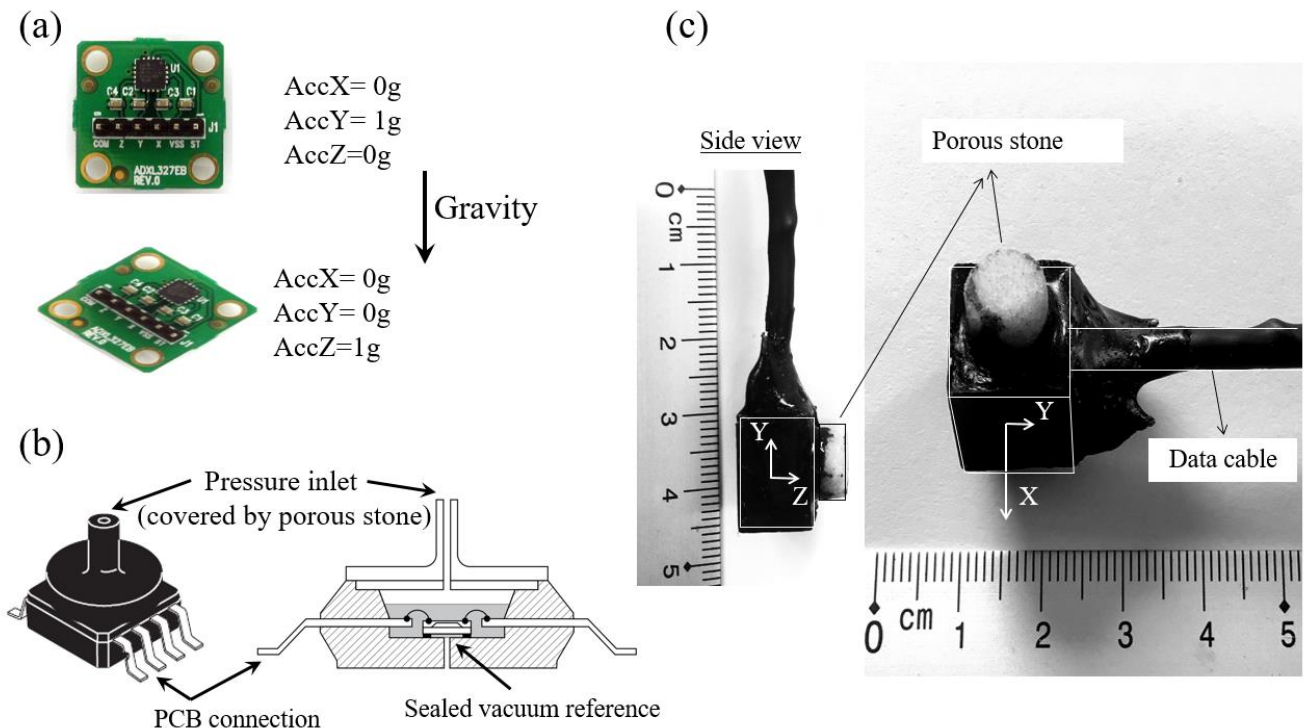


Figure 3-4. Illustrations of: (a) accelerometer chip (ADXL327) and two reference orientations with respect to gravity; (b) water pressure electronic sensor (MPX4250A) and its connection to the porous stone; (c) final assembly of the mobile sensor

- **Installation**

Figure 3-5 (b) illustrates the installation steps of the mobile sensors in the reported experiments and Figure 3-5 (c) depicts a schematic view of the implemented installation pattern. A linear installation pattern along the centreline of the liquefaction tank (LT) was selected as the one which represents the overall kinematic of the ideally plane-strain inclined flat bed with minimum boundary effects inside the LT. MS sensors were suspended above the centreline of the LT using the data cables. The length of the data cables was arranged so that they could reach the desired depth within the sand layer (e.g., the middle of the sand layer). As shown in Figure 3-5 (b) and (c), the sensors were installed above the tank before the fluidization stage and they settled down along with the soil particles when the upward flow was terminated. This method ensures a minimum disturbance in the loose sand specimen due to the installation of the sensors. It should be noted that, since the sensors were connected to flexible data cables, their location may not be exactly in the middle of the sand layer due to the possible local bending of the cable.

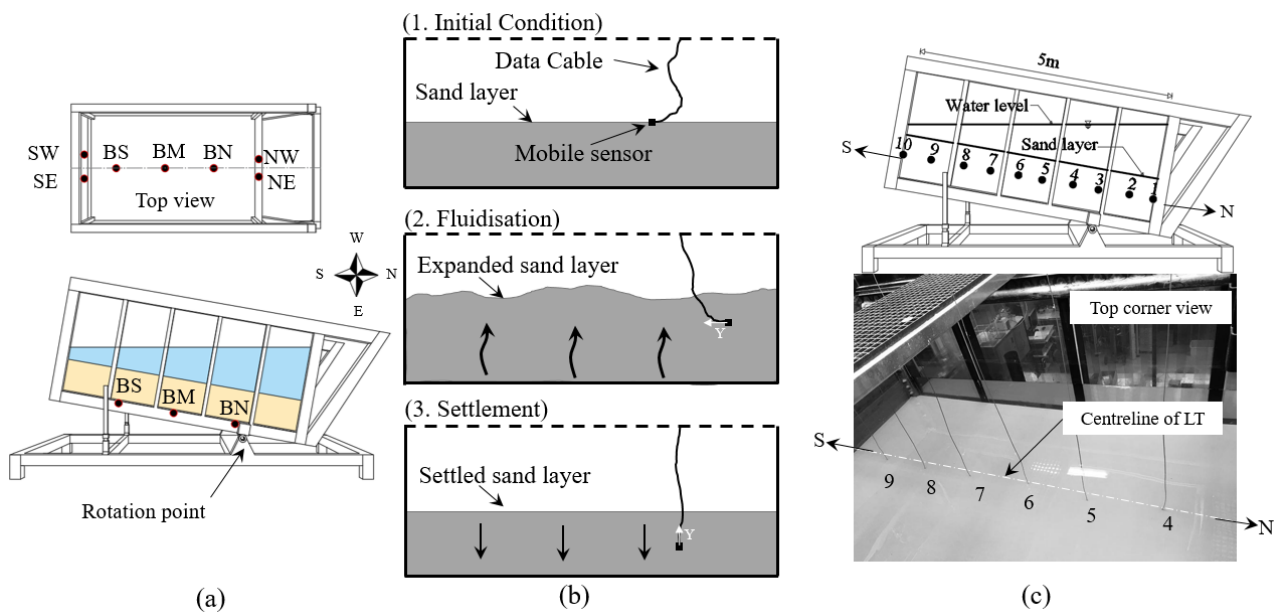


Figure 3-5. (a) Fixed sensors' installation pattern; (b) schematic representation of the MS installation steps; (c) installation pattern of 10 MS sensors along the centreline of the LT

- **Measurement results**

Figure 3-6 shows example data recorded by MS03 and MS08 in one of the liquefaction triggering tests (see Figure 3-5 (c)). Rapid large deformations at the time of failure can be indicated by an abrupt change in the acceleration data, followed by fluctuating values that indicated the occurrence of large plastic deformations and directional acceleration of the soil mass around the sensors. This figure presents additional information on the post-failure acceleration and pressure response, such as post-failure pressure fluctuations due to wave formations, post-failure large deformations, and reconsolidation phases.

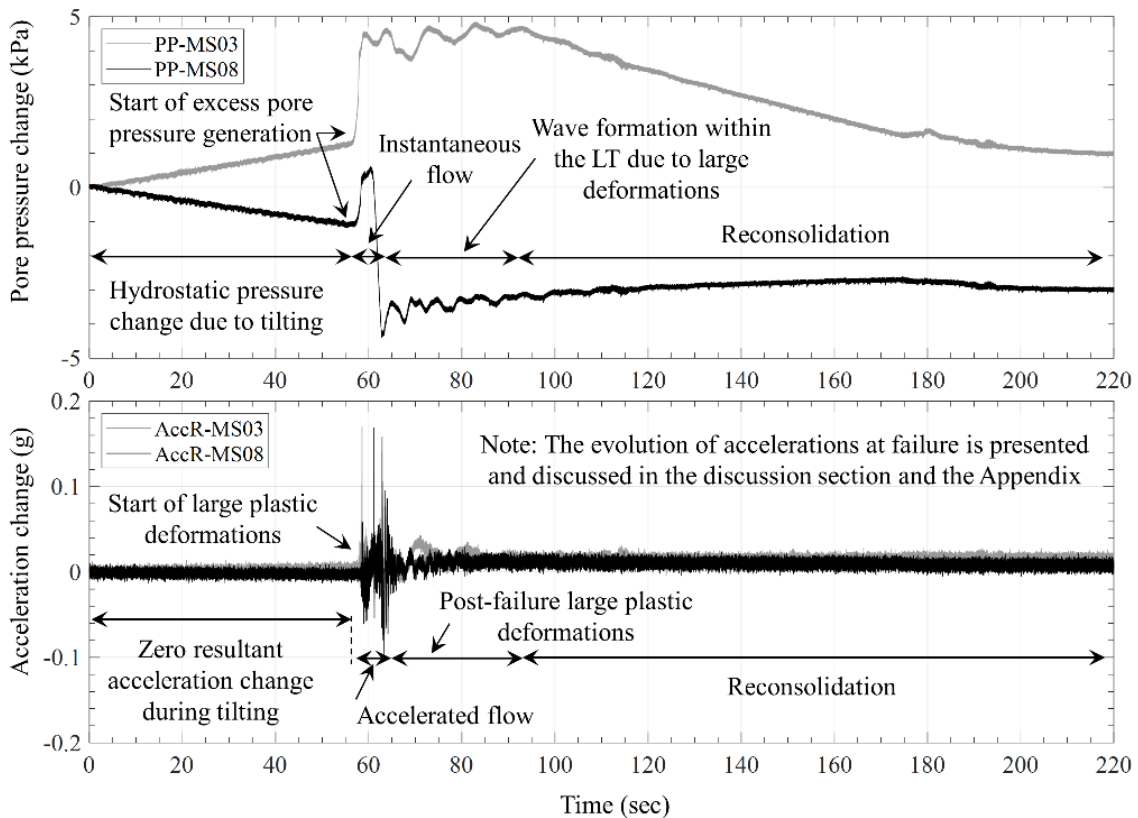
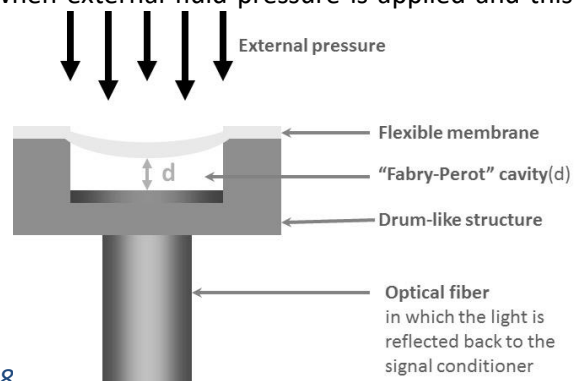


Figure 3-6. Resultant acceleration and pore water pressure evolution recorded by Sensors MS03 and MS08 during one liquefaction triggering test

3.4. Optical fibre pore pressure sensor

Amin Askarinejad, Tristan Quinten, Technical University of Delft.

Askarinejad et al. (2020) installed an optical fibre capable of measuring pore pressure changes on the outer skin of the model pile (Figure 3-7) to monitor the pore pressure generation at the pile-soil interface during impact driving. The data is complemented by standard miniature pore pressure transducers embedded in the soil mass that allow the radial distribution of excess pore pressure to be measured. The pore pressure sensor is produced by FISO and is made of a *Micro-Opto Mechanical System* (MOMS) bonded to the tip of a fibre optic (Pinet 2009). This system is composed of a deformable membrane (mechanical part) which is assembled over a cylindrical cavity. The membrane deflects towards the base of the cavity when external fluid pressure is applied and this results in a



decrease in the length of the sensing cavity (Figure 3-8

).

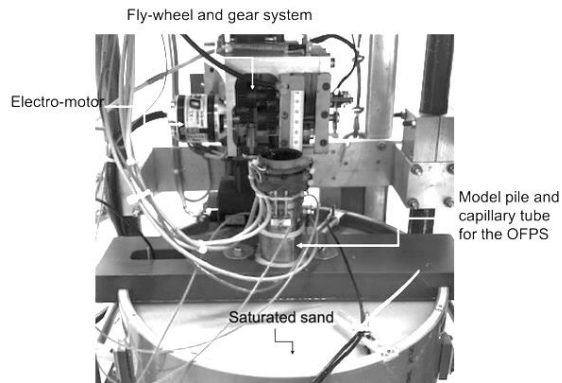


Figure 3-7. Test setup, model pile and capillary tube

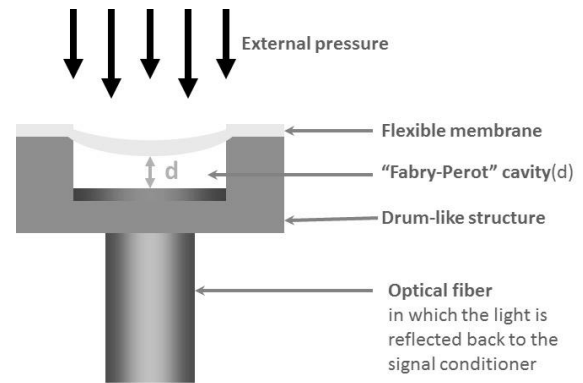


Figure 3-8. Pressure optical fibres (after Pinet 2009)

- **Installation**

Optical fibres were installed at the interface of the pile and the soil and were housed by capillary tubes (with an inner diameter of 0.8 mm). The capillary tubes were embedded into the outer periphery of the model piles. By filling the capillaries with silicon oil, and subsequently closing them off at the top with a water-resistant silicon adhesive, a closed chamber is obtained in which pressure fluctuations along the shaft can be monitored. At the bottom of the capillary, a small slit (behind which a filter is installed), allows for the transmittance of pressure from the pore fluid at the interface to the sensor. An advantage of this installation method is that the sensors follow the movement of the pile.

- **Measurement results**

To capture the development of excess pore fluid pressure during the driving operation, static pore fluid pressure sensors (SPS) are installed in the soil layer. The results of the pore pressure measurements as a function of the model time and centrifugal acceleration are presented in Figure 3-9. Both conventional and optical fibre pressure sensors were installed at similar depths with respect to the soil surface. Both sensors measure an increase in the hydro-static pressure due to the increase of centrifugal acceleration. A very good agreement is seen between the two measurements. Moreover, the decrease in the centrifugal acceleration and its effect on the hydrostatic pore pressures is very well captured by both sensors.

The optical fibre sensor shows higher values of pore pressure after installation compared to pre-installation measurements. This increase in hydro-static pore pressure indicates the added embedment of the pile. Whereas, the static PPT measures equal values before and long after the hammering. The area confined by the rectangular zone in Figure 3-9 shows the time span of pile driving and the details of the measurements in terms of excess pore pressure (EPP) development are shown in Figure 3-10. Optical sensor which is installed at the interface of the dense sand and the driven pile has measured the accumulation of negative pressures over a set of consecutive blows. At its peak, the under-pressure is about 5 kPa, equivalent to a decrease of about 10% with respect to hydrostatic conditions. Hence, it is cautiously stated that for dense sand samples as used for this research, the accumulation of positive excess pore water pressures in the vicinity of the pile is non-existent. Hence, a state of soil liquefaction seems to be ruled out in this zone. However, the limited resolution of the data logging rate inhibits the further exploration of pore pressure generation at the soil-pile interface. On the contrary, the pore pressure transducer installed with a radial distance of about 0.3 times the pile diameter measures a 30% increase in the pore pressure with respect to the initial hydro-static values pre-installation.

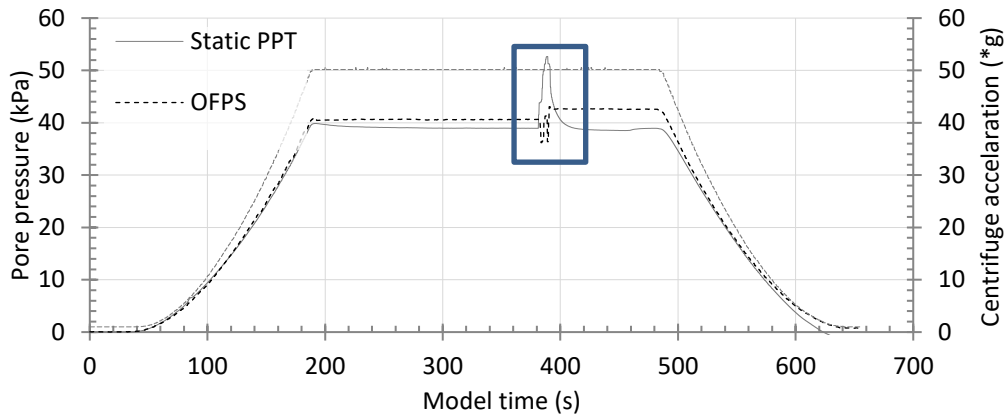


Figure 3-9. Results of pore pressure measurements as a function of model time. The rectangle shows the time span of pile driving.

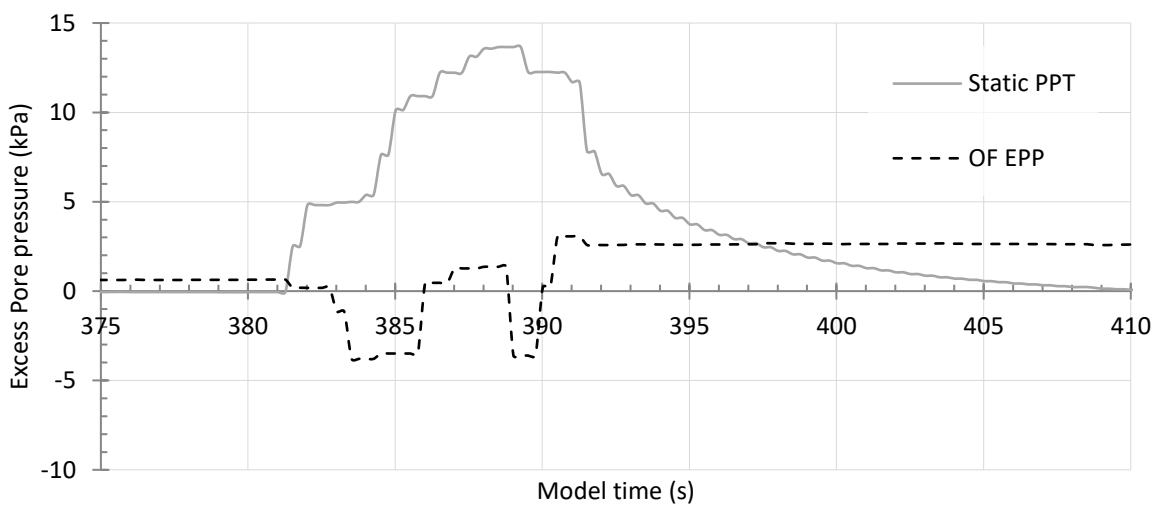


Figure 3-10. Development of excess pore pressure in the vicinity of the pile.

From a practical point of view, it could be concluded that the largest challenge lies in the area of sensor fixation and the saturation of the capillary tubes, which might tend to leak oil during the experiments. Moreover, it was observed that it would be beneficial to increase the measurement frequency of these sensors. However, it should be noted that the intrinsic data logging rate of the system used was limited to 125 Hz.

3.5. Wireless sensing systems

Zheng Li, University Gustave Eiffel.

Instruments, such as pore pressure transducers, geophones, accelerometers, settlement monitors, and inclinometers, are commonly used in geotechnical fieldwork. Traditionally, these instruments have been used with cable-based data acquisition (DAQ) systems which restrict their placement only in urban areas and construction sites. On the contrary, wireless sensing systems are compatible with many geotechnical instruments and represent an improvement over tethered DAQ by eliminating concerns about maintaining a wired connection between instruments and a global DAQ. Additionally, wireless sensors are endowed with both memory capacity and embedded data processing resources. For example, wireless sensor networks (Figure 3-11) can maintain recorded data at the node so that the data can be locally processed or held until the transmission is possible.

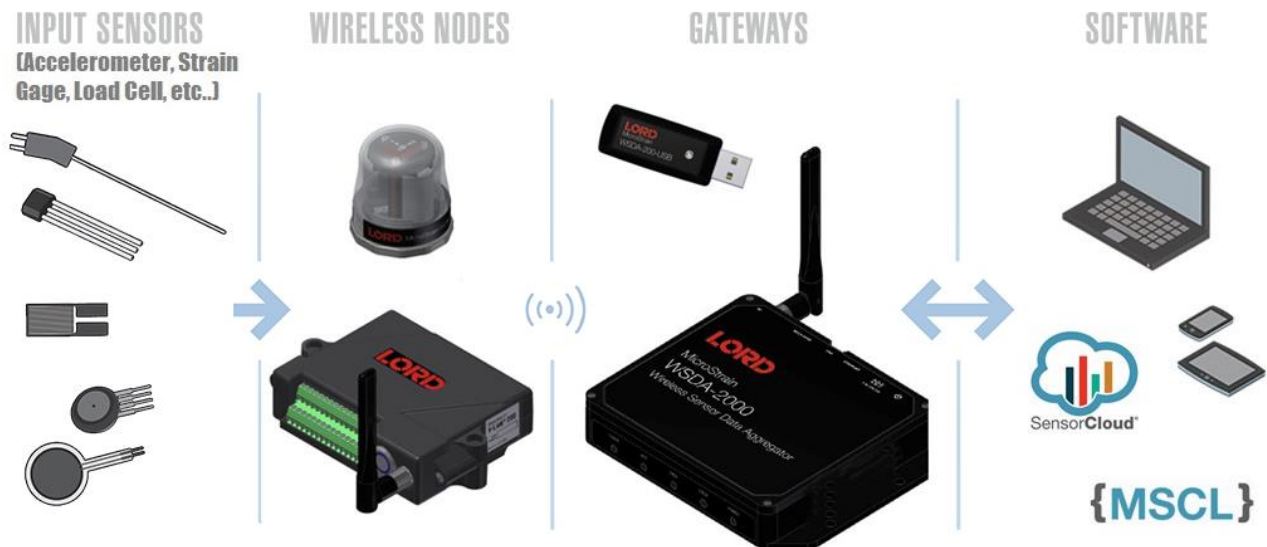


Figure 3-11. System overview of wireless sensor network (<https://shamatec.com/wireless-sensing/>)

Benefiting from their durability, economical pricing, and the previously mentioned advantages, wireless sensors have huge potential for wide use in geotechnical engineering. With a little more research and experience, it can be foreseen that the health monitoring of buried infrastructure could also become a mature area like what structural health monitoring is now. Potential applications, where wireless sensors could advance the current state of geotechnical engineering practice, include monitoring strain in buried pipelines and tunnels, recording vibrations near construction or blasting sites, measuring foundation settlement, and providing early warning of slope instability (Saftner et al., 2008).

In the field of geotechnical centrifuge test, Gaudin et al. (2009) describe a novel high-speed wireless data acquisition system (WDAS) developed at the University of Western Australia for operation onboard a geotechnical centrifuge, in an enhanced gravitational field of up to 300 times Earth's gravity. The WDAS system (Figure 3-12) consists of up to eight separate miniature units distributed around the circumference of a 0.8 m diameter drum centrifuge, communicating with the control room via wireless Ethernet. Results from a centrifuge test of a submarine landslide show good performance of the new WDAS.

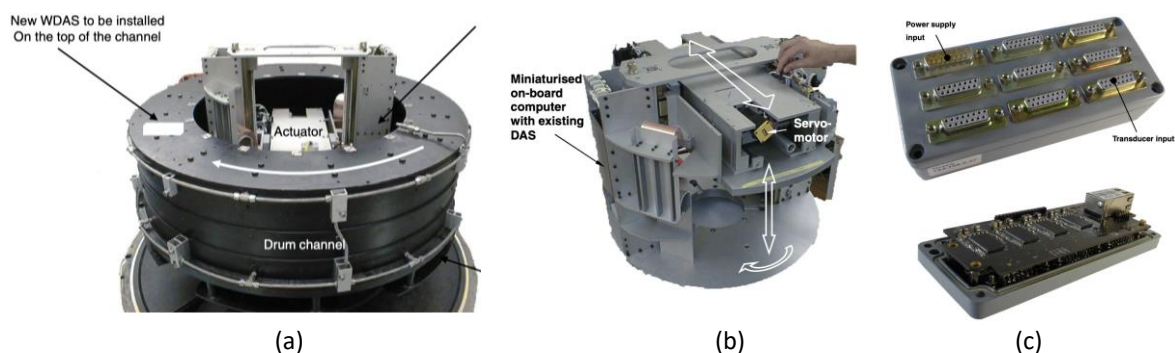


Figure 3-12. A novel high-speed wireless data acquisition system (WDAS) developed at the University of Western Australia : (a) drum centrifuge; (b) the tool table actuator; (c) WDAS units (Gaudin et al. 2009)

3.6. Non-contact measuring by Particle Image Velocimetry (PIV) method

Zheng Li, University Gustave Eiffel.

PIV is a velocity-measuring technique that was originally developed in the field of experimental fluid mechanics (Adrian, 1991). The technique was originally implemented using double-flash photography of a seeded flow. The resulting photographs contain image pairs of each seed particle. For PIV analysis, the photograph is divided into a grid of test patches. The displacement vector of each patch during the interval between the flashes is found by locating the peak of the autocorrelation function of each patch. The peak in the autocorrelation function indicates

that the two images of each seeding particle captured during the flashes are overlying each other. The correlation offset is equal to the displacement vector. The aforementioned process is illustrated in Figure 3-13.

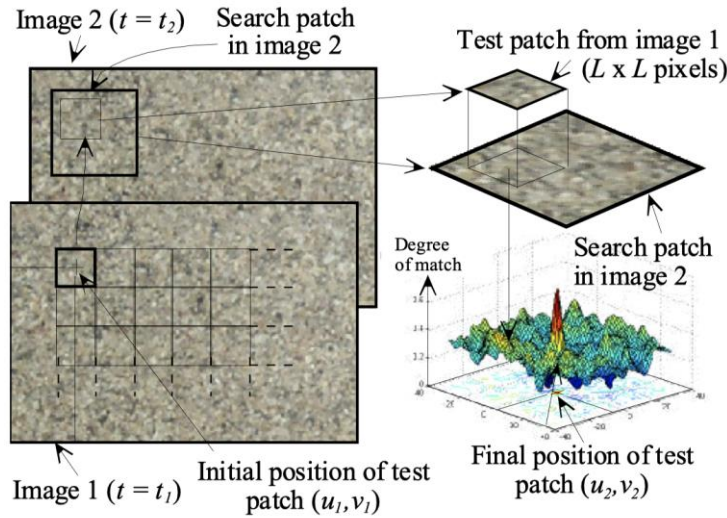
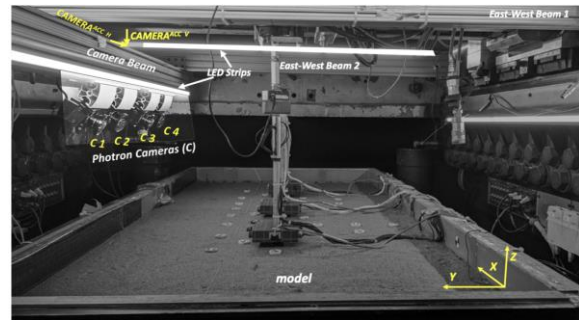
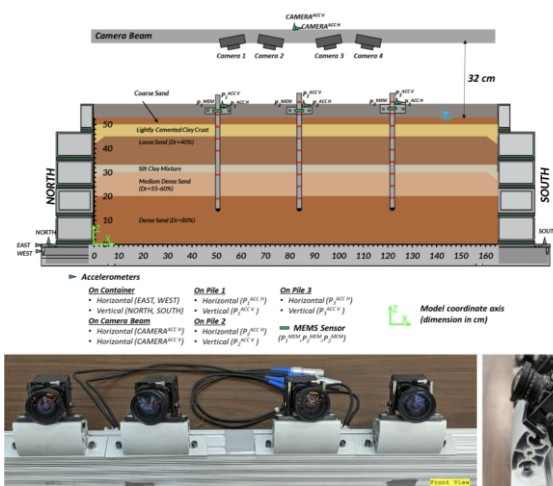


Figure 3-13. Principles of PIV analysis (White and Take 2002)

A modified approach has been used to implement PIV in geotechnical testing. Whereas fluid requires seeding with particles to create features upon which image processing can operate, natural sand has its own texture in the form of different-coloured grains and the light and shadow formed between adjacent grains when illuminated. Texture can be added to an exposed plane of clay by the addition of coloured 'flock' material or dyed sand (White et al., 2003).

PIV method can be also generalized to measure the dynamic motion of a moving system such as the vibration of structures, the movement of cars etc. Recently, for the application of PIV in the centrifuge test (Figure 3-14), Sinha *et al.* (Sinha et al., 2021) describe the first combined use of new high-speed Photron cameras and the TEMA Classic 3D software at the Center for Geotechnical Modeling (CGM) at University of California, Davis (UCD). The cameras and their mounting, as well as the target markers, lighting, camera calibration, and camera triggering, are described, followed by a discussion on the software options selected for the analysis of videos recorded in a centrifuge model test conducted on the 9 m-radius centrifuge. The results presented show that this method is effective and reliable in obtaining the positions, displacements, velocities, and accelerations of the targets.



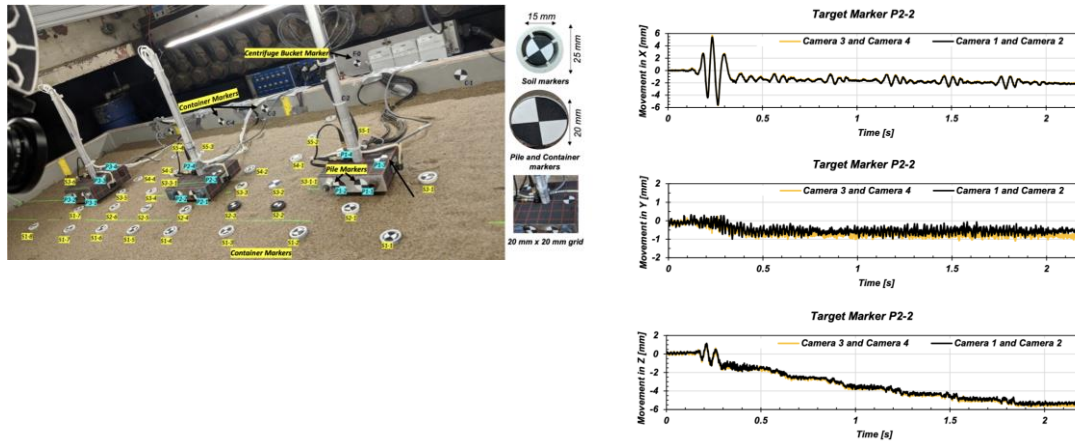


Figure 3-14. The application of PIV in the centrifuge test and typical results (Sinha et al. 2021)

3.7 Ballast particles with triaxial accelerometer embedded – cedex track box

Jose Estaire, Cedex.

Perhaps the most outstanding sensing systems at CEDEX TRACK BOX (CTB), is that one used in some ballast particles instrumented with triaxial MEMS (micro-electro-mechanical systems) accelerometers embedded.

Most of the railway track sections include a ballast layer, with an average thickness of 35 cm. These ballast particles have sizes ranging from 5 to 8 cm. The idea of transforming a ballast particle into a sensing device, such as an accelerometer, appeared at CTB as the ideal solution to measure the real accelerations of ballast particles during the pass-by of different (high) speed trains. This fact is so important, because the accelerations of ballast particles are directly related to the ballast degradation rate. This technology has been used in several in situ campaigns, as the ones performed for the European Project C4R (Capacity for Rail, 2017), and described in the Appendix 8.2 “*In-situ test campaigns in Madrid-Barcelona HSL*”.


For that reason, some CTB ballast particles were drilled, and a triaxial MEMS accelerometer was inserted, and fixed with epoxy, into each one. The three-vibration axis of the embedded accelerometer can be determined as long as the accelerometer cable is in the X-axis direction. Figure 3-15 shows two photographs with some of the ballast particles used in the tests.



Figure 3-15 Ballast particles instrumented with accelerometers

The following table summarizes the characteristics of the accelerometer embedded into each ballast particle.

characteristics of the accelerometers inserted in a ballast particle cedex track box	
Model	ADXL 335
Manufacturer	ANALOG DEVICES; www.analog.com
Accelerometer type	Capacitive. Triaxial. MEMS technology
Nominal Measurement Range	+/- 3 g

Frequency Response	0 Hz a 1600 Hz; X, Y axis 0 Hz y 550 Hz; Z axis
Bias Voltage Level	3,3 V
Nominal Sensitivity	330 mV/g (Sensitivity is ratio metric to the bias voltage level)
External conditioning	Metallic box with a 9 V battery supply and connectors for the three axis output.
	Ballast particle with the conditioning system, and all the cables: one for the direct output of the accelerometer, and other three for each vibration axis.

Improvement CTB ballast particle project

CEDEX TRACK BOX is planning to achieve a better approach for ballast particles instrumented with accelerometers. The best idea would be to have a wireless ballast particle, with no cables, so that it would be easier to install in the ballast layer.

To accomplish that, both the bias system and the transmission data system must be replaced for other systems which do not need cables. As regard the bias system, it could be substituted by a small “power pad” inserted into the ballast particle. And for the transmission data system, the best choice would be to use an “Arduino pi mini”, also inserted into the ballast particle.

4 3D Printing (3DP) or Additive Manufacturing for physical modelling

Supervised by Luc THOREL and Zheng LI, University Gustave Eiffel

4.1 Introduction

Luc THOREL and Zheng LI, University Gustave Eiffel

“3D printing, also known as additive manufacturing, is the exact opposite of the traditional way of making objects. Instead of machining or “subtracting” material to form an object - much like how a sculptor cuts away clay - 3D printing adds layer upon layer of material to build an object, but only where it’s needed. Product designers and engineers upload a digital (Computer Aid Design or CAD) file to a 3D printer, which then prints a solid 3D object. Thermoplastics are the most frequently used materials, but the technology also includes photopolymers, epoxy resins, metals, and more. Cutting-edge bioinks, which use a mixture of human cells and gelatin, have also been leveraged to 3D print complex tissue models. Even edible materials such as chocolate are being used in 3D printers.” (Stratasys, 2022)

Today, 3D printers are everywhere, for instance in the electronics (Chua et al., 2021). “Since the early 1980s, 3D printing has evolved into a global industry. Before 3D printing, product designers and artists lived in a two-dimensional world, creating designs on paper. If a 3D model was necessary, designers had to build it by assembling

parts or sculpting from blank solids. These models, also known as prototypes, were time-consuming and expensive to build. In the 1970s, CAD software emerged to improve the design process. Designers replaced tedious hand drawings with computer sketches. This saved money and time, but they still didn't have an easy way to create a model." (Pearson, 2022)

Jaber (2020) has made a review of the use of 3D printing in Rock mechanics, mentioning that "global revenues generated by 3D printing in 2012 were \$2.204 billion (Wohlers, 2013). This income is continuously growing (Wohlers, 2019). Additive manufacturing finds its place in the markets of different fields (construction of validation models for industries, construction of architectural models, construction of spare parts for some machines such as the washing machine, medical and dental field, automobile, etc. (Berman, 2012).

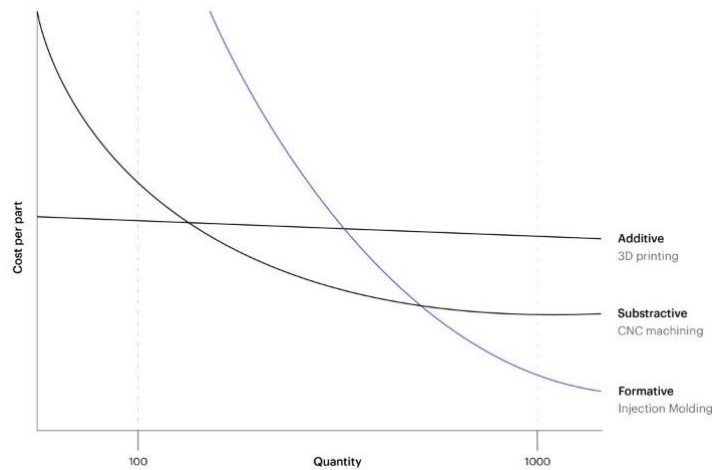


Figure 4-1 Comparison of industrial techniques for in terms of cost vs quantity (Hubs, 2022)

This growth is due to the ease and speed of the technology, as well as the variety of manufacturing processes adapted to different types of materials. We can note as an example the additive manufacturing of polymers, metals, papers and composites, plaster, and pasty materials. In the **geotechnical field**, the use of additive manufacturing remains limited. The applications of 3DP can be classified into two main families: modeling of **structures** by 3DP for study their behavior as well as the soil-structure interaction (Feng et al., 2015; Ritter et al., 2018; Stathas et al., 2018), and a modeling of **test specimens** are constructed by 3DP to characterize them mechanically and compare their behavior to that of geomaterials (small-scale physical modeling) (Cui et al., 2019, Ishibashi et al. 2019)".

4.2 3D printing techniques

Luc THOREL and Zheng LI, Université Gustave Eiffel

In the ISO standards (2015) seven process categories are identified. They are detailed below.

4.2.1. Binder jetting

Additive manufacturing process in which a liquid bonding agent is selectively deposited to join powder materials. A powder-based process similar to SLS, except that the powder is fused by a **binding agent** rather than a laser. This technique has been used among others by: Kittu et al. (2019), Sharafisafa et al. (2018), Ritter et al. (2018), Gomez et al. (2019), Braun et al., 2021.

4.2.2. Directed Energy Deposition (DED)

Additive manufacturing process in which focused thermal¹ energy is used to fuse materials by melting as they are being deposited. For instance, mechanical properties of as-printed 316L stainless steel thin-walled structures (Figure 4-2) obtained by directed energy deposition have been investigated (Margerit et al., 2020).

¹ "Focused thermal energy" means that an energy source (e.g. laser, electron beam, or plasma arc) is focused to melt the materials being deposited.

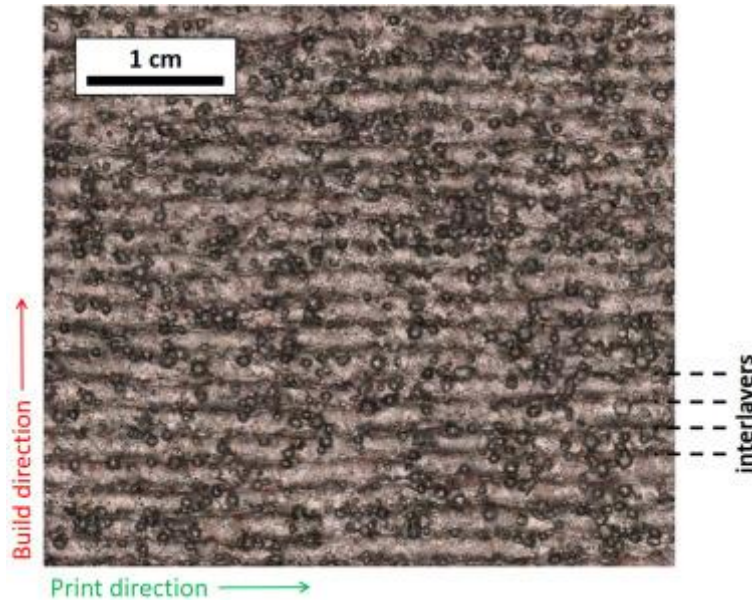


Figure 4-2 Close image of the as-build material surface showing the printing layers and the unmelted particles. Interlayers are separated of a distance of $200\ \mu\text{m}$ (Margerit et al., 2020).

4.2.3. Material extrusion

Additive manufacturing process in which material is selectively dispensed through a nozzle or orifice.

Fused deposition modeling (FDM)

“In 1988, S. Scott Crump was looking for a simpler way to make a toy frog for his daughter. Using a hot glue gun, he melted plastic and poured it into thin layers. He called the invention of Fused Deposition Modeling (FDM). His machine melted and layered plastic filaments onto a flat surface. The shape formed as the plastic cooled. He then used numerically-controlled (NC) software to automate the process. With patent in hand, Crump and his wife Lisa went on to found Stratasys. FDM® is now used in many 3D printers. » (Pearson, 2022)

Fused Filament Fabrication (FFF) is another name for FDM (Ultimaker 2022): “An FFF printer extrudes a thick string of material, commonly referred to as filament, through a heated nozzle. The nozzle is mounted on a motion system that moves it around a build area, where melted filament is deposited onto a build plate. As the material cools and solidifies, the build plate moves down by a fraction of a millimeter layer by layer until the object is complete. FFF is the most commonly used 3D printing technology, due to its ease of use and lack of reliance on harsh chemicals. FFF uses a thick string of raw material, commonly referred to as filament. Filament is a constant width of either 1.75 mm or 2.85 mm, and is typically a thermoplastic that is delivered on a spool. The FFF process extrudes the filament through a heated nozzle, which is mounted on a motion system that moves it around a build area. Melted filament from the nozzle is deposited onto a build plate, where it cools and solidifies to form a layer. The bed then moves down by a fraction of a millimeter to start another layer. The process is repeated until the complete object is formed.”

This technique has been used among others by: Song et al. (2019), Stathas et al. (2018), Zhou and Zhu (2018).

4.2.4. Material jetting

Additive manufacturing process in which droplets of build material are selectively deposited

Example materials include photopolymer and wax.

A variation on ‘2D’ inkjet printing that can create 3D parts by depositing wax or plastic material then curing it with **UV light** (Ultimaker, 2022).

PolyJet is a 3D printing technology that produces smooth, accurate parts, prototypes and tooling. With microscopic layer resolution and accuracy down to 0.014 mm, it can produce thin walls and complex geometries using the widest range of materials available with any technology (Stratasys, 2022).

This technique has been used among others by: Adamidis et al. (2018), Hanaor et al. (2016), Wei et al. (2020).

4.2.5. Powder Bed Fusion (PBF)

Additive manufacturing process in which thermal energy selectively fuses regions of a powder bed. The principle of powder bed fusion is the use of heat energy to melt a fine layer of powder previously laid down by a roller on a build plate. A review is available in Soundararajan et al. (2021).

Selective Laser Sintering (SLS)



Figure 4-3 Removing a finished SLS 3D printed part (Ultimaker, 2022)

“College student [Carl Decker](#) patented a 3D printing method using laser technology. Selective laser sintering (SLS) uses lasers to bind thermoplastic powders into a shape.” (Pearson, 2022)

“SLS 3D printing uses a powdered raw material, typically a polymer. The powder sits in a container, where a blade distributes a thin layer of material onto the build area. A laser fuses the small particles of material together to form a single horizontal layer of the part, then the container then moves a fraction of a millimeter to start a new layer, and the blade swipes across the build area to deposit a new layer of raw material. This process repeats to create the finished object.” (Ultimaker, 2022).

SLS uses high-powered CO² lasers to selectively melt and fuse powdered thermoplastics (3D systems, 2022). Jaber et al. (2020) have used this technique for rock joint printing (Figure 4-4). This technique has been used among others by: Gupta et al. (2019).

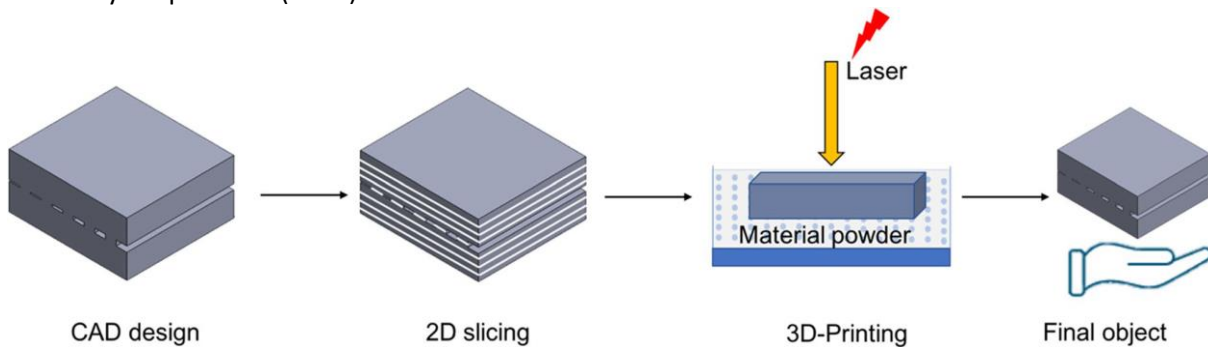


Figure 4-4 3D printing principle with SLS (Jaber et al., 2020)

Selective Laser Melting (SLM)

Metals, plastics and ceramics in powder form are melted² layer by layer by a **laser** (FuturaSciences, 2022). It is one of a few similar variations of SLS technology for metal 3D printing (Ultimaker, 2022).

Direct metal printing (DMP), also commonly known as direct metal laser sintering (DMLS), are other names for Metal applications (3D systems, 2022).

4.2.6. Sheet lamination

Additive manufacturing process in which sheets of material are bonded to form a part. It combines the addition and subtraction of material: sheets or plates of material are cut up using a cutting system (laser, cutting tool, ultra- sound, etc.), stacked and then bonded to one another (positioning, glueing, ultrasonic welding, or possibly the use of inserts, etc.) to form the product (Laverne et al. 2018).

² The distinction which exists between fusion and sintering is to do with the amount of energy supplied. In sintering, the powder is heated without reaching its melting point. The grains of powder then weld themselves to one another, which causes the layer to build.

4.2.7. Vat photopolymerization

Additive manufacturing process in which liquid photopolymer in a vat is selectively cured by light-activated polymerization (typically UV radiation from lasers or lamps).

This technique has been used among others by: Hanaor et al. (2016).

Stereolithography Apparatus (SLA)

“In 1982, Chuck Hall was a design engineer trying to solve a manufacturing problem. In an interview he explained the problem (Hull, 2013): "The process then was, you design the part, then do blueprints of the part, discuss it with a toolmaker who would make the mold for the plastic part. Then that mold would go to a molder who would inject that first part. At least six weeks later, maybe eight weeks, you would see your first part."

Hall went on to patent a design for the stereolithographic (SLA) 3D printer. He used UV light to bind polymers into layers. The light strikes a layer of polymer (a UV-curable resin) that hardens and then lowers into a bath of liquid polymer. Each layer hardens until the shape formed. » (Pearson, 2022)

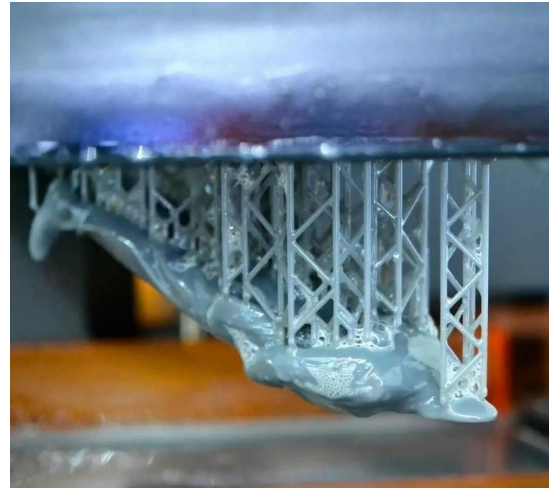


Figure 4-5 A model printed in resin on an SLA printer (Ultimaker, 2022)

The resin is poured into a glass-bottomed container, into which a build platform is submerged. A laser shines UV light on the resin to selectively harden a cross-section of the required shape. The platform gradually raises out of the container to build up the print (Ultimaker, 2022).

This technique has been used among others by: Ishibashi et al. (2020), Kittu et al. (2019), Su et al. (2020), Zhou and Zhu (2018), Zhu et al. (2018).

DLP (Direct Light Processing)

A resin-based process similar to SLA. Instead of a laser curing an individual point of resin at a time, DLP uses light to project an image of the entire layer into the resin (Ultimaker, 2022).

Continuous Liquid Interface Production (CLIP)

A liquid resin is polymerized by an ultraviolet laser in an environment where the oxygen content is controlled (FuturaSciences, 2022).

4.2.8. Conclusions

Figure 4-6 shows current uses in industry of the seven processes defined by NF ISO 17296-2 during the product development with prospects for their development over the coming years (Laverne et al., 2019).

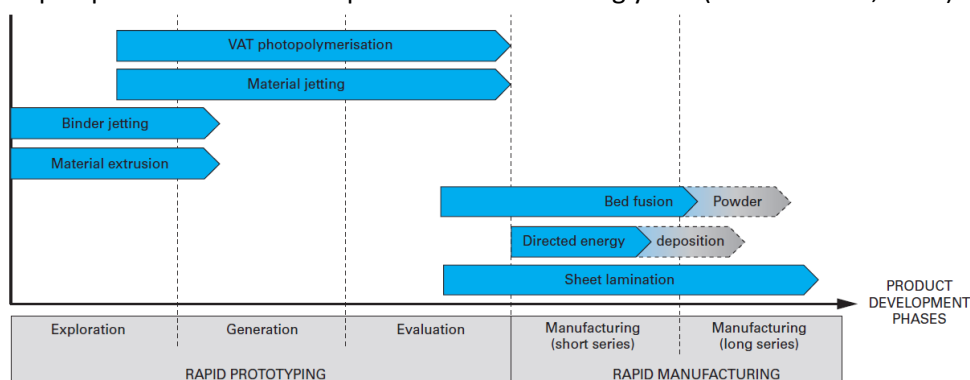


Figure 4-6 Uses of AM processes (from Laverne et al., 2019)

4.3. Granular material printing

Huan WANG, Technical University of Delft.

Understanding the micromechanical origins of the behaviour of granular materials is of increasing interest across multiple disciplines in science and engineering. In a broad range of naturally occurring granular materials, including soils, sediment particles, sand rocks and minerals, there is a need to establish better relationships between the multi-scale particle morphology of these geomaterials and their mechanical, hydrological and rheological performance (Hanaor et al., 2016). In the past years, many experimental studies have been performed to study the mechanical and hydraulic behaviour of granular materials using different natural sands (Cho et al. 2007; Lee et al., 2007; Altuhafi et al., 2013; Shin and Santamarina, 2013; Altuhafi et al., 2016; Hafez et al., 2021). However, limited by the observation techniques, it is still difficult to establish the micro-structure of granular to its bulk properties. Alternatively, the molecular dynamics (MD) or discrete element modelling (DEM) simulations provide a new investigation strategy to directly quantify the particle shape on bulk properties. However, most of the existing MD or DEM studies are limited to sphere shape particles. Recently, the improvements in the capabilities and cost-effectiveness of 3D printing technologies, combined with the availability of computational resources that permit high-resolution simulations, have made it possible to produce grain morphologies representative of real geomaterial particles in large quantities. The ability to print surrogate granular material opens the door to new research methodologies that can assist in establishing the micromechanical origins, and the role of morphology and material properties, in the behaviour of granular materials. This chapter therefore provides a comprehensive review on the existing research involving the application of 3D printing technique in the study of granular materials, including both the mechanical and hydraulic behaviour.

Pol et al. (2022) have explored the use of 3D printed grains for understanding the effect of particle shape on the kinematics and the shear-induced alignment of elongated particles in confined, heterogeneous granular flow conditions. The aim of the research is to understand the impact of particle shape on the rheology, which can be critical both in industrial and natural flows (mobility of avalanches and rockfalls). Sphero-cylindrical particles with different aspect ratios were prepared by FDM, and granular flow experiments were conducted in an annular shear cell with a rotating bottom wall and a top wall permitting confinement of the flow. The 3D printing technique allowed for preparing materials with different colors, which was useful for characterizing flow kinematics and particle orientation statistics by particle tracking using optical imaging. While translational velocity profiles were surprisingly not influenced by particle shape, rotations were found to be highly frustrated for elongated particles. In addition, a clear shear-rate dependency of the proneness of a particle to rotate is observed, with a stronger inhibition in low shear zones, which are characterized by larger relative velocity fluctuations. The orientation distributions of particles were also studied, together with the correlation of the instantaneous orientation with the angular velocity fluctuations. The richness of the results, which the authors are currently comparing to DEM simulations, witnesses of the benefits of the 3D printing technique for preparing model granular materials for laboratory testing.

4.3.1. Study on the mechanical behaviour of granular materials

Miskin and Jaeger (2013) performed a series of molecular dynamics (MD) simulations to study the influence of the particle shapes on packing stiffness. In each case, triaxial test was performed on the randomly packed particles under the same pressure from all axes, as shown in Figure 4-7 (a). To validate the finding from the MD simulations, the 3D printing technique was used to replicate the granular molecules (Figure 4-7 (b), (c)), confined and compressed under conditions similar to those of the simulations. The good agreement between the simulations and the experiments asserts that the 3D printing can be used to calibrate or validate MD simulations.

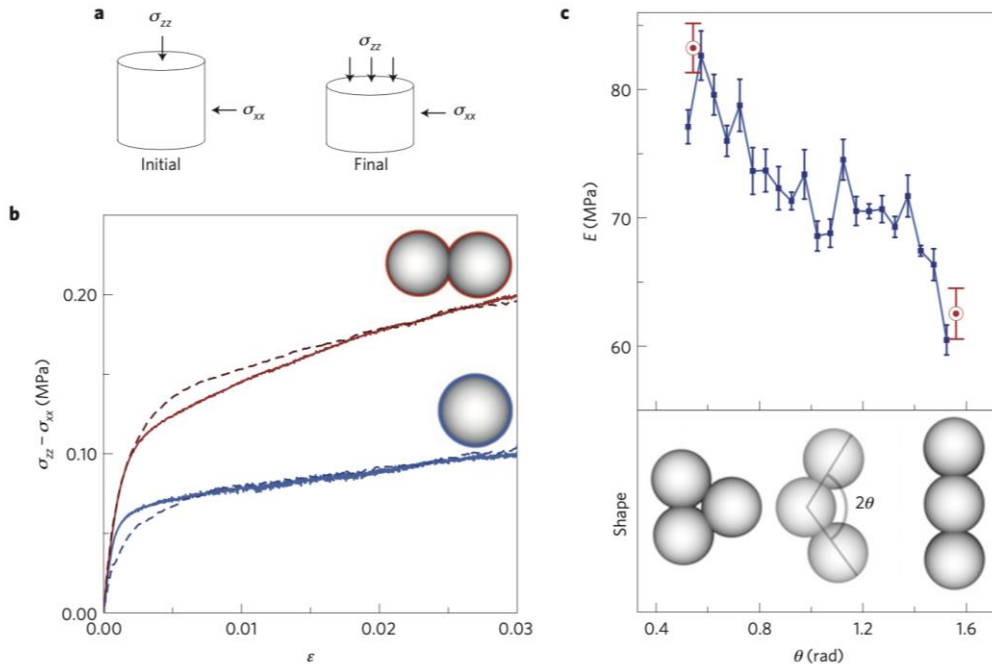
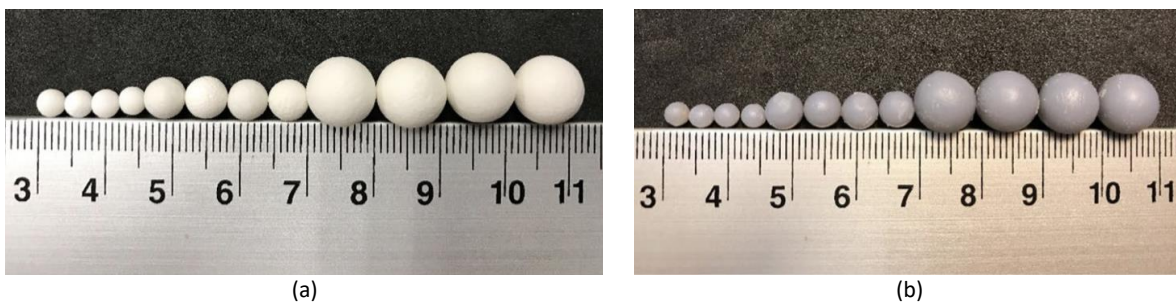


Figure 4-7 The impact of particle shape on mechanical response: (a) Sketch of a triaxial test procedure; (b) the change of stress-strain response from single spheres to dimers consisting of two rigidly connected spheres; (c) the rugged, nonlinear relationship between shape and stiffness for particles made from three adjoined spheres (Miskin and Jaeger, 2013).

Since the Additive Manufacturing (AM) technologies can be used to create 3D objects of any shape layer-by-layer, theoretically, DEM validations using a wide range of shapes and more realistically replicating natural sands and gravels can be performed using these AM particles as analogue soils. It should be noted however that the material properties of 3D printing materials are different from that of typical soil (i.e. quartz) with much smaller stiffness. In this case, characterization of the AM material is essential to ensure its suitability for laboratory testing and to determine the intrinsic material property inputs into the DEM models. Kittu et al. (2019) studied the material properties and surface characteristics of gypsum-epoxy composite (used in a binder-jetting printer) and a photopolymer resin (used in a stereolithography (SLA) system). The models of spheres and cylinders shape with different diameters were printed and tested in the inter-particle friction test and the Rockwell test as shown in Figure 4-8. Young's modulus, Poisson's ratio, shape, surface roughness, and inter-particle friction angle were measured for different material type particles. It was also found that the gypsum spheres exhibited a Hertzian behavior and the AM material is feasible for use in DEM validation studies. However, extra consideration should be given to the variability of the material properties, as discussed in Watters et al. (2017).



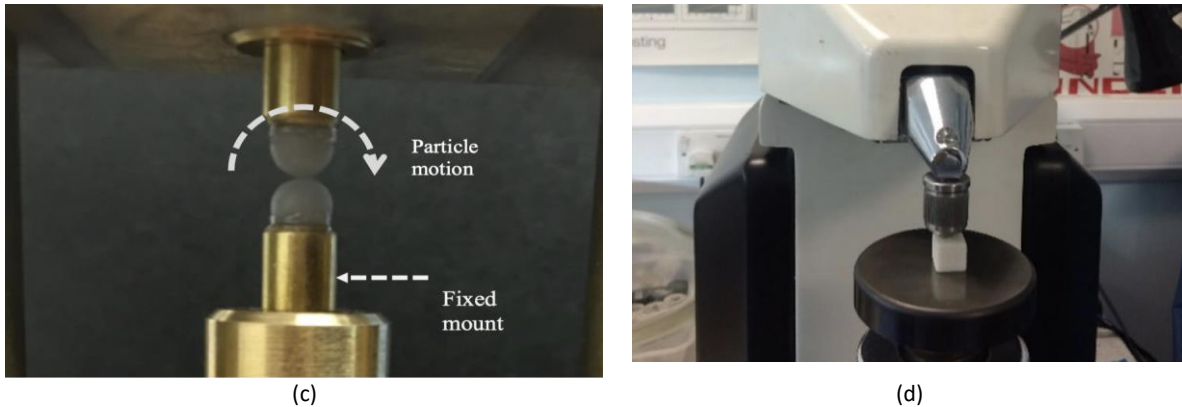
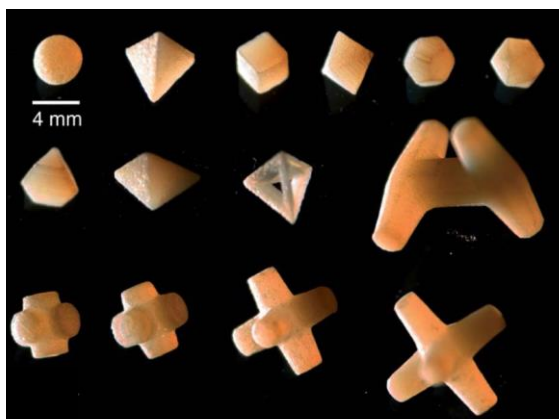


Figure 4-8 The study on different 3D printing materials: (a) gypsum spheres; (b) photopolymer spheres; (c) Inter-particle friction testing setup; (d) Rockwell testing setup (Kittu et al. 2019).

Although the Additive Manufacturing (AM) 3D technologies can produce the particles with any shape, most studies are still limited to spheres and a small set of anisotropic shapes, such as ellipsoids and rods. Recently, some progress has been made by systematically investigating the microstructural configurations of more complex shapes including faceted polyhedra. However, the particular focus was on finding the highest achievable packing fraction (Torquato and Jiao 2009; Schaller et al. 2016) instead of the mechanical behaviour. It should be also noted that those studies are all based on DEM simulations without experimental validation. To fill this gap, Athanassiadis et al. (2014) presented a comprehensive study on the stress response of packings formed from a wide range of particle shapes. Besides spheres, these also include convex shapes such as the Platonic solids, truncated tetrahedra, and triangular bipyramids, as well as more complex, non-convex geometries such as hexapods with various arm lengths, dolos, and tetrahedral frames (as shown in Figure 4-9(a)). All particles were 3D-printed on an Objet Connex 350 3D-printer, using 50 mm print resolution and a UV-cured resin (“Vero White Plus”, Objet Geometries Inc.). Well-defined initial packing states were established through preconditioning by cyclic loading under given confinement pressure. Starting from such initial states, stress–strain relationships for axial compression were obtained at four different confining pressures (i.e. 1 kPa 10 kPa, 35 kPa and 80 kPa) for each particle type. It was found that particle shape controls the details of the stress-strain curves and can be used to tune packing stiffness and yielding. For example, while cubes pack most densely under the sample preparation conditions, they exhibit a smaller initial slope and lower onset stress for yielding than the tetrahedra and octahedra (as shown in Figure 4-9(b)), which pack at lower density. Based on the experimental results, correlation of the measured values for the effective Young’s modulus under compression, yield stress and energy loss during cyclic loading with particle shape was established. This provides a set of base lines in terms of the performance that can be expected from different shapes, which can help selecting the proper particle shape for the simulation of different problems.



(a)

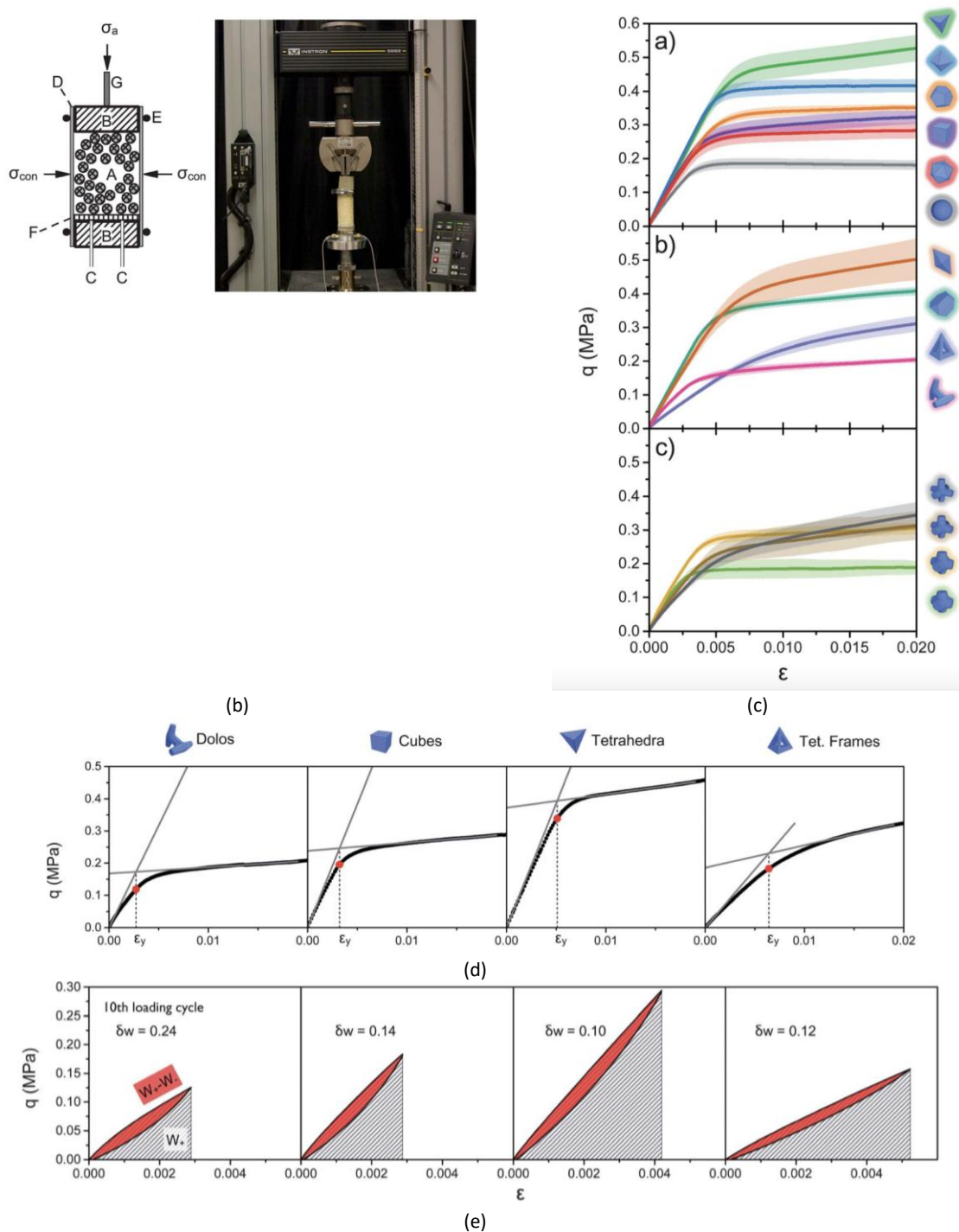


Figure 4-9 The study on particle shape: (a) Photo of 3D-printed particles; (b) Triaxial test set-up; (c) Ensemble-averaged stress–strain curves at confining pressure of 80 kPa; (d) Definition of yield stress and strain; (e) Energy loss during the final conditioning (Athanasiadis et al. 2014).

The ability to print surrogate granular material opens the door to new research methodologies that can assist in establishing the micromechanical origins, and the role of morphology and material properties, in the mechanical (Hanaor et al., 2014; Russel, 2014) and hydraulic (Frayse et al., 1999) behaviour of granular materials. For example, Gupta et al. (2019) combined the powerful micro-CT and 3D printing technique to extract particle shape features of a real sand grain and replicate it using the 3D printer. In this study, a “boxes printing” approach (Figure 4-10(c)) was used which allows to print 100 grains together in a box instead of one single particle. This approach utilizes the characteristic of SLS printing method where all grains in a box are physically separated by easily removable not sintered plastic powder resulting 100 individually separable grains in each box. The raw materials used to manufacture the synthetic particles is Polyamide 2200, a synthetic polymer commonly used for 3D printing. As shown in Figure 4-10, the surficial characteristics of a real sand grain can be well captured by the micro-CT and

replicated by the 3D printer.

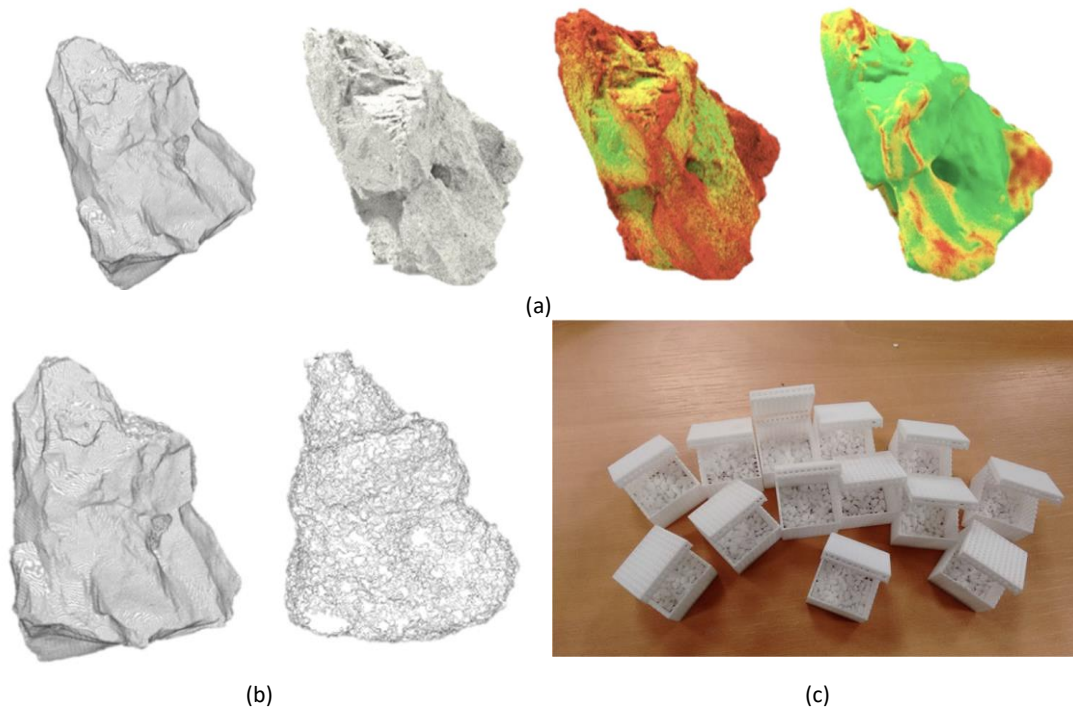


Figure 4-10 micro-CT scanning and 3D printed Hostun sand: (a) micro-CT and image processing of sand particle; (b) real (left) and printed (right) grain; (c) 3D printed grains (Gupta et al. 2019).

The oedometer tests (Figure 4-11) were then performed on a specimen composed of the printed particles of identical size and shape to create benchmark cases for calibrating and validating discrete element models. Results from digital image correlation on the synthetic sand assemblies reveal that the fracture and fragmentation of the synthetic particles are minor, which in return makes particle position tracking possible. The study proves that the 3D printing technique opens doors for modelers to design further controlled experiments using synthetic granular materials such that the individual influence of each morphological feature of granular assemblies (e.g., shape and size distribution, void ratio, fabric orientation) can be individually tested without being simultaneously affected by other variables.

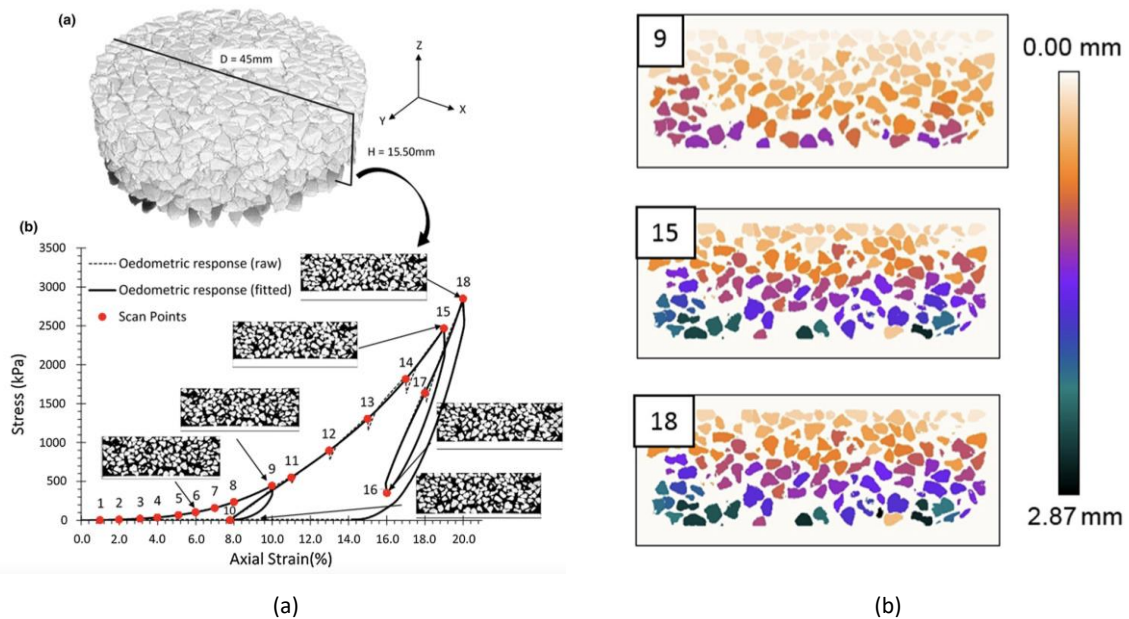


Figure 4-11 Oedometer test using the printed particles: (a) 3D view of the reconstructed image stack and the stress-strain response of oedometer test; (b) particle displacement from image analysis (Gupta et al. 2019).

To further evaluate the performance of 3D printing to create an artificial granular medium that reproduces the morphological characteristics of a natural sand, Adamidis et al. (2019) combined the microcomputed tomography (μ CT) scanning and the 3D printing technology. The 3D geometry of individual Hostun sand grains was captured first using the μ CT. The PolyJet was then employed to print the particles with the same 3D geometry. The PolyJet was selected because it provides an avenue for nonmanual support material removal using a caustic solution bath and it is quick and affordable and can thus be used to efficiently produce thousands of grains. However, it should be noted that the resolution of 40 μ m of PolyJet is insufficient for printing the scanned particles in real scale with adequate detail. Thus, scaling up was necessary. In this study, difference scaling up factor were adopted, namely 4, 8 and 16.

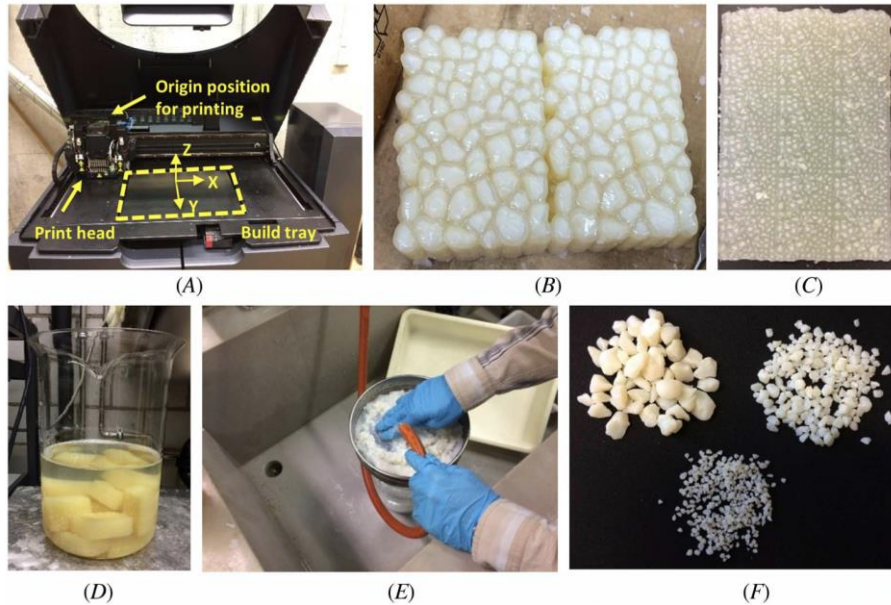


Figure 4-12 PolyJet 3D printing process (Adamidis et al. 2019).

The 3D printed grains of scaling factors 4, 8, and 16 were then subjected to drained triaxial compression tests in the specimens of 50 mm in diameter and 100 mm in height prepared by wet pluviation in de-aired water. The test for scaling factor 16 was repeated to assess whether the 3D-printed media can be reused for triaxial testing. Results of Hostun sand tested at 10 kPa (same as the printed grains) and 270 kPa of initial confinement were also included in Figure 4-13. It can be seen that the 3D printed media can capture certain aspects of Hostun sand's shear response, where the stress ratio q/p' increased to a peak before reducing toward the critical state. In terms of volumetric response, the 3D printed media exhibited a more pronounced initial contractive phase than Hostun sand but did eventually dilate as expected. This increased initial contraction was likely due to the softer material of the grains, because particle shapes and packing were not that different from the specimens of Hostun sand. In addition, it was found the mechanical response of 3D printed media at 10 kPa is closer to that of real Hostun sand at a confining stress of 270 kPa instead of 10 kPa. This suggested that maintaining the same ratio of confining stress to stiffness of grain material for the 3D printed media as for Hostun sand is critical to produced good agreement in terms of maximum friction and dilation angle, as opposed to using the same level of confinement.

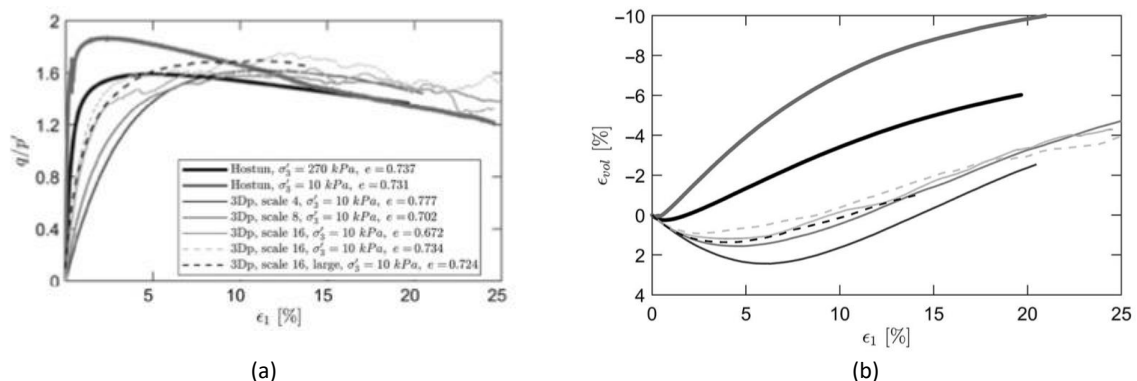


Figure 4-13 Triaxial test results using the printed grains: (a) axial strain-stress ratio response; (b) axial strain-volumetric strain response (Adamidis et al. 2019).

Adamidis et al. (2019) emphasized that applications of using 3D printing technique where particle roughness is important should be avoided because this aspect of morphology cannot be reproduced with 3D printing. In applications where material stiffness is crucial, selective laser sintering or selective laser melting 3D printing should be considered as potentially preferential to PolyJet, thanks to the availability of much stiffer materials. In applications where particle shape, roundness, and packing are of interest, PolyJet 3D printing performs well, for example, when creating experimental setups for DEM validation.

The importance of choosing the right cell pressure for replicating the real grain behaviour using the 3D printed particles was also reported in Ahmed and Martinez (2021). In this study, drained and undrained isotropically-consolidated triaxial compression tests were performed on specimens composed of angular and rounded 3D printed and natural sands, as shown in Figure 4-14 and Figure 4-15.

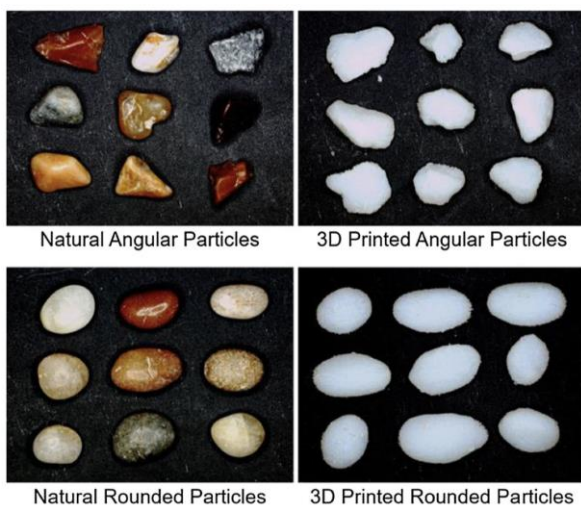


Figure 4-14 Natural and 3D printed angular and rounded particles (Ahmed and Martinez 2021).

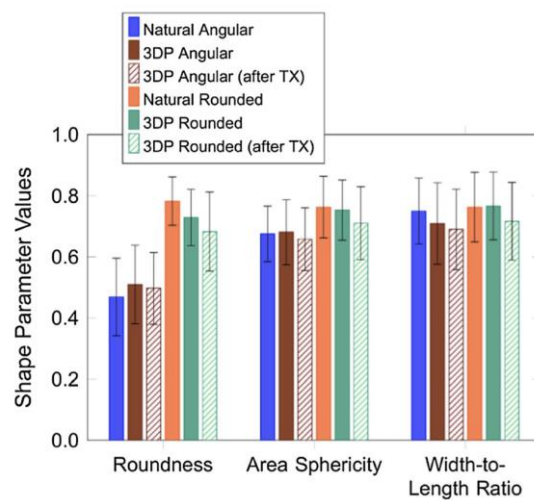


Figure 4-15 Comparison of shape factors for natural and printed grains (Ahmed and Martinez 2021).

The test results from Ahmed and Martinez (2021) indicate that the 3D printed sands exhibit stress-dilatancy behavior that follows well-established flow rules, the angular 3D printed sand mobilizes greater critical state friction angle than that of rounded 3D printed sand, and analogous drained and undrained stress paths can be followed by 3D printed and natural sands with similar initial void ratios if the cell pressure is scaled. The results suggest that some of the fundamental behaviors of soils can be captured with 3D printed soils, and that the interpretation of their mechanical response can be captured with the critical state soil mechanics framework. However, important differences in response arise from the 3D printing process and the smaller stiffness of the printed polymeric material. Same response was also observed in Ahmed and Martinez (2020).

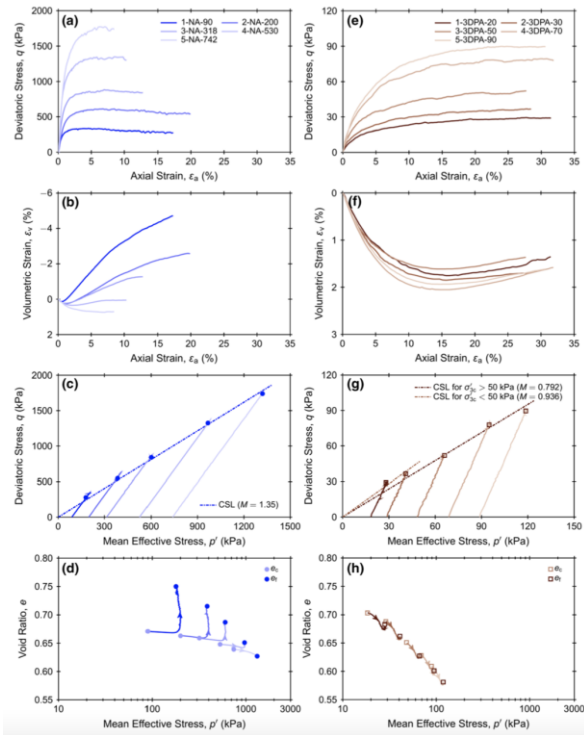


Figure 4-16 Drained triaxial test results on a–d natural angular sand and e–h 3D printed angular sand (Ahmed and Martinez 2021)

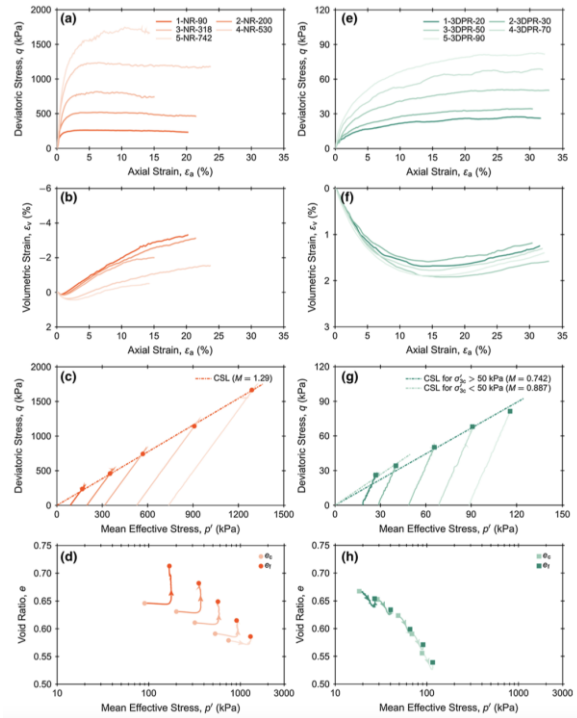


Figure 4-17 Drained triaxial test results on a–d natural round sand and e–h 3D printed angular sand (Ahmed and Martinez 2021)

Apart from the strength and volumetric response, the shear wave velocity and shear modulus are also strongly affected by the shape and material properties of the printed particles. Ahmed and Martinez (2020) performed a comprehensive of bender element tests on the 3D printed sand analogs of different shape parameters (i.e., round and angular) and material properties (i.e., steel, glass, polymer).

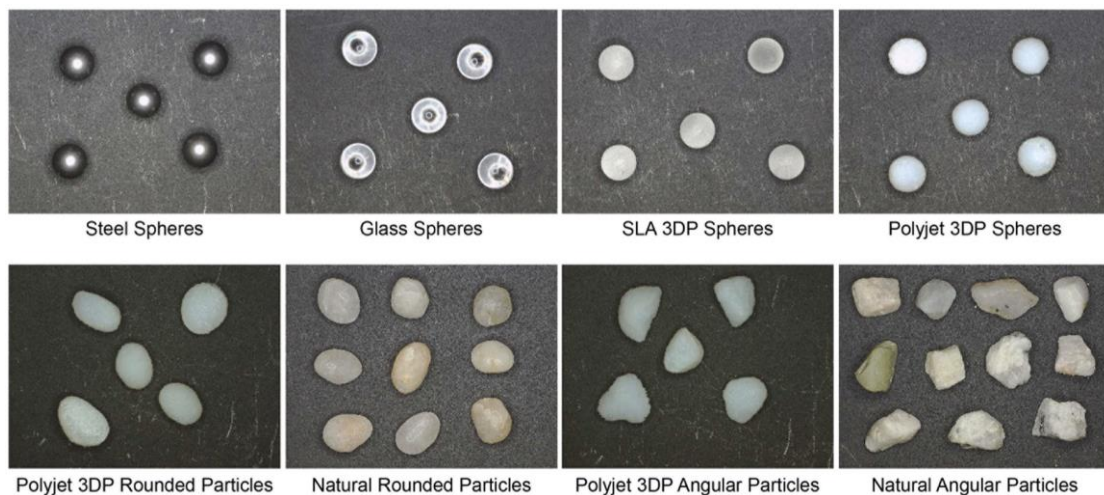


Figure 4-18 Printed particles of different shapes and materials in Ahmed and Martinez (2020)

As shown in Figure 4-19, shear wave velocity and shear modulus measurements obtained with bender elements indicate that the dependency with mean effective stress and void ratio for the 3D printed materials is similar to that of natural sands.

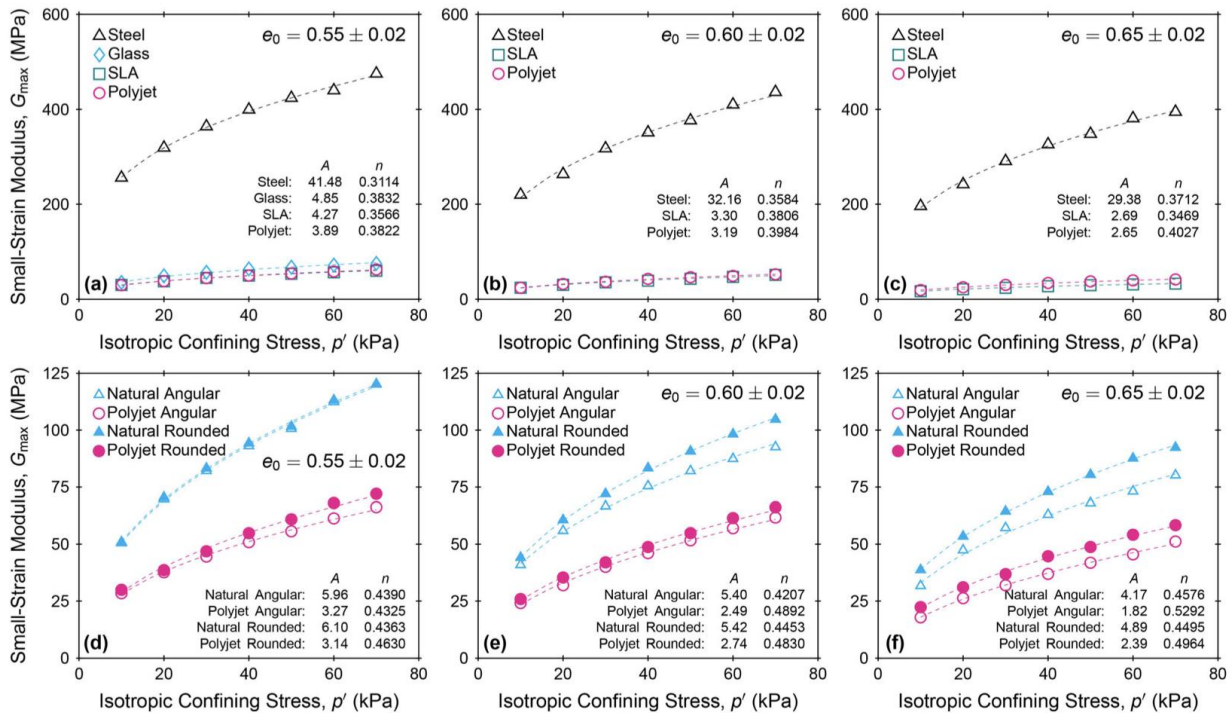


Figure 4-19 Small-strain moduli for specimens of a, b, c spheres and d, e, f angular and rounded natural and additive manufactured particles (Ahmed and Martinez 2020)

Apart from printing soil grains based on the microcomputed tomography (μ CT) scanning, the concept of printable granular geomaterials offers an avenue to “standardize” soil for quality control and calibration in geotechnical testing. Instead of using the standard materials in geotechnical laboratories, like the mineral sands and soils from particular geological sources, the 3D printing technology allows us to fabricate uniform and consistent geomaterial specimens with controlled standardized properties. Hanaor et al. (2016) described the use of 3D printing to generate surrogate granular particles of irregular shape with the objective to create standard granular soils. Three different approaches are demonstrated for the 3D generation of model grains. The first method involves the superimposition of a fractal surface with higher level stochastic features on the face of a closed volume (FSO method), such as a geodesic spheroid. It should be noted that while generation of particles with fractal surface overlays allows a wide range of shapes to be generated, acquiring appropriate input parameters from natural geomaterials through morphological analyses is difficult owing to the complexity of meaningful multi-scale surface analysis.

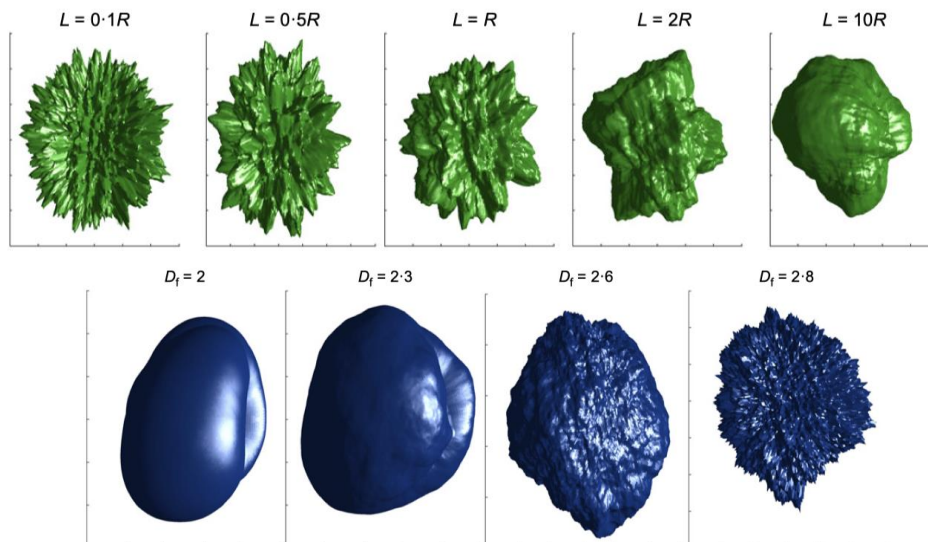


Figure 4-20 Grains simulated using the FSO method (Hanaor et al. 2016)

The second method involves the use of Fourier descriptors or fractal geometry generated from two-dimensional (2D) cross-sections and their interpolation (CRI method) to produce simulated geomaterial particles in three dimensions. Although the grains generated by this method can exhibit irregularity typical of natural particles, the interpolation method currently employed yields some unrealistic parallel ridges.

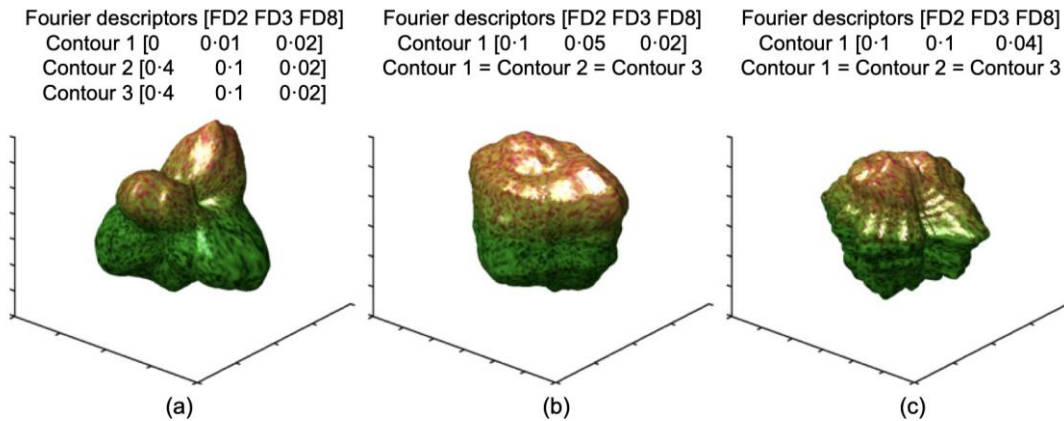


Figure 4-21 Grains simulated using the CRI method (Hanaor et al. 2016)

The third method involves the generation of complex particles by the aggregation of polyhedral elements such as cubes or octahedra which is suitable for the simulation and fabrication of porous or branching particles. In contrast to methods, such as FSO and CRI, that generate particles by varying the surface structure of initial primitive geodesic spheroids or Voronoi type cells, the DPA method employs an aggregation algorithm to construct particles of varied porosity and volume fractality from many convex polyhedral primary particles.

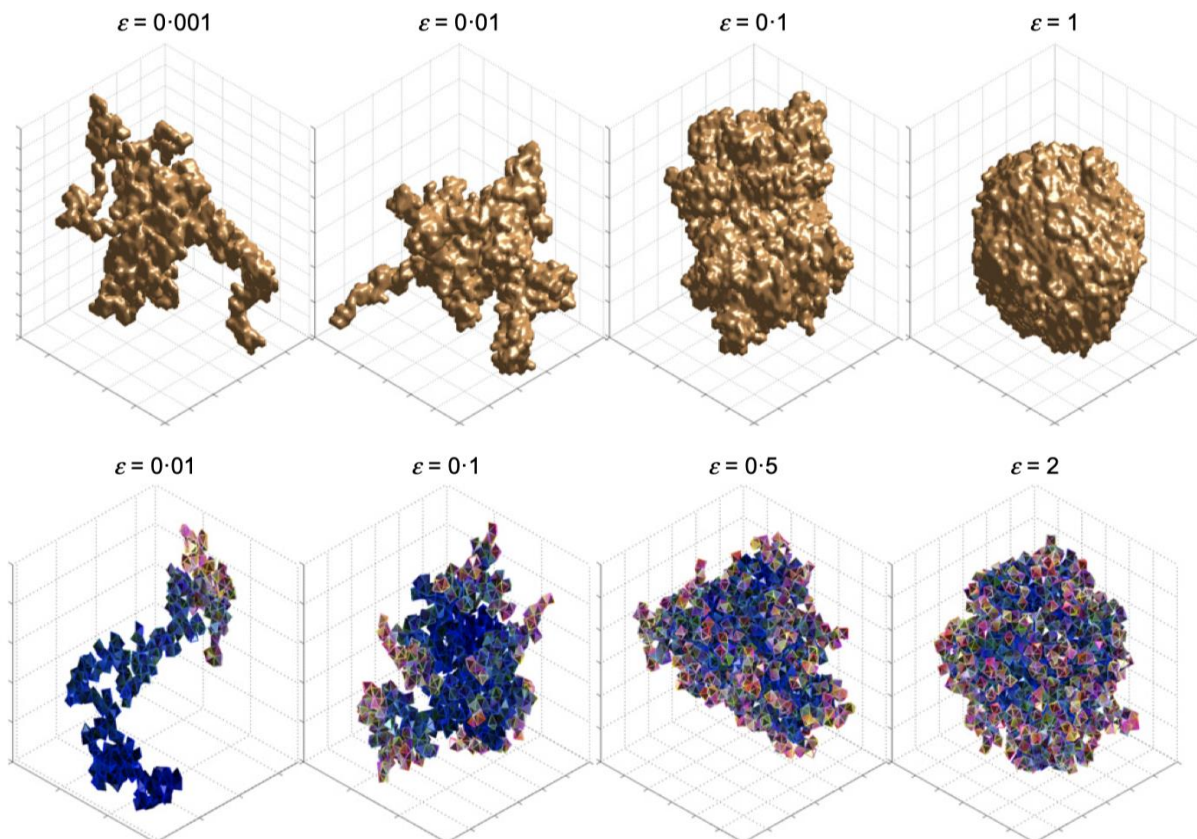


Figure 4-22 Grains simulated using the DPA method (Hanaor et al. 2016).

The morphologies obtained by the three methods can be fabricated using 3D printing methods and are further utilizable in DEM models. In the study of Hanaor et al. (2016), the 3D printer output from the polyjet fabrication of particles using these three methods were performed, as shown in Figure 4-23, Figure 4-24 and Figure 4-25. It can

be seen that with the three different methods, grains with complex morphologies can be defined and printed. The benefits and drawbacks of each method are summarized and presented in

Table 4-1.

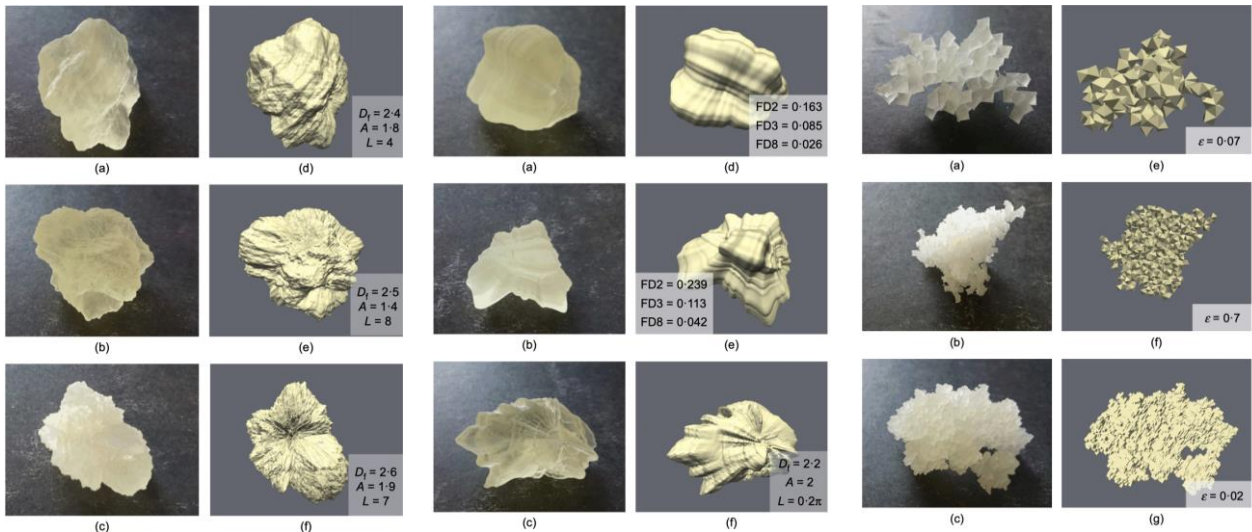


Figure 4-23 Grains from FSO method

Figure 4-24 Grains from CRI method

Figure 4-25 Grains from DPA method

Table 4-1 Summary of grain generation methodologies investigated in Hanaor et al. (2016)

FSO	Superimposition of a simulated fractal surface on a 3D geodesic spheroid	
	Benefits	<ul style="list-style-type: none"> • Reproduction of natural isotropic multi-scale grain surfaces • Grain elongation control by varying highest level wavelength
CRI	Interpolation and morphing of three 2D contours to generate a 3D surface	
	Benefits	<ul style="list-style-type: none"> • Input parameters can be readily extracted from 2D grain data • Captures properties of elongation, roughness and irregularities
DPA	Controlled assembly of polyhedral elements to yield branching aggregates	
	Benefits	<ul style="list-style-type: none"> • Reproduction of sediment particles and branching aggregates • Control of aggregate fractality by particle selection exponent
	Drawbacks	<ul style="list-style-type: none"> • Extraction of input parameters from real materials is challenging <ul style="list-style-type: none"> • Absence of smooth facets, angularity and pores • Branching morphologies cannot be simulated <ul style="list-style-type: none"> • Computationally intensive • Appropriate for studying the effect of varying morphology <ul style="list-style-type: none"> • Absence of smooth facets, angularity and pores • Anisotropic features in the form of parallel ridges <ul style="list-style-type: none"> • Branching morphologies are not represented • Input parameters can be extracted from particle characterisation <ul style="list-style-type: none"> • Surface roughness is not meaningfully represented <ul style="list-style-type: none"> • Cannot simulate solid monolithic particles <ul style="list-style-type: none"> • Computationally intensive

Triaxial tests was also performed on particles produced by the CRI method, which most readily allows input parameters to be obtained from natural geomaterials. As shown in Figure 4-26, the stress ratio (q/p') of the denser specimen rises to a peak, before reducing, with associated dilation, towards an ultimate state, while the stress ratio of the looser specimen rises gradually and the specimen compresses throughout. The second test was a repeat test using the same particles to confirm the high resistance and also to investigate whether changes in shape of the soft particles could be influencing the shear behaviour. Although a few particles were noticeably changed, it can be seen that the bulk response is not significantly affected. These results from triaxial tests using the printed grains show the ability of the printed particles to reproduce soil behaviour, and demonstrate the effect of particle shape on the material response.

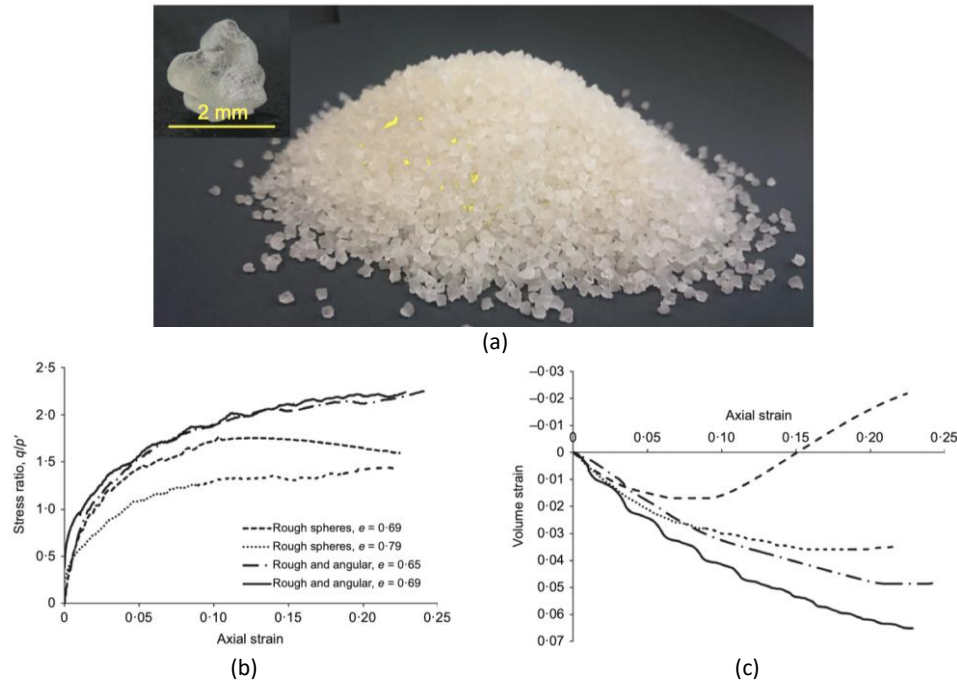


Figure 4-26 Triaxial shear behaviour of printed grains: (a) printed grains; (b) stress ratio, axial strain; (c) volume strain, axial strain (Hanaor et al. 2016).

4.3.2. Study on the hydraulic behaviour of granular materials

As the pore complexity and micro-heterogeneity are pivotal in characterizing biogeochemical processes in soils, Dal Ferro and Morari (2015) combined the X-ray computed microtomography (microCT) with 3D printing technology to evaluate the reproducibility of 3D-printing soil structures at the original scale and compared the hydraulic properties of original soil samples with those obtained from the soil-like prototypes. The printer (ProJet 3510 HD, 3D Systems, <http://www.3dsystems.com/>) was selected as it provided a fast prototype reconstruction with high resolution and available at a relatively low price. The 3D structure was printed with resin. The whole working flow is outlined in **Error! Reference source not found.** To check the reliability of 3D printing technique for capturing the pore structures inside the soil, the saturated hydraulic conductivity K was measured with both constant and variable head method for both original soil and the printed prototypes.

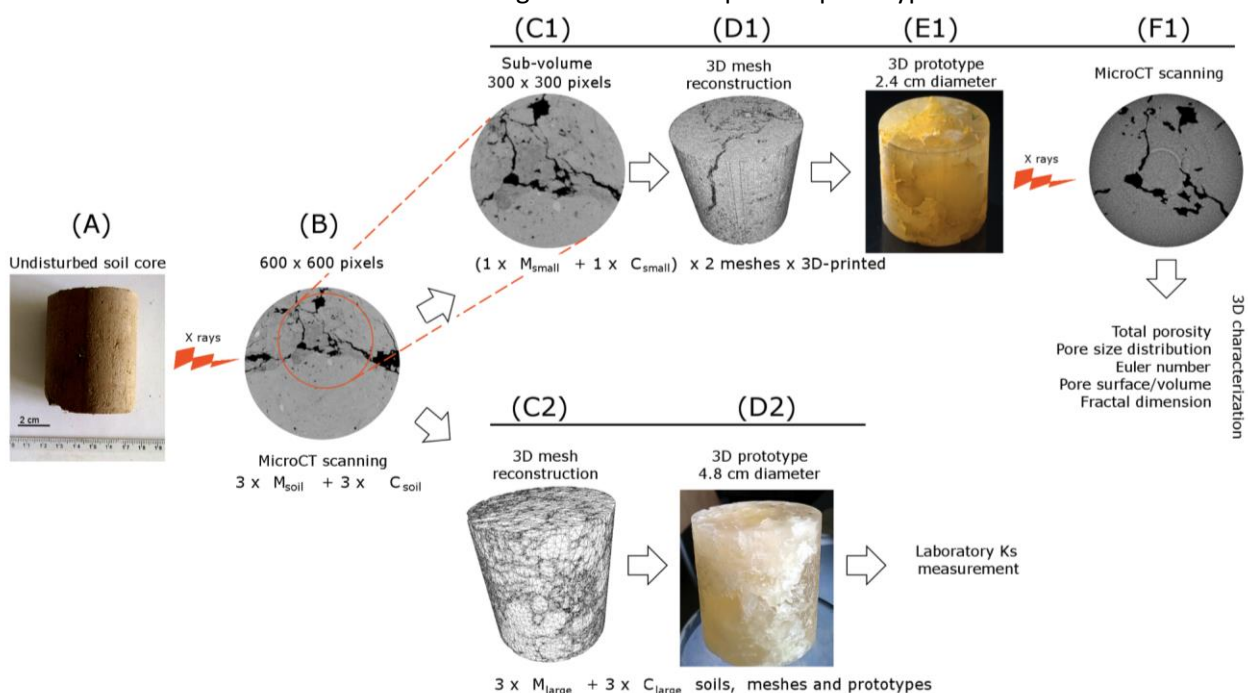


Figure 4-27 Outline of steps used to obtain soil-like prototypes and sample measurements (Dal Ferro and Morari 2015)

A result of X-ray computed microtomography (microCT) analysis of the spatial soil-like porosity and pictures of its

3D-printed copy is presented in Figure 4-28. It can be seen that the porosity of original soil can be re-constructed by the 3D printer. However, when comparing the measured hydraulic conductivity values, a significant difference can be observed in Figure 4-28(b). This is believed to be caused by the macropore surface smoothing and the hydrophobic nature of wax which ideally should be removed completely after 3D printing. Despite the deficiency, the microCT and 3D printing technology provide a completely new way to study the soil structure and its interaction with biogeochemical processes. In fact, a higher microCT scanning and 3D-printed resolution will favor the representation of the soil pore system at the nanoscale and its heterogeneity. Moreover, the use of soil-like materials will be able to model the physical-chemical interaction between water and the pore surface.

As the cohesion and capillary forces between grains are also governed by surface structures (Frayssé et al., 1999), the 3D printing could be used to elucidate how microscale characteristics affect macroscale behavior. This is possible because the 3D printed media share the same coefficient of uniformity, the same packing, and practically the same morphological characteristics while having different grain sizes; a feat impossible to achieve with natural granular media. Adamidis et al. (2019) presented such an application where the hydraulic conductivity of the three available 3D printed media (as shown in Figure 4-29(b)) is measured and then compared with commonly used formulas.

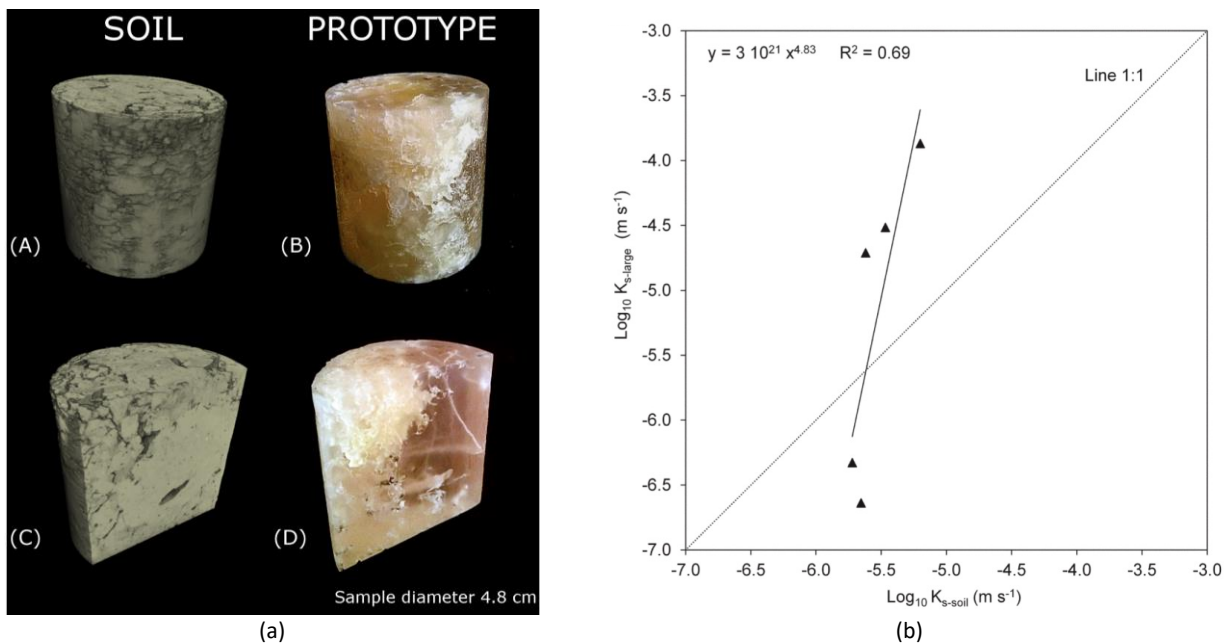


Figure 4-28 Soil samples and hydraulic test results: (a) Three-dimensional representations of original and printed soil samples; (b) comparison of hydraulic conductivity of original and printed samples (Dal Ferro and Morari 2015).

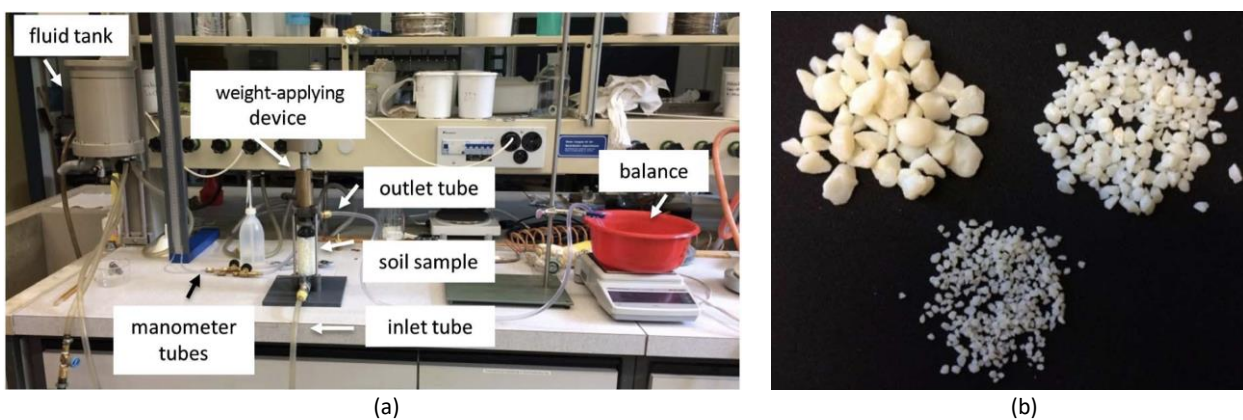


Figure 4-29 Laboratory setup and printed particles for hydraulic conductivity measurements: (a) experimental setup; (b) printed particles (Adamidis et al. 2019)

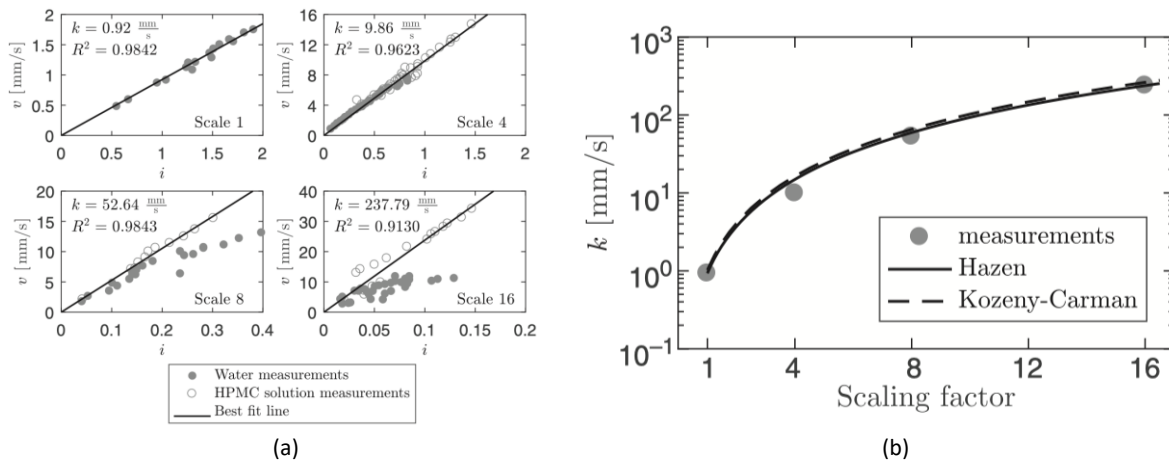


Figure 4-30 Hydraulic conductivity measurements and its variation with scale factor: (a) hydraulic conductivity measurements; (b) comparison to the predictions of the formulas of Hazen and Kozeny-Carman (Adamidis et al. 2019).

As shown in Figure 4-30, a linear relation between the hydraulic gradient and the flow velocity was realized for Hostun sand (Scale 1 in Figure 4-30(a)) and for scaling factor 4 using water, as one would expect considering critical velocities. For the other two media, a linear relation was captured using the viscous HPMC solution. It is also worth pointing out how well Kozeny-Carman's formula performed in predicting hydraulic conductivity. The results of Figure 4-30(b) confirm the square law linking hydraulic conductivity to particle size.

Wei et al. (2021) also explored water permeability of uniformly graded irregular grains using 3D printing with controlled shapes and fractal morphological features at low Reynold's number for viscous flow. In this study, the 3D Fourier Transformation was used to transform spherical surfaces into a sum of Spherical Harmonic (SH) function. A poly-jet layer-printing 3D printer (Objet Eden 250) with horizontal and vertical resolutions of 4 and 32 μm was used. The shape parameter inputs for the printed grains, the printed grains and the experimental setup are presented in Figure 4-31.

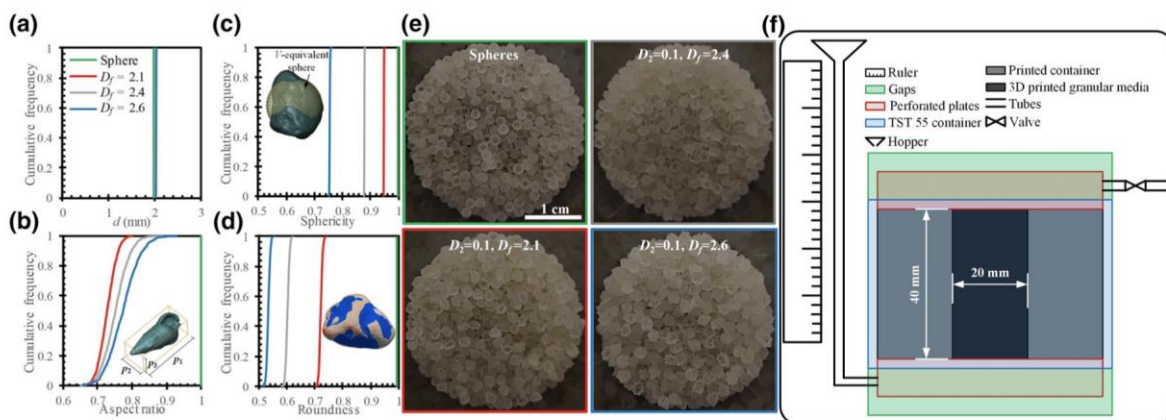


Figure 4-31 The printed grains and the test setup: (a)-(d) Cumulative distributions of classical shape indices of printed grains; (e) Snapshots of printed grains; (f) Schematic of the modified TST-55 permeameter for experiments (Wei et al. 2021).

Figure 4-32(a) shows the measured absolute coefficients of water permeability as a function of porosity for different particle shapes. With the increase of D_f (SH fractal dimension, representing the particle shape), the tortuosity of pores in porous media of same porosity becomes higher, resulting in lower permeability. Based on the experimental results, a modified Kozeny-Carman equation was proposed through more accurate determination of specific area, as a function of relative roughness and fractal dimension, than approximation using the volume-equivalent sphere. By isolating the contributions from specific area, the shape coefficient is found to be insensitive to particle morphology. Through benchmarking the model prediction against experiments from both this work and past literature, the validity and wide applicability of the modified Kozeny-Carman equation were checked.

Apart from the hydraulic response, the granular flow is commonly encountered across different fields including silo discharge in the food industry, cement production and the transport of mining products (Hafez et al. 2021). Migrating particles may jam and form arches that span constrictions and hinder particle flow. Most studies have

investigated the migration and clogging of spherical particles. However, natural particles are rarely spherical, but exhibit eccentricity, angularity and roughness. The 3D printing technique provides the possibility to produce particles with any arbitrary shapes. Therefore, Hafez et al. (2021) studied the discharge of spherical, elongated, faceted, and non-convex particles during both dry granular and particle-laden fluid flow. Plastic particles of four different shapes: cube, 2D cross, 3D cross and sphere were printed with acrylonitrile butadiene styrene plastic filament, as shown in Figure 4-33.

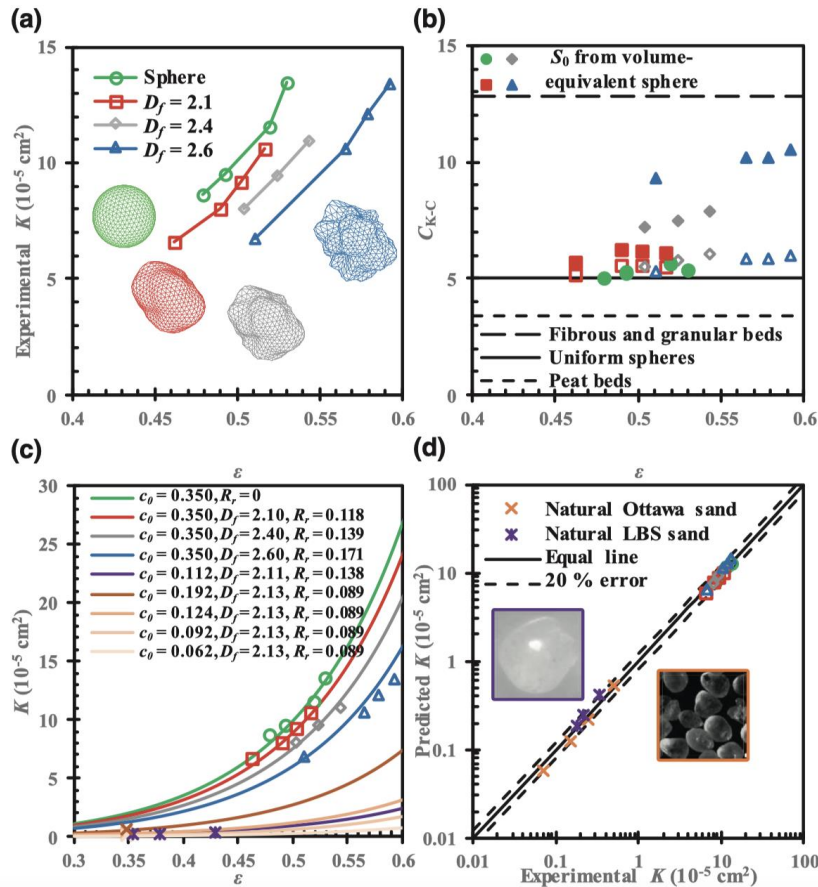
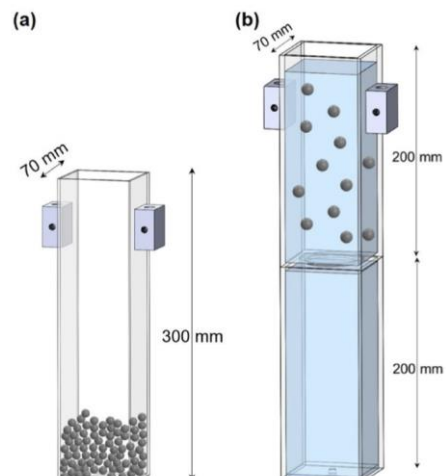


Figure 4-32 experimental water permeability coefficients as a function of porosity; (b) relations between C_{k-c} and porosity for S_0 calculated from STLs (void symbols) or volume equivalent spheres (solid symbols). Values for fibrous and granular beds, uniform spheres, and peat beds are from Li and Gu (2005), Carman (1937), and Mathvan and Viraraghavan (1992), respectively; (c) relations between porosity and water permeability coefficients with lines for the proposed equation and data points for experimental data. The color orange and purple denote natural Ottawa sand and LBS particles. The unit of c_0 is cm; (d) comparisons between experimental results and predictions of modified Kozeny-Carman equation, including two natural LBS (Taylor et al., 2017) and Ottawa sand (Schroth et al., 1996) particles.

Shape	Sketch	Dimensions d	Sphericity ψ []	Angle of repose [°] Mean \pm SD	Dry flow	
					Initial solidity Φ_i []	$(d_o/d)_{50}$ []
3D cross			0.54	38 ± 5	0.45	6.7
2D cross			0.6	33 ± 5	0.53	5.5
Cube			0.8	33 ± 4	0.83	7.2
Sphere			1.0	25 ± 2	0.68	4.7

(a)



(b)

Figure 4-33 Granular particles and the test setup: (a) the four different shape particles; (b) the dry granular flow and particle-laden fluid flow test setups (Hafez et al. 2021).

As shown in Figure 4-34, cubes and 3D crosses are the most prone to clogging because of their ability to interlock or the development of face-to-face contacts that can resist torque and enhance bridging. Spheres arriving to the orifice must be correctly positioned to create stable bridges, while flat 2D crosses orient their longest axes in the direction of flowlines across the orifice and favor flow. Intermittent clogging causes kinetic retardation in particle-laden flow even in the absence of inertial effects; the gradual increase in the local particle solidity above the constriction enhances particle interactions and the probability of clogging. The discharge volume before clogging is a Poisson process for small orifice-to-particle size ratio; however, the clogging probability becomes history-dependent for non-spherical particles at large orifice-to-particle size ratio and high solidities, i.e., when particle-particle interactions and interlocking gain significance.

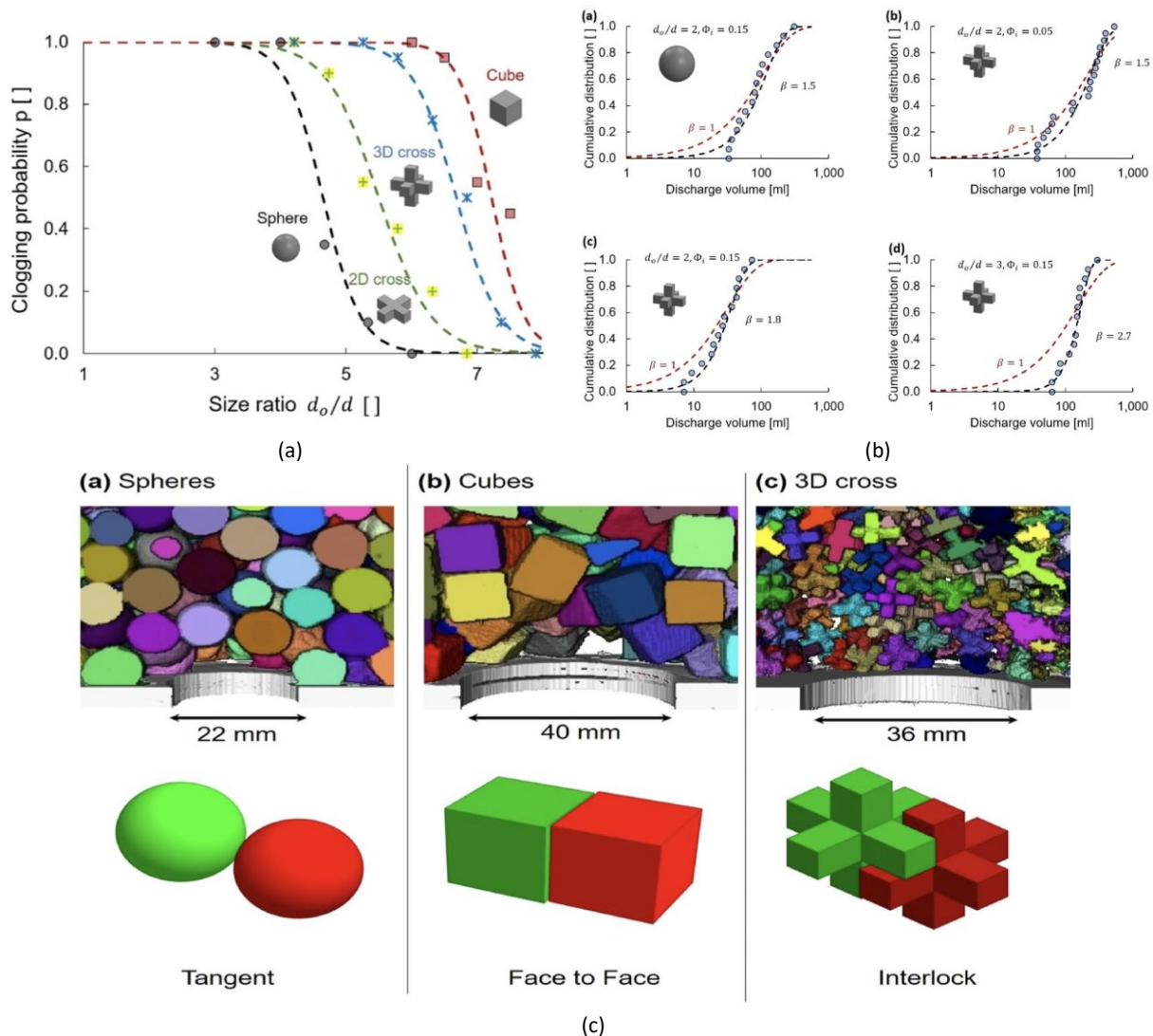


Figure 4-34 The influence of particle shape on clogging: (a) clogging probability; (b) discharge volume; (c) bridge topology from CT scan (Hafez et al. 2021).

4.3.3. Conclusion

In this section, a comprehensive review was presented on the application of 3D printing technologies in the study of granular materials' behaviour. Amazing work has been done using the powerful 3D printing technologies to replicate the complex morphology of granular particles. It is clear that this new technology can already be used for validating the reliability of the molecular dynamics (MD) or discrete element modelling (DEM), at the same time, contributing to the multi-scale investigation of the mechanical and hydraulic behaviour of granular materials.

However, there is still a fundamental issue left to solve when using the 3D printing technologies in

granular material studies: the different stiffness of the printing material and granular material (i.e. quartz) as one of the most important mechanical features of granular materials is their dependency on stress level. Bridging the behaviour of 3D printed granular materials (i.e. using much softer materials) with that of real granular materials (i.e. much stiffer) at different stress levels will be a challenge. In addition, the size and surface roughness of 3D printed particles are far from those of real granular particles. How to address this “scale effect” will be another challenge. In the end, although significant developments haven been made in 3D printing technologies, the efficiency of printing particles in large scale is still low relative to the number of particles we are facing in any problem involving granular materials.

4.4. Clay printing

Stefano MURARO, Technical University of Delft.

Execution of physical testing in geotechnics requires reproducing as accurate as possible soil field conditions in the laboratory. Thus, the natural variations and characteristics of the soil deposits must be incorporated during the model construction and monitored during testing to obtain significant results. Doing so requires developing and applying innovative and modern technologies and laboratory techniques to prepare models closer to natural conditions.

4.4.1. Innovative Sample Preparation

Soil masses are natural materials with complex physical, chemical and geological relationships that amount to sizeable natural variation and randomness at different scales. This variation leads to uncertainty in geotechnical engineering analysis and design. Traditionally, physical modelling and laboratory practices have tested and characterized the properties of soil materials through the assumption of homogeneousness. Thus, physical modelling often uses homogeneous layers of site materials and disregards the effects of natural soil variation, which can be substantial. This assumption contributes to the usual difference in the behaviour that is commonly expected between physical models and their real-scale counterparts. To increase the representativeness of the experimental results, the natural variations and characteristics of the soil deposits should be incorporated during the model construction and monitored during testing. This requires developing and applying innovative and modern technology and laboratory techniques to prepare models closer to natural conditions.

Recent research has explored different ways of preparing samples for centrifuge and laboratory testing that account for natural variation in fine grained soils. Garzon et al. (2015) used random field theory to model spatial variations of the liquid limit of clays within a soil mass and showed that it could be reproduced on a centrifuge testing sample by using coloured mixtures of kaolin and bentonite clays. A centrifuge model sample is constructed by depositing the clay mixtures via extrusion at water contents above the liquid limit in a grid-like array (Figure 4-35). Using this technique, Garzon et al. (2018) tested a shallow foundation in a centrifuge and found a reduction in bearing capacity with respect to the homogeneous case, as suggested by theory.

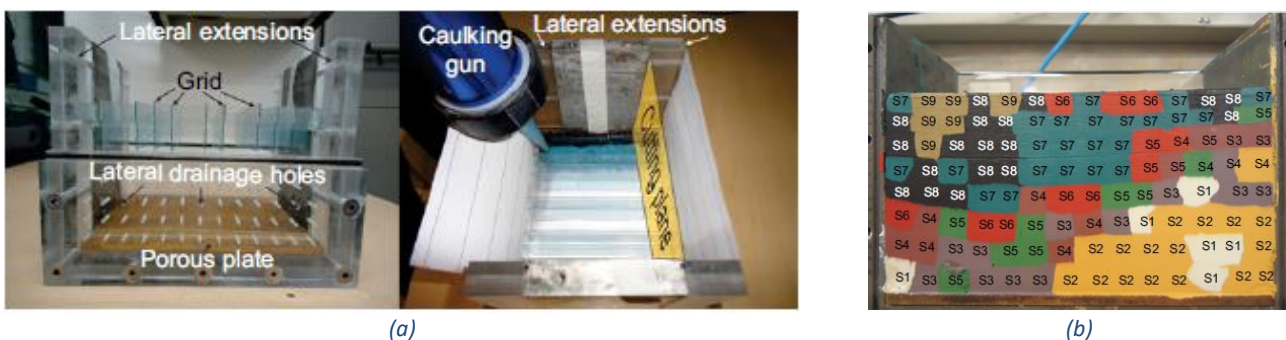


Figure 4-35. Construction of the heterogeneous model: (a) container box with the porous stone and the grid, process of placing the strings of slurries into the container and (b) Heterogeneous physical model (Garzon et al., 2015)

Pua et al. (2018) and Pua and Caicedo (2020) extended the extrusion concept and developed a 3D printer for clayey soils. As shown in Figure 4-36, a random liquid limit field was generated first for the soil sample using the random field theory whose mean is 205% and coefficient of variation is 50% with correlation lengths of 12 cm in x and y directions and 4 cm in the z direction. During the 3D printing of soil sample, the initial random field is discretised using eight types of homogeneous clays, which are mixtures of kaolin and bentonite. In addition, mineral colorants were added to differentiate the mixtures.

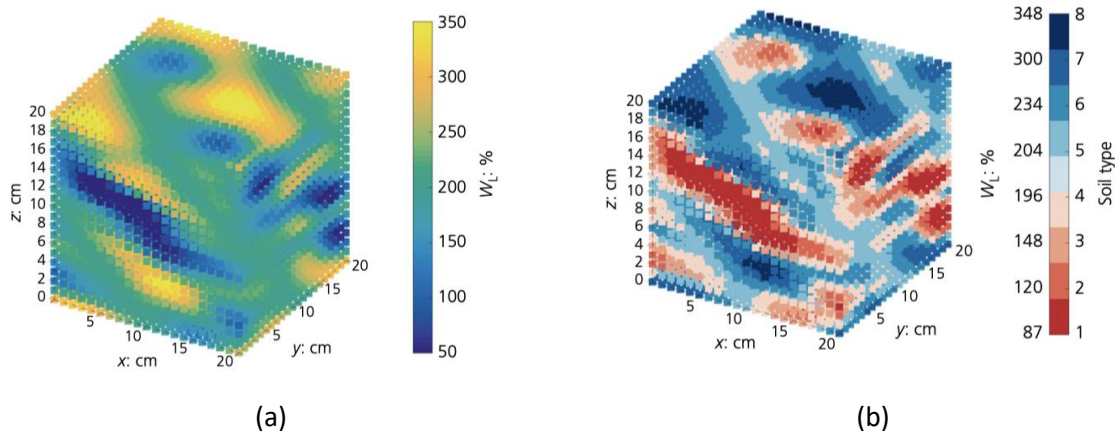


Figure 4-36 Real and discretized liquid limit field in soil sample: (a) realisation of the random field for a liquid limit whose mean is 205% and coefficient of variation is 50% with correlation lengths of 12 cm in x and y directions and 4 cm in the z direction; (b) discretisation of the liquid limit field in terms of soil type (Pua and Caicedo, 2020)

The 3D printer works by a set of 8 syringe pumps that presents eight types of homogeneous soils to reproduce the complex pattern defined previously. The key element is a commercial VICI (Valco Instruments Company Inc.) hydraulic valve, which has eight inputs and one output. This valve works as a multiplexer for the slurries coming from the extrusion syringes. The 3D clay printer has three movement axes and can build a model with maximum size of 30*30*30 cm and a controlling voxel of 5 mm (Figure 4-37).

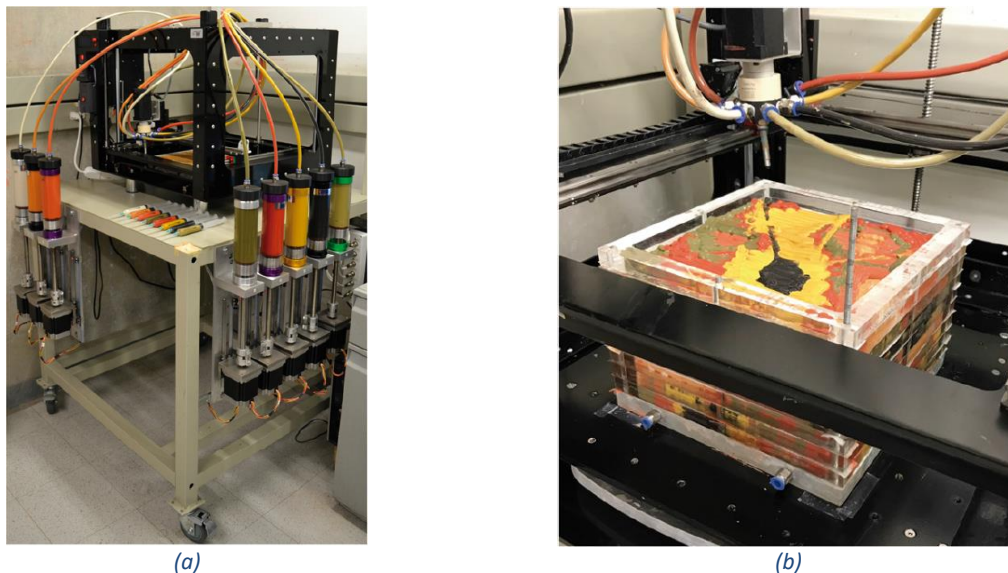


Figure 4-37. 3D printer for clay slurry: (a) photograph of the experimental set-up (b) heterogeneous model constructed with the 3D clay printer (Pua and Caicedo, 2020)

Soil water content and consistency is selected according to an indirect extrusion test, and all the equipment is sealed to prevent drying. The liquid consistency required means that the clay is not self-supported, so a modular acrylic container is used during the process. In this study, a 20*20*20 cm model sample was printed. As shown in Figure 4-38, the pattern of heterogeneous models matches well. Unwanted shallow traces generated by movement of the machine can be seen but do not detract from the basic patterns.

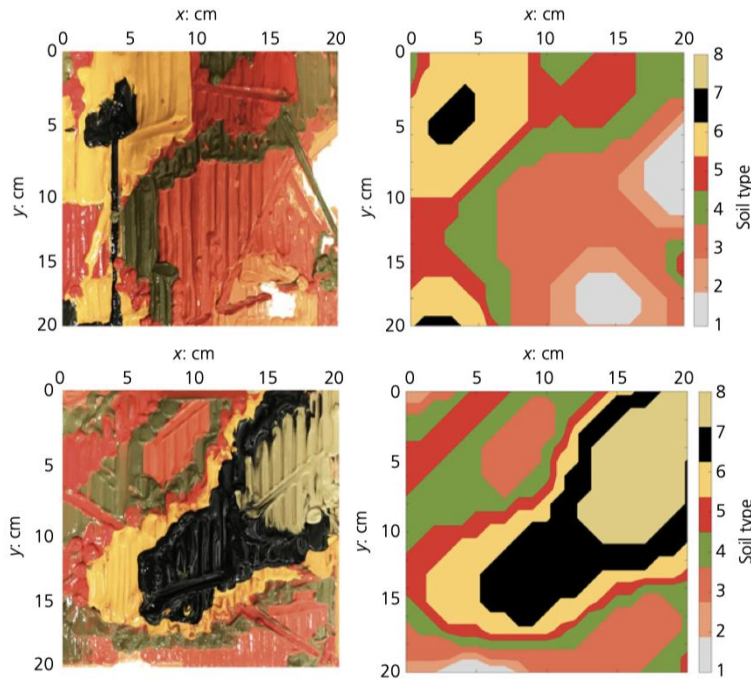


Figure 4-38 View of the printed layer for $z = 14$ cm and the corresponding layer generated numerically (Pua and Caicedo, 2020)

After construction of a heterogeneous sample, consolidation stress is applied by applying extra surcharge at sample surface. However, it should be noted that the model has heterogeneous compressibility in space. Consequently, using a rigid plate for consolidation could lead to biased results. To minimise this problem, and considering the still very liquid initial consistency of the model, only the first two consolidation steps of low stress (i.e. 3 and 6 kPa) were applied with a rigid plate but the following three consolidation stages of higher stress up to 50 kPa were applied using a flexible latex membrane filled with water (Figure 4-39).

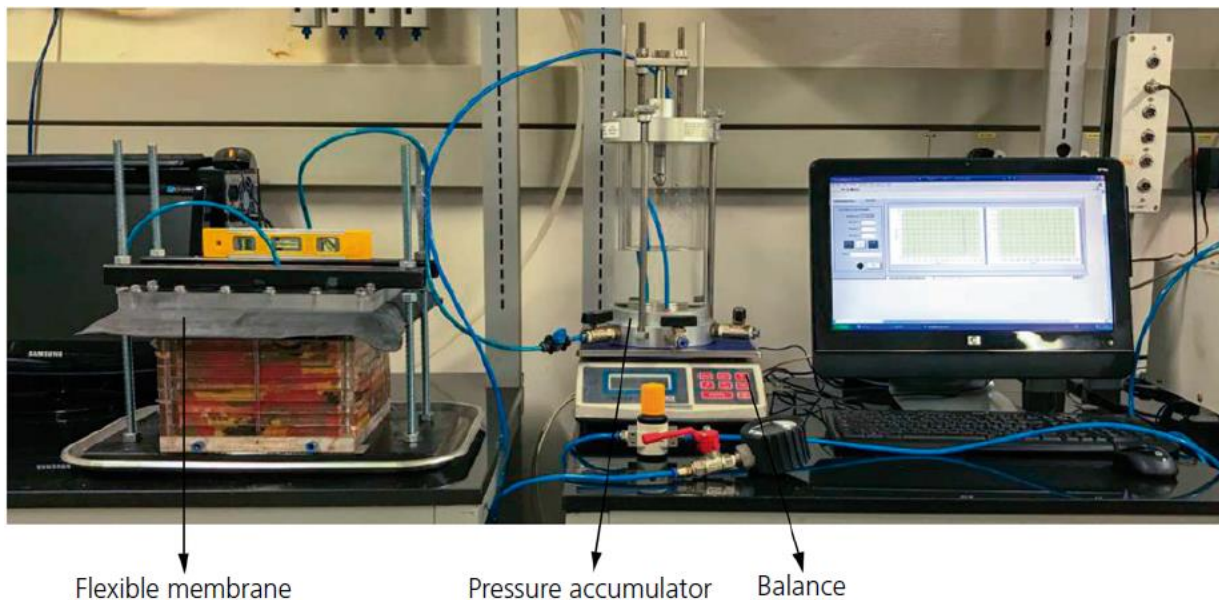


Figure 4-39. Consolidation set-up using a flexible membrane (Pua and Caicedo, 2020)

The variability of the heterogeneous model was characterised by continuously measuring 25 vertical profiles of electrical properties using a high-resolution electrical resistivity needle probe and 20 profiles of undrained shear strength using a miniature ball penetrometer, as shown in Figure 4-40.

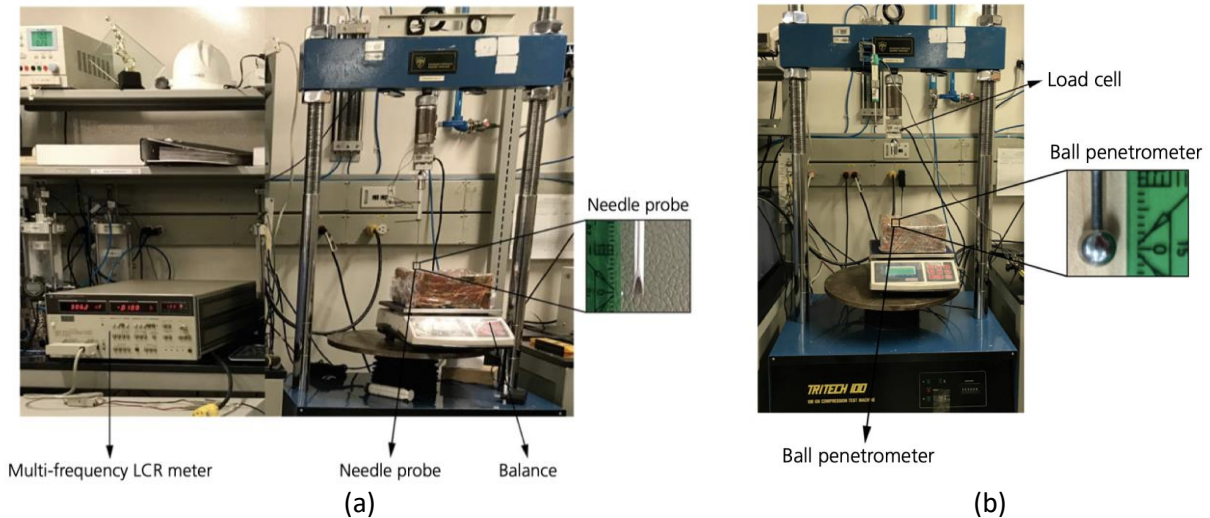


Figure 4-40 Characterisation of the variability of the physical model: (a) set-up for measuring soil impedance with detail of needle tip; (b) set-up for measuring undrained strength (Pua and Caicedo, 2020)

Figure 4-41 shows the electrical resistivity and shear strength of the soil in different 2D planes obtained from measurements of the 25 needle probe testing and 20 ball penetrating testing. It can be seen that both tests can assess spatial variability of soil properties. A clearly heterogeneous sample was successfully printed. In addition, zones with high and low resistances and strength are well defined and randomly distributed reflecting the random distribution of clays within the field.

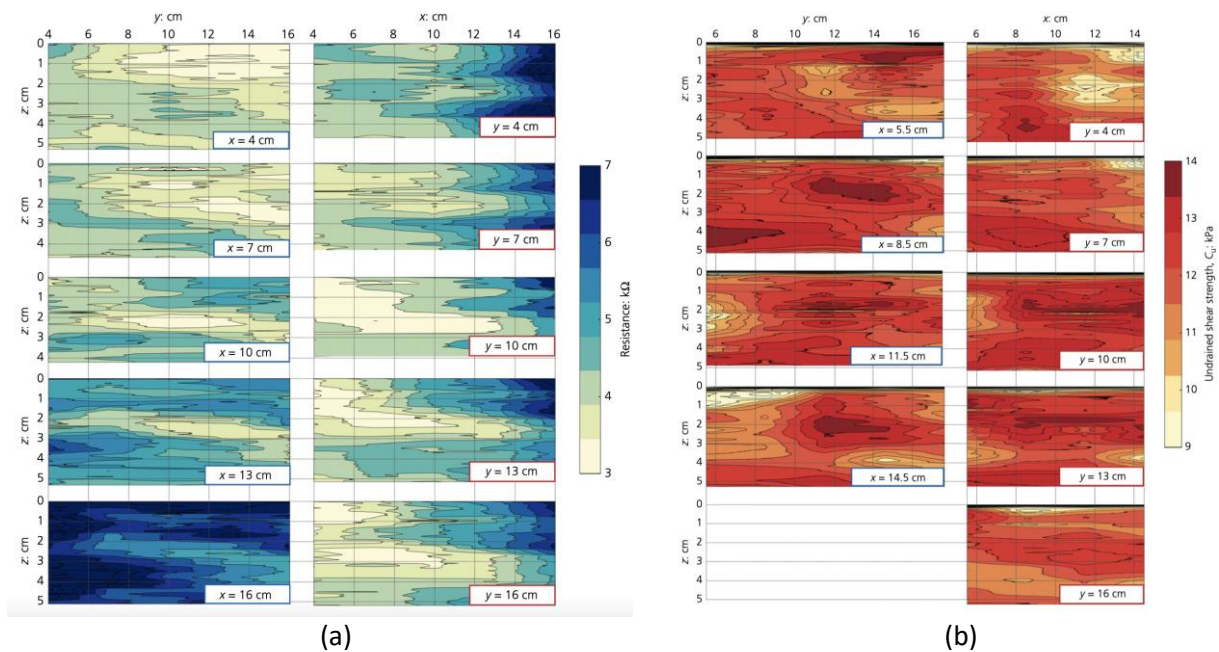


Figure 4-41 Map of: (a) electrical resistivity of the heterogeneous model; (b) undrained strength of the heterogeneous model (Pua and Caicedo, 2020)

Different from the 3D printing in Pua et al. (2018) and Pua and Caicedo (2020), Divall et al. (2018) developed a method for creating layered clay models within a geotechnical centrifuge by sedimenting high water content slurries in-flight, since many sedimented soils are deposited from eroded and transported material. According to Phillips et al. (2014), when both natural and reconstituted clay cuttings are agitated in water, they disaggregate into slurries containing a high proportion of silt sized agglomerations of clay particles or ‘clay peds’ rather than individual clay particles. It is likely that the majority of sedimented clays are formed from these silt sized clay peds and not the clay particles present in powdered clays such as Speswhite kaolin. In this study, a moderately stiff normally consolidated clay sample was prepared first following the common procedures used for clay sample preparation (Lau 2015). The clay was then divided into ‘cuttings’ (of approximately 40–50 mm³) and placed into the planetary mixer with more distilled water to a water-content of 1285%, consisting of 500 g of clay, 200 g of

sand and 9 L of distilled water. It was then mixed for about 30 minutes until fully disaggregated. The silt-sized clay agglomerate and sand-based slurry was poured into a second soil container and subjected to acceleration on the centrifuge of 160g. This forced the larger soil particles and agglomerates to sediment first with the finer material sedimenting later. This process created the layered soil structure that can be seen in standard sedimentation columns but across a soil container suitable for larger scale centrifuge model testing.

The undrained shear strength of a typical sample prepared using this method is presented in Figure 4-42(b) from the T-bar penetration test using the setup in Figure 4-42(a). The soil on the top layer was very weak and had very little “stand-up” time. This was assumed to be owing to the unloading process during deceleration of the centrifuge and the standing water above the soil as part of the sedimentation process. As shown in Figure 4-42(b), at shallow clay layer, there is a shear strength of 0.25 kPa. But, the readings from T-bar increase dramatically when passing through the sand layer below and then drop to approximately 0.65 kPa. This layer is assumed to be the second clay stratum. This has been stressed by the weight of the layer above and therefore has a slightly higher undrained shear strength compared with the uppermost layer. After this, the readings decrease for the intermediate clay layer before increasing once again for the sand layer. This shows it is possible to identify the sand and clay layers and possibly their relative strengths.

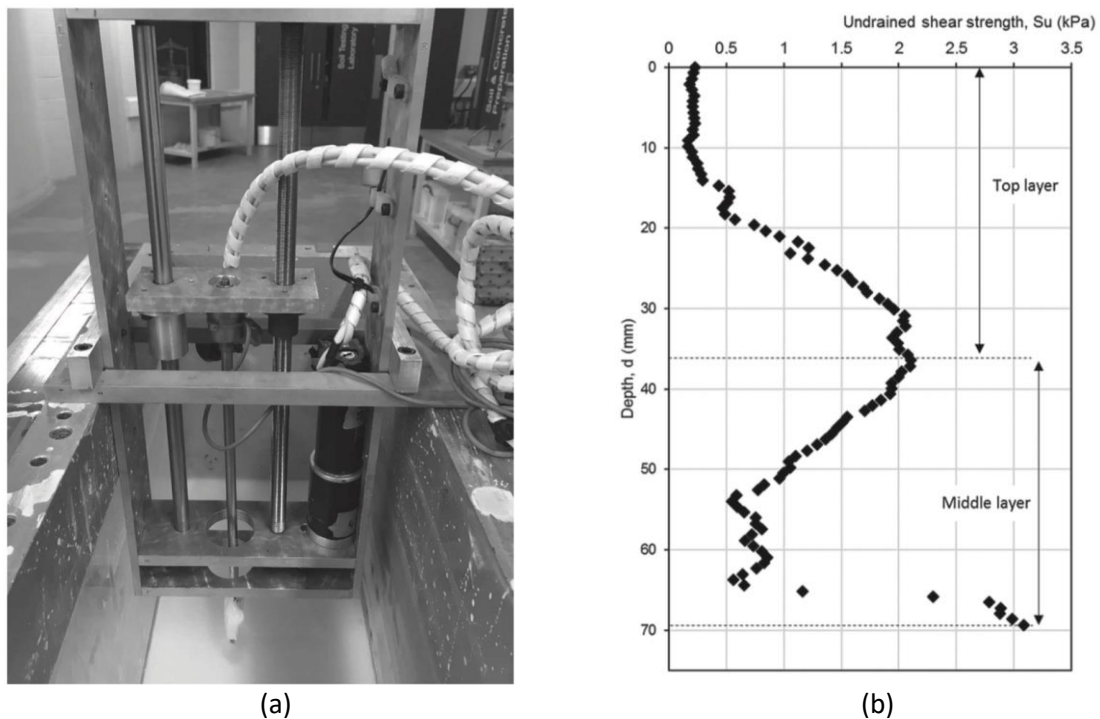


Figure 4-42 Sample characterization: (a) T-bar penetrometer and frame used for determining the undrained shear strength with depth; (b) T-bar readings with depth for the layered soil sample

4.4.2. Conclusion

This section presents two advanced sample preparation methods to replicate the natural variations of soil. The printer is an enticing proof of concept for 3D printing samples with clayey materials with controlled variability in three dimensions. This equipment allows analysis of the effects of soil variability and can be used for validating and calibrating the extensive numerical studies that are available in the literature. However, there are still some problems that should be addressed. The coloring minerals added to keep track of different printed materials can impact the properties of the clay mixtures, so their use should be controlled and studied. The printing time can be a large issue as the sample must be protected from drying to avoid the development of cracks or voids. The appearance of gaps between layers and or in the corners can be a problem; however, exposing the printed piece to a vacuum can help prevent the apparition of bubbles. The consolidation process can introduce frontier effects and change the volumetric distribution of the material as more compressible layers get compacted further and change stress distribution. Pua et al. (2018) show that the printer concept is a viable way of generating samples generated from a liquid limit random field; however, further studies are required to understand how to create model samples that reproduce other field properties and conditions.

The other sample preparation is designed to create a centrifuge model with a sedimented soil structure as defined by Mitchell (1976). A novel procedure for creating a layered soil model within a geotechnical centrifuge was proposed and proved promising based on the undrained shear strength profile from T-bar testing. However, one major shortcoming of this method is that the method currently creates very weak soil samples. This would be overcome by creating more layers and allowing drainage after the layers have been created, to remove the surface water. This would help prevent the soil swelling and reabsorbing the standing water on top of the final layer. In addition, the required sedimentation time will increase exponentially with the target sample size, making it less efficient and practical.

4.4 Rock type material printing

Luc THOREL, University Gustave Eiffel; Huan WANG, Technical University of Delft

Jaber (2020) has made a review of the use of 3D printing in Rock mechanics, which has given the core of this part. Jiang and Zhao (2015) were among the first to test the applicability of 3DP in rock mechanics. They studied the behavior of PLA (polylactic acid) specimens using the FDM technique. Several geometries are tested: continuous specimens, specimens having a lattice configuration (nodes + bars) and specimens with a microstructure and voids (Figure 4-43). The aim was to compare the behavior obtained with that of rocks and to study the effect of microstructures on the overall behavior of PLA. However, this 3DP technique and the material used are not the most suitable for simulating a rock matrix. The mechanical behavior of PLA under uniaxial compression is ductile, and it is a very deformable material, not showing crack propagation at rupture (Figure 4-43).

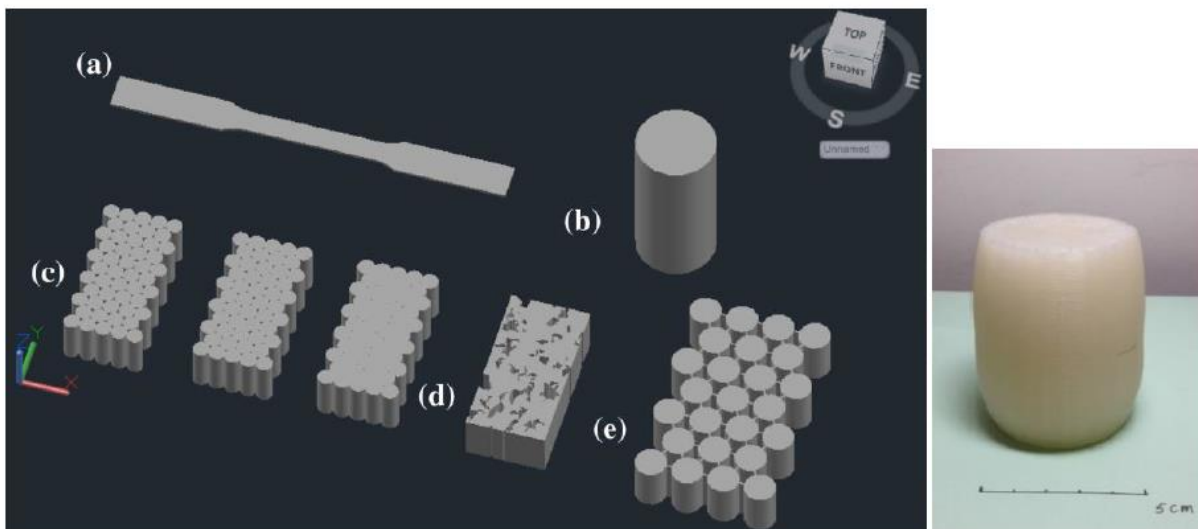


Figure 4-43 : Different geometries built by the FDM technique of 3DP and tested by Jiang and Zhao, 2015 to characterize them mechanically.

This work was followed by preliminary studies to find the “ideal” analogue rock material (Jiang et al., 2016c; Zhou and Zhu, 2018). In order to optimize the results and approach the behavior of rocks, Fereshtenejad and Song (2016) were interested in studying the effects of printing parameters on the mechanical parameters of compression specimens.

The printer used is powder-based (ZPrinter 450) and the material used is ZP 150 powder with Zb 63 as a binder. This study highlights the dependence between the mechanical properties of the parts and the printing parameters. The studies cited above are general characterization studies. Other more specific studies are carried out. They can be classified according to the type of 3DP application: study of porosity and permeability, study of crack propagation and study of stress distribution inside a heterogeneous mass.

4.4.1. Porosity and permeability

The technique mainly used in this type of study is sand-based 3DP. The main advantage of this technique is the use of geomaterials respecting similar behavior than rocks. In the manufacturing process, the sand is mixed with binders, and the cohesion between the different layers is ensured by a chemical reaction during the deposition of the layers. Osinga et al. (2015) tested continuous compression specimens and others containing a single through fracture. These tests have made it possible to highlight the interest of this technique, especially since the base material used is a geomaterial. In the same perspective, and given the influence of manufacturing parameters on mechanical properties, Primkulov et al., 2017 studied the influence of temperature on binders added to sand. Gomez et al., 2017;2019 (Figure 4-44) characterized the porosity and permeability of compression specimens constructed by sand-based 3DP. They found that this technique can reproduce a porosity similar to the porosity of rocks. However, and for application to reservoir studies, specimens fabricated by 3DP are more compressible and permeable than typical reservoir rocks. Optimizations of the manufacturing technique are therefore necessary to achieve the authors' goal.

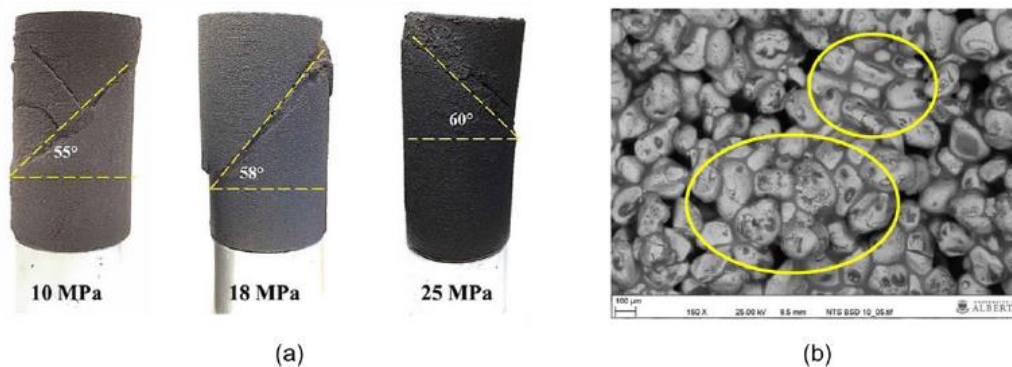


Figure 4-44 : a) Compression specimens built by 3DP based on sand; b) corresponding SEM image in order to characterize the porosity of the specimens (from Gomez et al., 2019).

Other techniques have been tested to validate the possibility of using 3DP to concretely model the porosity of rocks. Head and Vanorio (2016) used a resin in the construction of their heterogeneous model from which they calculated the permeability. Ishutov et al. (2015) printed connected porosity networks using an FDM filament printer (materials: ABS³ and PLA⁴) (Figure 4-45). However, this technique, with its basic parameters, is one of the least precise in 3DP and does not allow good resolutions to be obtained when the geometry becomes complex. Suzuki et al. (2016, 2017) generated a network of fractures in a test piece built by 3DP (VisiJet[®] EX200 Plastic Material for 3-D Modeling, 3D Systems), and injected water to study the hydraulic behavior of the test piece. They find that even if the geometry of the fracture network is globally respected, the experimental result is far from the numerical simulations and therefore questions must arise as to the ability of the material used to simulate rocks. Liu et al. (2016) found similar trends (gap between experimental and theoretical properties) using transparent (vero clear⁵) materials for the matrix and opaque (RGD white) for reservoir heterogeneities.



Figure 4-45 Networks of fractures obtained from 3D printing by the FDM technique (from Ishutov et al., 2014).

³ Acrylonitrile Butadiene Styrene, $(C_8H_8)_x(C_4H_6)_y(C_3H_3N)_z$, is a common thermoplastic polymer. Young's Modulus 2.28 GPa; Tensile Strength 43MPa.

⁴ Polylactic acid, also known as poly(lactic acid) or polylactide, $(C_3H_4O_2)_n$ or $[-C(CH_3)HC(=O)O-]_n$ is a thermoplastic polyester. . Young's Modulus 2.7-16 GPa; Tensile Strength 16MPa.

⁵ VeroClear™ simulates PMMA (polymethyl methacrylate), commonly known as acrylic, and enables the visualization of internal components

4.4.2. Crack propagation

Jiang et al. (2016a) and Sharafisafa et al. (2018) used the same material (VisiJet PXL Core hemihydrate $\text{CaSO}_4 \cdot 0.5\text{H}_2\text{O}$, a gypsum-based material) and the same 3DP technique to study the ability of this material to initiate crack propagation, from a pre-existing defect in the matrix. The common conclusion of these two works is the possibility of initiating crack propagation and reproducing brittle behavior under uniaxial compression, unlike specimens constructed from polymers. A second material, plastic, is used in the study of crack propagation: transparent resin. This material (Zhu et al., 2018; Zhou et al., 2019) is mainly used to visualize the mode of crack propagation inside the specimen constructed by 3DP (Figure 4-46).

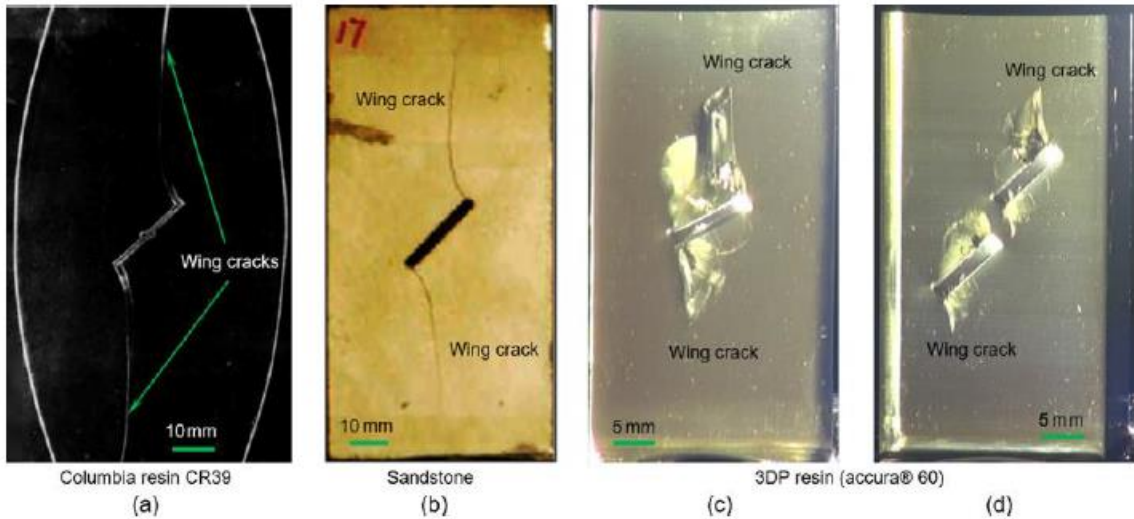


Figure 4-46 Comparison between crack propagation in a resin, in a sandstone rock, and in resin specimens built by 3DP (from Zhou et al., 2019).

4.4.3. Stress distribution

The materials used for visualization of the stress distribution in the rock mass as a function of the fracture network, are photoelastic polymers. Ju et al. (2014, 2017), Wang et al. (2017) studied the stress distribution in 3DP specimens simulating rock formations, in the presence of heterogeneities (Figure 4-47). They used the Object Connex 500 printer to make cubic test tubes in "Vero Clear" photopolymers for the matrix and opaque materials, such as "Vero Xhite plus" and "Fullcure 705" for the fractures. The choice of materials is driven by the possibility of visualizing the distribution of stresses by photoelastic techniques. However, these tests remain preliminary and lack a detailed study of the characterization of the intact material and its comparison to real rocks.

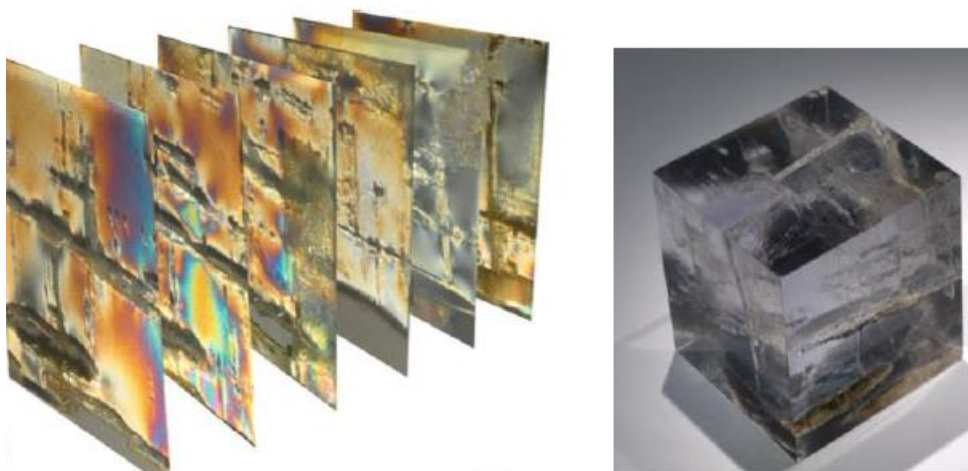


Figure 4-47 Visualization of the stress distribution in slices of test specimens in photoelastic material, constructed by 3DP. An example of a heterogeneous specimen (50 x 50 x 50 mm) is shown on the right of the figure (from Ju et al., 2014).

4.4.4. Rock joint

Jiang et al. (2016b) investigated the ability of additive manufacturing to reproduce the roughness of rock joints (Figure 4-48). For this, they generated a CAD model from a 3D scan of the rock joints. The model built by 3DP is a

mold used to build concrete or cement shear specimens. Additive manufacturing is in this case used to reproduce the geometry and not to characterize an analog material. Ishibashi et al. (2020) or Fang et al. (2020) also used 3DP to study the behavior of rock joints in 3D printing, generating surfaces from the fractal dimension to study the hydromechanical behavior of the joints. They found promising results in this area.

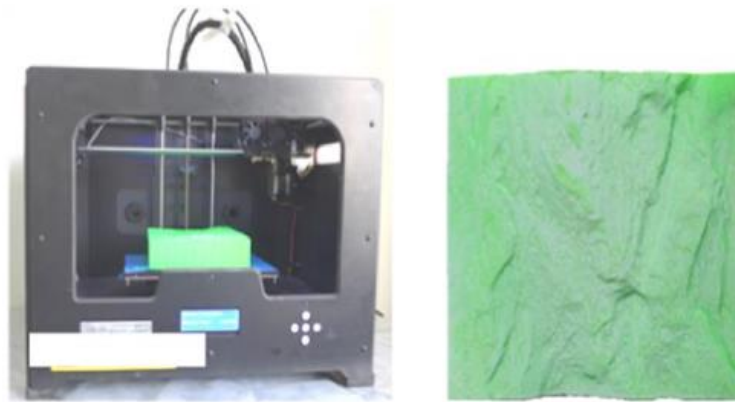


Figure 4-48 A surface of a rock joint being 3DP printed (from Jiang. et al., 2016b).

Sand-based 3-D-printing, enables to adjust the geometry and roughness of analog fault interfaces (Braun et al. 2021). Binder-jetting allows one to create composite materials by controlled mixing of two components: powder and binder. Among the various potential granular materials, silica sand is used as the powder component. Before the printing process, silica sand is mixed with an acidic activator. This activator serves later as a catalyst for the polymerization reaction of the binder. Specimens created by powder-based 3-D-printing are characterized by their micro-structure (composition of powder, binder and pore phases) and macro-structure (phase composition, macroporosity, pore geometry). Uniaxial compression tests, direct shear tests without and with designed roughness have been performed to characterize the surrogate material, also in the post-pic domain. This material has been tested on a new apparatus (Figure 4-49) designed to reproduce earthquake-like instabilities in the lab (Gutierrez-Oribio et al., 2022).

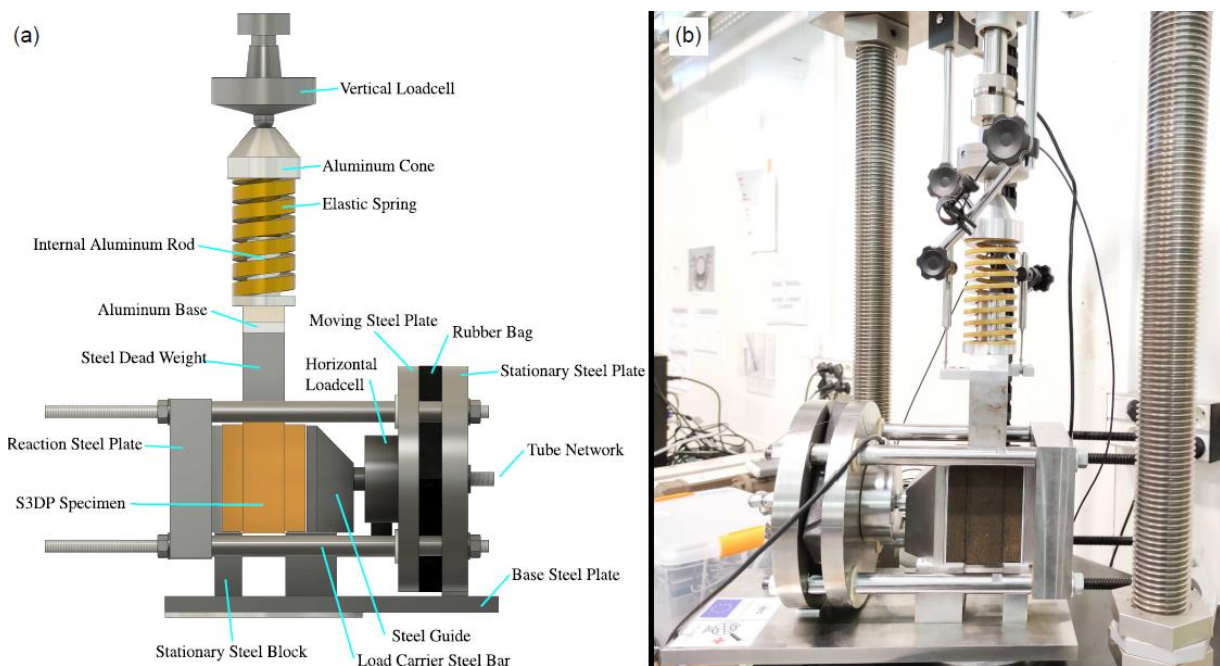


Figure 4-49 Experimental apparatus: (a) Scheme; (b) real configuration (Gutierrez-Oribio et al., 2022)

4.4.5. Small scale models

Up to now, the work performed did not target analog materials with the aim of applying them to physical modeling of geotechnical structures. Song et al. (2018) tried to build a scale model of a tunnel from additive manufacturing. Their massif is built with a gypsum-based printer, and contains a pre-excavated tunnel. A coating is printed with the FDM technique. Studies are carried out with and without coatings on a model with a total dimension of 20 cm × 20 cm (Figure 4-50). The results obtained are compared with numerical and physical models. The results are

promising, with an awareness of some limitations of additive manufacturing technologies such as respecting the laws of similarities not mentioned in the article, and the limit of the dimensions of the printed models.



Figure 4-50 Scale model built by 3DP of a tunnel. The block is printed with a gypsum-based material, and the coating is PLA (from Song et al., 2018).

Jaber et al. (2020) present the experimental results of the mechanical characterization of artificial rock joints constructed by 3D-printing (3DP). The mechanical behavior of rock masses is controlled by the presence of joints (Figure 4-51). Understanding the mechanical behavior of rock joints is essential to predict their influence on a rock mass. The application of innovative 3DP technology in rock mechanics to model artificial rock-like joints allows strict control of joint geometry (orientation, roughness, number of rock bridges, etc.), and thus of its mechanical behavior. The 3DP technology used in this work is selective laser sintering, and the material is Polyamide 12. Geometric characterization shows that this technology gives high dimensional precision for details smaller than 0.4 mm.

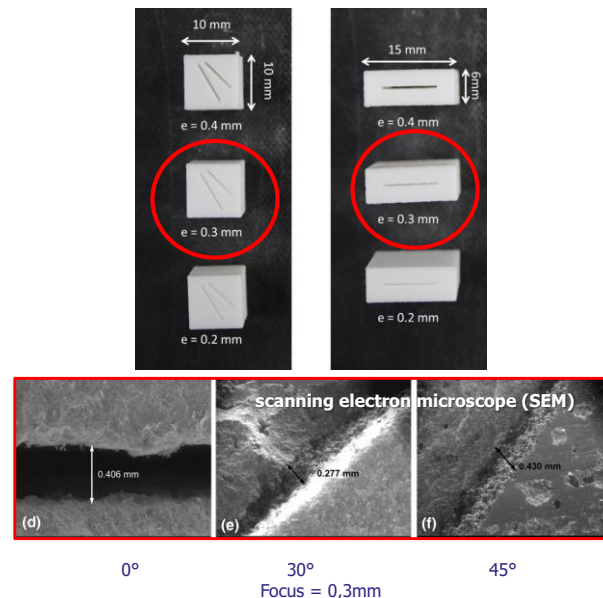


Figure 4-51. Samples of 1cm^3 used to characterize the joint aperture “e” (top) and SEM images (bottom), from Jaber et al. (2020)

More than 30 discontinuous samples were printed to investigate the global mechanical properties of a joint relative to its geometric features including Young’s Modulus (E), shear stiffness (k_s), cohesion (c_j), friction angle (φ_j) and dilation (i). The results show that the number of rock bridges (N_{rb}) and the roughness significantly influence the mechanical properties. A failure criterion that considers these parameters is proposed. These 3D-printed joints can be used in physical modeling of rock mass to understand the influence of the fractures on its stability by applying scaling laws. The application of scale factors to the experimental results shows the possibility of representing actual rocks with artificial 3DP joints.

4.4.6. Conclusions

Following this panoramic view of the applications of 3DP in rock mechanics, it is remarkable that the existing works seek to approach the real behavior of rocks at scale 1, by reproducing test specimens and laboratory tests. The work does not target analog materials with the aim of applying them to physical modeling of geotechnical structures.

Since the design of structures operated in rocky environments requires an understanding of the mechanical behavior of the rock mass, controlled both by the properties of the intact rock, as well as by the presence of rock discontinuities at any scale, two questions arise: 1) how can and should discontinuities be represented in scale models? 2) what techniques and what analog materials should be used to both reproduce a discontinuous solid

mass and respect the scale factors applied to the properties of the matrix and the joints?

4.5 Concrete printing

Luc THOREL, Université Gustave Eiffel; Huan WANG, Technical University of Delft

The introduction of digital manufacturing techniques, such as 3D printing applied to concrete material, opens up new perspectives on the way in which buildings are designed (Perrot, 2019; Zhang et al., 2019). Research on this theme is thriving and there is a high rate of innovation related to concrete. At the same time, the first life-size constructions made from printed concrete are emerging from the ground. Initially reserved for polymers, additive manufacturing is opening up to more and more materials. The transfer of this technology to construction, and therefore to concrete, initiated by Pegna (1997), benefited from the progress of computer-assisted construction design, with the implementation of the first BIM (Building Informative Modeling) digital models. Buswell et al. (2018) indicates a rise in the large-scale additive manufacturing since the concept inception in 1997.

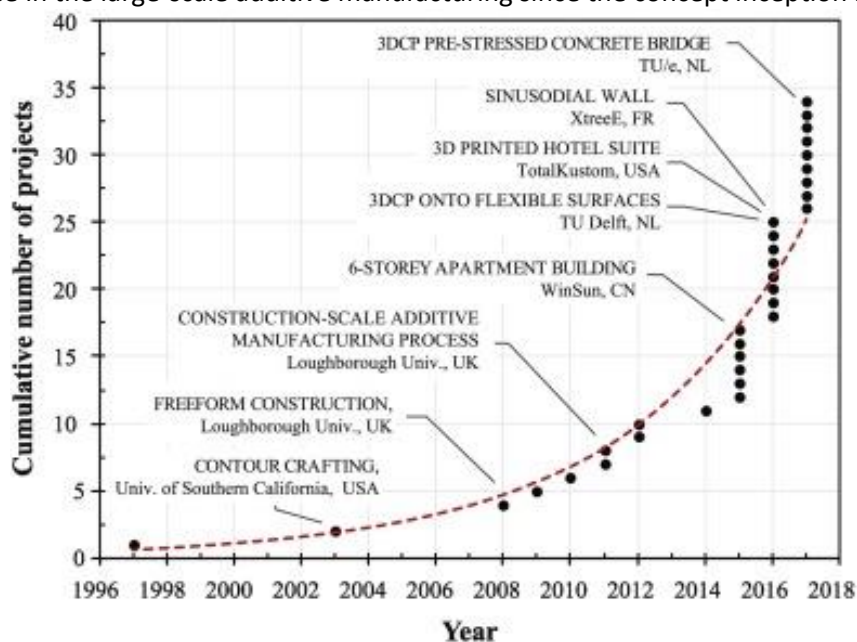


Figure 4-52 The rise in large-scale additive manufacturing for construction applications since the concept inception in 1997 (Buswell et al., 2018)

A recent example is the creation in Nantes of a 3D printed house (Figure 4-53), named Yhnova (Poullain et al., 2018). The ETH Zurich has developed a 3D printed and unreinforced concrete bridge (Figure 4-54), and plenty other applications seem possible, such as artificial reef (Figure 4-54). Other applications are in the pipeline, such as the prevention of electromagnetic interference (Wanasinghe, 2022), or concrete beam reinforcement (Gebhard et al., 2021).

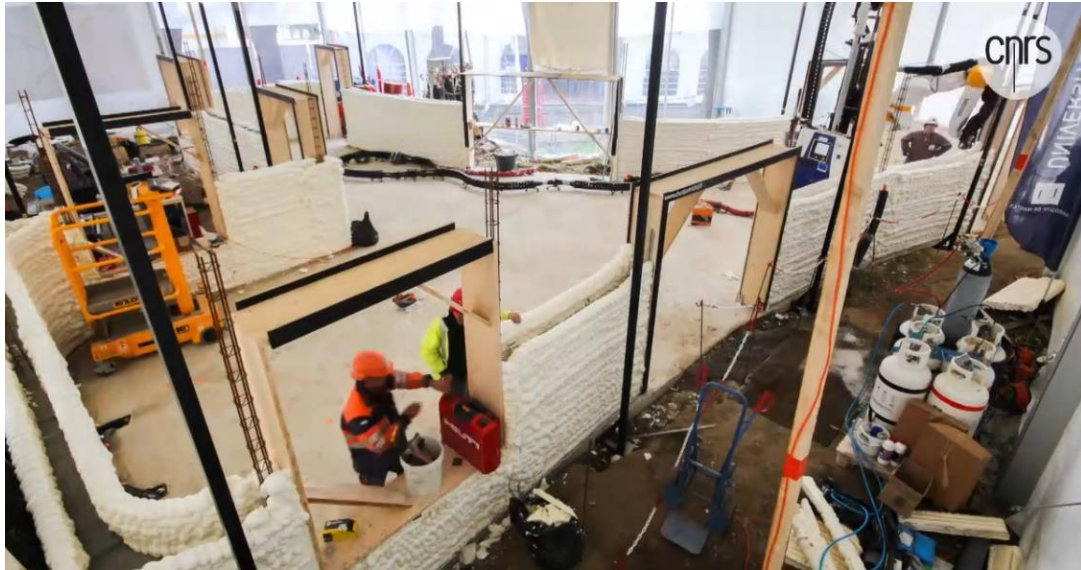


Figure 4-53 Yhnova, the 3D printed house under construction in Nantes (CNRS, 2022)



Figure 4-54 Printed and unreinforced concrete bridge on left (ETH Zurich, 2021). Artificial reef on right (XtreeE, 2017).

5 Conclusion

This report has presented an overview on new materials, new sensing and new manufacturing methods available in the European facilities of GEOLAB, but also outside its perimeter.

It shows that the limitations on the use of new approaches reduce gradually with time, and that the instrumentation based on low cost products and new technologies open the field of possibilities.

The developments on materials are still going on, when the technologies (in mechanics, electronics and software) offer a series of more and more miniature sensors.

Additive manufacturing or 3DP includes different techniques which offer a quite large range of mechanical or hydraulic properties, with a clear set of new researches in (geo)mechanics.

This report could be considered as a photography of the developed topics, but it is clear that other hot topics concern novelties in materials, sensing and manufacturing in the laboratories, but also in the industrial practice.

6 Acknowledgements

This deliverable would not have been finalized without the energy developed among the Geolab partners, by answering to an internal inquiry or by reviewing partly or totally the document. Information has also been provided by researchers and technicians involved in one of the topics presented her, namely: Prof. Olivier Deck (Mines de Nancy), Prof. Andrei Constantinescu (Ecole Polytechnique), Prof. Ioannis Stefanou (Centrale Nantes), Dr. Maria Santana Ruiz de Arbulo (Cedex), Dr. Riccardo Artoni and Philippe Audrain (University Gustave Eiffel). They are greatly acknowledged.

7 References

- 3D experience. <https://make.3dexperience.3ds.com/processes/3D-printing> (accessed on 19/01/2022).
- 3D Systems, 2022 <https://www.3dsystems.com/advantages-of-plastic-3D-printing> (accessed on 19/01/2022).
- Abdoun T, Bennett V, Danisch L, Barendse M, 2008. *Real-Time Construction Monitoring with a Wireless Shape-Acceleration Array System*. 533–540. [https://doi.org/10.1061/40972\(311\)67](https://doi.org/10.1061/40972(311)67)
- Adamidis O, Alber S, Anastasopoulos I, 2019. Assessment of Three-Dimensional Printing of Granular Media for Geotechnical Applications. *Geotech. Testing J.* 43(3): 641–659. <https://doi.org/10.1520/GTJ20180259>
- Adrian, RJ, 1991. Particle-imaging techniques for experimental fluid mechanics. *Annual Review Fluid Mechanics*, 23(1), 261–304. <https://doi.org/10.1146/annurev.fl.23.010191.001401>
- Ahmed SS, Martinez A, 2020. Modeling the mechanical behavior of coarse-grained soil using additive manufactured particle analogs. *Acta Geotechnica*, 15(10), 2829–2847. <https://doi.org/10.1007/s11440-020-01007-6>
- Ahmed SS, Martinez A, 2021. Triaxial compression behavior of 3D printed and natural sands. *Granular Matter*, 23(4), 1–21. <https://doi.org/10.1007/s10035-021-01143-0>
- Altuhafi F, O’sullivan C, Cavarretta I, 2013. Analysis of an image-based method to quantify the size and shape of sand particles. *Journal of Geotechnical and Geoenvironmental Engineering*, 139(8), 1290–1307. [https://doi.org/10.1061/\(ASCE\)GT.1943-5606.0000855](https://doi.org/10.1061/(ASCE)GT.1943-5606.0000855)
- Altuhafi FN, Coop MR, Georgiannou VN, 2016. Effect of particle shape on the mechanical behavior of natural sands. *Journal of Geotechnical and Geoenvironmental Engineering*, 142(12), 04016071. [https://doi.org/10.1061/\(ASCE\)GT.1943-5606.0001569](https://doi.org/10.1061/(ASCE)GT.1943-5606.0001569)
- Arlita, 2017. *Guía técnica*. 2ª Edición. https://www.arlita.es/sites/arlita.es/files/pdf/Guia_tecnica_ARLITA_web.pdf
- Askarinejad A, Quinten TO, Grima MA, van ’t Hof C, Gavin K, 2020. Use of optical fibres to measure pore water pressure development during impact pile driving: a geotechnical centrifuge study. *European conference of Physical Modelling in geotechnics*, 243 - 246.
- Athanassiadis AG, Miskin MZ, Kaplan P, Rodenberg N, Lee SH, Merritt J, ... Jaeger HM, 2014. Particle shape effects on the stress response of granular packings. *Soft Matter*, 10(1), 48–59. DOI <https://doi.org/10.1039/C3SM52047A>
- Berman B, 2012. 3-D printing: The new industrial revolution. *Business Horizons* 55:155–162. <https://doi.org/10.1016/j.bushor.2011.11.003>
- Braun P, Tzortzopoulos G, Stefanou I, 2021. Design of sandbased, 3-D-printed analog faults with controlled frictional properties. *Journal of Geophysical Research: Solid Earth*, 126, e2020JB020520. <https://doi.org/10.1029/2020JB020520>
- Buswell RA, Leal de Silva WR, Jones SZ, Dirrinberger J, 2018. 3D printing using concrete extrusion: a roadmap for research. *Cement concrete research* 112, 37–49. <https://doi.org/10.1016/j.cemconres.2018.05.006>
- Cabrera M, 2016. *Experimental modelling of granular flows in rotating frames* (Doctoral dissertation, Ph. D. thesis, University of Natural Resources and Life Sciences, Vienna).
- Caldeira L, Neves EMD, Saraiva P, 2012. *Reporte, LNEC – Proc. 501/19/18038, Laboratorio Nacional de Engenharia Civil (LNEC); Instituto Superior Tecnico (IST), Lisboa, Portugal.*
- Capacity for Rail, 2017. Deliverable 12.1. Innovative designs and methods for VHST (intermediate). http://www.capacity4rail.eu/IMG/pdf/c4r-d1.2.1_innovative_designs_and_methods_for_vhst_intermediate.pdf
- Carman PC, 1937. Fluid flow through a granular bed. *Transactions of the Institution of Chemical Engineers*, 15, 150–167.
- CEN/TS 17438, 2020. *Source materials considered in the development of the Aggregate standards of TC 154.*
- Cho GC, Dodds J, Santamarina JC, 2007. Closure to “Particle Shape Effects on Packing Density, Stiffness, and Strength: Natural and Crushed Sands” by Gye-Chun Cho, Jake Dodds, and J. Carlos Santamarina. *Journal of geotechnical and geoenvironmental engineering*, 133(11), 1474–1474. [https://doi.org/10.1061/\(ASCE\)1090-0241\(2006\)132:5\(591\)](https://doi.org/10.1061/(ASCE)1090-0241(2006)132:5(591))
- Chua CK, Teong WY, Low HY, Tan T, Tan HW, 2021. 3D printing and additive manufacturing of electronics. *Principles and applications*. World scientific series in 3D printing. ISBN 978-981-121-893-4, 363p.
- CNRS, 2022. *The 3D printed house (in French)* <https://lejournel.cnrs.fr/videos/a-nantes-une-maison-construite-par-impression-3d> (accessed on 26th January 2022)
- Cui Y (2019) Effect of joint type on the shear behavior of synthetic rock. *Bull Eng Geol Environ* 78:3395–3412. <https://doi.org/10.1007/s10064-018-1325-3>
- Dal Ferro N, Morari F, 2015. From Real Soils to 3D-Printed Soils: Reproduction of Complex Pore Network at the Real Size in a Silty-Loam Soil. *Soil Sci Soc Am J* 79, no. 4: 1008–1017. <https://doi.org/10.2136/sssaj2015.03.0097>
- Divall S, Stallebrass SE, Goodey RJ, Ritchie EP, 2018. Development of layered models for geotechnical centrifuge tests. In: McNamara et al. (eds), *Physical Modelling in Geotechnics*, London: CRC Press. <https://openaccess.city.ac.uk/id/eprint/19902/>
- ETH Zurich, 2021. *First 3D printed and unreinforced concrete bridge*. <https://ethz.ch/en/news-and-events/eth-news/news/2021/07/3d-printed-and-unreinforced.html> (accessed on 26th January 2022)
- EXCA, 2015. Expanded clay LWA in CEA, Lightweight fill and thermal insulation products for civil engineering applications Installation and structural quality control on site.

- <https://www.leca.no/sites/leca.no/files/pdf/Lightweight%20fill%20and%20thermal%20insulation%20products%20for%20civil%20engineering%20applicatations%20EXCA.pdf>
- Fang Y, Elsworth D, Ishibashi T, Zhang F, 2018. Permeability evolution and frictional stability of fabricated fractures with specified roughness. *Journal of Geophysical Research: Solid Earth*, 123, 9355–9375. <https://doi.org/10.1029/2018JB016215>
- Feng P, Meng X, Chen J-F, Ye L, 2015. Mechanical properties of structures 3D printed with cementitious powders. *Construction and Building Materials* 93:486–497. <https://doi.org/10.1016/j.conbuildmat.2015.05.132>
- Fereshtenejad S, Song JJ, 2016. Fundamental Study on Applicability of Powder-Based 3D Printer for Physical Modeling in Rock Mechanics. *Rock Mechanics and Rock Engineering* 49:2065–2074. <https://doi.org/10.1007/s00603-015-0904-x>
- Frayssé N, Thomé H, Petit L, 1999. Humidity effects on the stability of a sandpile. *Eur. Phys. J. B – Condensed Matter and Complex Systems* 11, No. 4, 615–619. <https://doi.org/10.1007/s100510051189>
- Futura Sciences, 2022. <https://www.futura-sciences.com/tech/definitions/imprimante-3d-impression-3d-15137/> (accessed on 17/01/2022).
- Garzón LX, Caicedo B, Sánchez-Silva M, Phoon KK, 2015. Physical modelling of soil uncertainty. *International Journal of Physical Modelling in Geotechnics*, 15(1), 19-34. <https://doi.org/10.1680/ijpmg.14.00012>
- Garzón LX, Caicedo B, Sánchez-Silva M, Phoon KK, 2018. Effect of spatial variability on the behaviour of shallow foundations: Centrifuge study. In *Physical Modelling in Geotechnics* (pp. 1285-1290). CRC Press.
- Gaudin C, White DJ, Boylan N, Breen J, Brown T, De Catania S, Hortin P, 2009. A wireless high-speed data acquisition system for geotechnical centrifuge model testing. *Measurement Science and Technology*, 20(9). <https://doi.org/10.1088/0957-0233/20/9/095709>
- Gebhard L, Mata-Falcón J, Anton A, Dillenburger B, Kaufmann W, 2021. Structural behaviour of 3D printed concrete beams with various reinforcement strategies. *Engineering Structures*, 240, 112380. <https://doi.org/10.1016/j.engstruct.2021.112380>
- Geotechnical Observations Ltd., Measurand Inc., 2018. *ShapeArray*
- Gomez JS, Ardila N, Chalaturnyk RJ, Zambrano-Narvaez G, 2017. Reservoir Geomechanical Properties Characterization of 3D Printed Sandstone. In: *Poromechanics VI*. American Society of Civil Engineers, Paris, France, pp 952–960.
- Gomez JS, Chalaturnyk RJ, Zambrano-Narvaez G, 2019. Experimental Investigation of the Mechanical Behavior and Permeability of 3D Printed Sandstone Analogues Under Triaxial Conditions. *Transport in Porous Media* 129:541–557 <https://doi.org/10.1007/s11242-018-1177-0>
- Gupta R, Salager S, Wang K, Sun W, 2019. Open-source support toward validating and falsifying discrete mechanics models using synthetic granular materials—Part I: Experimental tests with particles manufactured by a 3D printer. *Acta Geotechnica*, 14(4), 923-937. <https://doi.org/10.1007/s11440-018-0703-0>
- Gutiérrez-Oribio D, Tzoetopoulos G, Stefanou I, Plestan F, 2022. Earthquake control: an emerging application for robust control. Theory and experimental tests. <https://arxiv.org/abs/2203.00296>
- Hafez A, Liu Q, Finkbeiner T, Alouhali RA, Moellendick TE, Santamarina JC, 2021. The effect of particle shape on discharge and clogging. *Scientific reports*, 11(1), 1-11. <https://doi.org/10.1038/s41598-021-82744-w>
- Hanaor D, Gan Y, Revay M, Airey D, Einav I, 2016. 3d printable geomaterials. *Géotechnique* 66 (4): 323-332. <http://dx.doi.org/10.1680/jgeot.15.P.034>
- Hanaor DA, Ghadiri M, Chrzanowski W, Gan Y, 2014. Scalable surface area characterization by electrokinetic analysis of complex anion adsorption. *Langmuir*, 30(50), 15143-15152. <https://doi.org/10.1021/la503581e>
- Head D, Vanorio T, 2016. Effects of changes in rock microstructures on permeability: 3-D printing investigation: Permeability Of Printed Microstructures. *Geophys. Res. Lett.* 43:7494–7502. <https://doi.org/10.1002/2016GL069334>
- Higo Y, Lee CW, Doi T, Kinugawa T, Kimura M, Kimoto S, Oka F, 2015. Study of dynamic stability of unsaturated embankments with different water contents by centrifugal model tests. *Soils and Foundations*, 55(1), 112–126. <https://doi.org/10.1016/j.sandf.2014.12.009>
- Hubs <https://www.hubs.com/fr/guides/impression-3d/> accessed on 13/01/2022.
- Hull C, 2013. [Take 5: Q&A with Chuck Hull, Co-Founder, 3D Systems | IndustryWeek](https://www.IndustryWeek.com/2013/05/05/3d-systems-q-a-with-chuck-hull-co-founder/) (accessed on 19/01/2022)
- Ishibashi T, Fang Y, Elsworth D, Watanabe N, Asanuma H, 2020. Hydromechanical properties of 3D printed fractures with controlled surface roughness: Insights into shear-permeability coupling processes. *Int. J. Rock Mechanics and Mining Sciences* 128, 104271. <https://doi.org/10.1016/j.ijrmms.2020.104271>
- Ishutov S, Hasiuk FJ, Harding C, Gray JN, 2015. 3D printing sandstone porosity models. *Interpretation* 3: SX49–SX61. <https://doi.org/10.1190/INT-2014-0266.1>
- ISO 17296-2, 2015. Additive manufacturing- general principles. Part2 : overview of process categories and feedstock.8 p
- Jaber J, 2020. Application of additive manufacturing to the physical modeling of joints and rock masses, by experimental and numerical approaches. (in French). PhD thesis, Université de Lorraine, <http://theses.fr/2020LORR0071>
- Jaber J, Conin M, Deck O, Moumni M, Godard O, Kenzari S, 2020. Investigation of the Mechanical Behavior of 3D Printed Polyamide-12 Joints for Reduced Scale Models of Rock Mass. *Rock Mechanics and Rock Engineering* 53, 2687–2705. doi [10.1007/s00603-020-02064-9](https://doi.org/10.1007/s00603-020-02064-9)
- Jiang C, Zhao GF, 2015. A Preliminary Study of 3D Printing on Rock Mechanics. *Rock Mechanics and Rock Engineering* 48:1041–1050. <https://doi.org/10.1007/s00603-014-0612-y>
- Jiang C, Zhao G-F, Zhu J, et al., 2016a. Investigation of Dynamic Crack Coalescence Using a Gypsum-Like 3D Printing Material. *Rock Mechanics and Rock Engineering* 49:3983–3998. <https://doi.org/10.1007/s00603-016-0967-3>
- Jiang Q, Feng X, Gong Y, et al., 2016b. Reverse modelling of natural rock joints using 3D scanning and 3D printing. *Computers and Geotechnics* 73:210–220. <https://doi.org/10.1016/j.compgeo.2015.11.020>
- Jiang Q, Feng X, Song L, et al., 2016c. Modeling rock specimens through 3D printing: Tentative experiments and prospects. *Acta Mechanica Sinica* 32:101–111. <https://doi.org/10.1007/s10409-015-0524-4>
- Ju Y, Wang L, Xie H, et al., 2017. Visualization and Transparentization of the Structure and Stress Field of Aggregated Geomaterials Through 3D Printing and Photoelastic Techniques. *Rock Mech Rock Eng* 50:1383–1407. <https://doi.org/10.1007/s00603-017-1171-9>
- Ju Y, Xie H, Zheng Z, et al., 2014. Visualization of the complex structure and stress field inside rock by means of 3D printing technology. *Chinese Science Bulletin* 59:5354–5365. <https://doi.org/10.1007/s11434-014-0579-9>
- Kittu A, Watters M, Cavarretta I, Bernhardt-Barry ML, 2019. Characterization of additive manufactured particles for DEM validation studies. *Granular Matter*, 21(3), 1-15. <https://doi.org/10.1007/s10035-019-0908-4>

- Lau BH, 2015. Cyclic behaviour of monopile foundations for offshore wind turbines in clay. PhD. Thesis, University of Cambridge. <https://doi.org/10.17863/CAM.14093>
- Laverne F, Segonds F, Dubois P, 2018. Additive manufacturing. General Principles. Techniques de l'Ingénieur EBM 7017v2-1. 19p
- Lee JS, Guimaraes M, Santamarina JC, 2007. Micaceous sands: Microscale mechanisms and macroscale response. *Journal of Geotechnical and Geoenvironmental Engineering*, 133(9), 1136-1143. [https://doi.org/10.1061/\(ASCE\)1090-0241\(2007\)133:9\(1136\)](https://doi.org/10.1061/(ASCE)1090-0241(2007)133:9(1136))
- Lehners C, Wittorf N, 2004. Verwendung Von Blähton Als Leichtbaustoff Beim Straßenbau Auf Wenig Tragfähigem Untergrund, Erfahrungsbericht Über Durchgeführte Baumaßnahmen, Fibo ExClay Deutschland GmbH, Lübeck, Alemania.
- Li J, Gu Y, 2005. Coalescence of oil-in-water emulsions in fibrous and granular beds. *Separation and Purification Technology*, 42(1), 1–13. <https://doi.org/10.1016/j.seppur.2004.05.006>
- Liu P, Ju Y, Ranjith PG, et al., 2016. Visual representation and characterization of three-dimensional hydrofracturing cracks within heterogeneous rock through 3D printing and transparent models. *Int J Coal Sci Technol* 3:284–294. <https://doi.org/10.1007/s40789-016-0145-y>
- Maghsoudloo A, Askarinejad A, de Jager RR, Molenkamp F, Hicks MA, 2021. Large-scale physical modelling of static liquefaction in gentle submarine slopes. *Landslides*. Oct;18(10):3315-35.
- Margerit B, Weisz-Patrault D, Ravi-Chandar K, Constantinescu A, 2020. Tensile and ductile fracture properties of as-printed 316L stainless steel thin walls obtained by directed energy deposition. *Additive Manufacturing*, Elsevier. hal-03042512 <https://doi.org/10.1016/j.addma.2020.101664>
- Mathavan GN, Viraraghavan T, 1992. Coalescence/filtration of an oil-in-water emulsion in a peat bed. *Water Research*, 26(1), 91–98. [https://doi.org/10.1016/0043-1354\(92\)90116-L](https://doi.org/10.1016/0043-1354(92)90116-L)
- Matsumura S, Kobayashi T, Mizutani T, Bathurst R, 2017. Manufacture of Bonded Granular Soil Using X-Ray CT Scanning and 3D Printing. *Geotechnical Testing Journal* 40(6): 1000-1010.
- Ministerio de Fomento, 2008. EHE-08 (Instrucción del Hormigón Estructural) Madrid, Ministerio de Fomento, Secretaría General Técnica.
- Miskin MZ, Jaeger HM, 2013. Adapting granular materials through artificial evolution. *Nature materials*, 12(4), 326-331. <https://doi.org/10.1038/NMAT3543>
- Mitchell JK, 1967. Fundamentals of soil behaviour. New York: Wiley.
- Osinga S, Zambrano-Narvaez G, Chalaturnyk R, 2015. Study of geomechanical properties of 3D printed sandstone analogue. In: 49th U.S. Rock Mechanics/Geomechanics Symposium (ARMA-2015-547), San Francisco, CA.
- Pearson A, 2022. 3D printing history. <https://www.stratasys.com/explore/article/3d-printing-history> (accessed on 13/01/2022).
- Pegna J, 1997. Exploratory investigation of solid freedom construction. *Automation in Construction*, vol.5, n°5, 427-437. [https://doi.org/10.1016/S0926-5805\(96\)00166-5](https://doi.org/10.1016/S0926-5805(96)00166-5)
- Perrot A, 2019. 3D printing of concrete. State of the art and challenges of the digital construction revolution. ISTE/Wiley. ISBN : 9781786303417
- Phillips NS, Stallebrass SE, Goodey RJ, Jefferis SA, 2014. Test development for the investigation of soil disaggregation during slurry tunnelling. *Proceedings of the Eighth International Conference on Physical Modelling in Geotechnics (ICPMG 2014)*, Perth, Australia, 2: 979–984. <https://openaccess.city.ac.uk/id/eprint/8050/>
- Pinet É, 2009. Fabry-Pérot fiber-optic sensors for physical parameters measurement in challenging conditions. *Journal of sensors* (2). <https://doi.org/10.1155/2009/720980>
- Pol A, Artoni R, Richard P, Nunes da Conceição PR, Gabrieli F, 2022. Kinematics and shear-induced alignment in confined granular flows of elongated particles, submitted.
- Poullain P, Paquet E, Garnier S, Furet B, 2018. On site deployment of 3D printing for the building construction. The case of Yhnova™. *MATEC Web of Conferences* 163, 01001 https://doi.org/10.1051/mateconf/201816301001_MATBUD'2018
- Primkulov B, Chalaturnyk J, Chalaturnyk R, Zambrano Narvaez G, 2017. 3D Printed Sandstone Strength: Curing of Furfuryl Alcohol Resin-Based Sandstones. *3D Printing and Additive Manufacturing* 4:149–156. <https://doi.org/10.1089/3dp.2017.0032>
- Pua L, Caicedo B, Castillo D, Caro S, 2018. Development of a 3D clay printer for the preparation of heterogeneous models. In *Physical Modelling in Geotechnics* (McNamara et al. (eds)). CRC Press, London, UK, vol. 1, pp. 155–162.
- Pua L-M, Caicedo B, 2020. Reproducing the inherent variability of soils using a three-dimensional printer. *Int. J. Physical Modelling in Geotechnics* 21(6). <https://doi.org/10.1680/jphmg.20.00006>
- Rashad AM, 2018. Lightweight expanded clay aggregate as a building material—An overview, *Constr. Build. Mater.* 170, 757–775. <https://doi.org/10.1016/j.conbuildmat.2018.03.009>
- Ritter S, DeJong MJ, Giardana G, Mair RJ, 2018. 3D printing of masonry structures for centrifuge modelling. *Physical Modelling in Geotechnics – McNamara et al. (Eds) Taylor & Francis Group, London, ISBN 978-1-138-34419-8.* 449-454.
- Russell AR, 2014. How water retention in fractal soils depends on particle and pore sizes, shapes, volumes and surface areas. *Géotechnique*, 64(5), 379-390. <https://doi.org/10.1680/geot.13.P.165>
- Saftner DA, Hryciw RD, Green RA, Lynch JP, Michalowski RL, 2008. The use of wireless sensors in geotechnical field applications. *Proceedings of the 15th Annual Great Lakes Geotechnical/Geoenvironmental Conference*, 9(5).
- Sarda D, Choonia HS, Sarode DD, Lele SS, 2009. Biocalcification by *Bacillus pasteurii* urease: a novel application". *Journal of Industrial Microbiology and Biotechnology*, Volume 36, Issue 8, 1 Aug., Pages 1111–1115, <https://doi.org/10.1007/s10295-009-0581-4>
- Schaller FM, Weigel RF, Kapfer SC, 2016. Densest local structures of uniaxial ellipsoids. *Physical Review X*, 6(4), 041032. <https://doi.org/10.1103/PhysRevX.6.041032>
- Schroth MH, Istok JD, Ahearn SJ, Selker JS, 1996. Characterization of Miller-similar silica sands for laboratory hydrologic studies. *Soil Science Society of America Journal*, 60(5), 1331–1339. <https://doi.org/10.2136/sssaj1996.03615995006000050007x>
- Sharafisafa M, Shen L, Xu Q, 2018. Characterisation of mechanical behaviour of 3D printed rock-like material with digital image correlation. *Int. J. Rock Mechanics and Mining Sciences* 112, 122–138. <https://doi.org/10.1016/j.ijrmms.2018.10.012>
- Shin H, Santamarina JC, 2013. Role of particle angularity on the mechanical behavior of granular mixtures. *Journal of Geotechnical and Geoenvironmental Engineering*, 139(2), 353-355. [https://doi.org/10.1061/\(ASCE\)GT.1943-5606.0000768](https://doi.org/10.1061/(ASCE)GT.1943-5606.0000768)
- Sinha SK, Kutter BL, Wilson DW, Carey T, Ziotopoulou K, 2021. *Use of Photron cameras and TEMA software to measure 3D displacements in*

centrifuge tests.

- Song L, Jiang Q, Shi Y-E, Feng X-T, Li Y, Su F, Liu C, 2018. Feasibility Investigation of 3D Printing Technology for Geotechnical Physical Models: Study of Tunnels. *Rock Mechanics and Rock Engineering* (2018) 51:2617–2637, <https://doi.org/10.1007/s00603-018-1504-3>
- Soundararajan B, Sofia D, Barletta D, Poletto M, 2021. Review on modeling techniques for powder bed fusion processes based on physical principles, *Additive Manufacturing*, Vol.47, <https://doi.org/10.1016/j.addma.2021.102336>.
- Stathas D, Xu L, Wang JP, Ling HI, Li L, 2018. Concave segmental retaining walls. In *Physical Modelling in Geotechnics* (McNamara A, Divall S, Goodey R, Taylor N, Stallebrass S and Panchal J (eds)). CRC Press, London, UK, vol. 2, pp. 1457-1462. In: 9th Int. Conf. Phys. Modelling Geotechnics. London
- Stratasys. <https://www.stratasys.com/explore/blog/2020/3d-printing-faq> (accessed on 13/01/2022)
- Stringer ME, Allmond JD, Proto CJ, Wilson DW, Kutter BL, 2014. Evaluating the response of new pore pressure transducers for use in dynamic centrifuge tests. *Physical Modelling in Geotechnics - Proceedings of the 8th International Conference on Physical Modelling in Geotechnics 2014, ICPMG 2014, 1*, 345–351. <https://doi.org/10.1201/b16200-43>
- Su YF, Lee SJ, Sukumaran B, 2020. Influence of particle morphology simplification on the simulation of granular material behavior. *Granular Matter* 22:19 <https://doi.org/10.1007/s10035-019-0987-2>
- Suzuki A, Li K, Horne RN, 2017. Potential Utilizations of 3D Printed Fracture Network Model. *Proceedings, 42st Workshop on Geothermal Reservoir Engineering*, Stanford University, Stanford, CA.
- Suzuki A, Sawasdee S, Makita H, Hashida T, Li K, Horne, RN, 2016. Characterization of 3D printed fracture networks. 17- *Proceedings, 41st Workshop on Geothermal Reservoir Engineering*, Stanford University, Stanford, CA.
- Taylor H, Osullivan C, Sim WW, Carr SJ, 2017. Sub-particle-scale investigation of seepage in sands. *Soils and Foundations*, 57(3), 439–452. <https://doi.org/10.1016/j.sandf.2017.05.010>
- Torquato S, Jiao Y, 2009. Dense packings of the Platonic and Archimedean solids. *Nature*, 460(7257), 876-879. <https://doi.org/10.1038/nature08239>
- Ueda K, Sawada K, Wada T, Tobita T, Iai S, 2019. Applicability of the generalized scaling law to a pile-inclined ground system subject to liquefaction-induced lateral spreading. *Soils and Foundations*, 59(5), 1260–1279. <https://doi.org/10.1016/j.sandf.2019.05.005>
- Ultimaker, 2022. <https://ultimaker.com/fr/learn/what-is-3d-printing> (accessed on 19/01/2022).
- Van Zeben JCB, Azúa-González CX, Alvarez Grima M, van't Hof C Askarinejad A, 2018. July. Design and performance of an electro-mechanical pile driving hammer for geo-centrifuge. In *Proc. Int. Conf. Phys. Mod. Geotech. (ICPMG 2018)* (pp. 469-473).
- Wanasinghe D, Aslani F, Ma G, 2022. Development of 3D printable cementitious composite for electromagnetic interference shielding. *Construction and Building Materials*, 317: 125960.
- Watters M, 2017. Feasibility of additive manufactured materials for use in geotechnical laboratory testing applications. PhD. Thesis, University of Arkansas. <https://scholarworks.uark.edu/etd/1973>
- Wei D, Wang Z, Pereira JM, Gan Y, 2021. Permeability of uniformly graded 3D printed granular media. *Geophysical Research Letters*, 48(5). <https://doi.org/10.1029/2020GL090728>
- White DJ, Take WA, 2002. GeoPIV: Particle Image Velocimetry (PIV) software for use in geotechnical testing.
- White DJ, Take WA, Bolton MD, 2003. Soil deformation measurement using particle image velocimetry (PIV) and photogrammetry. *Geotechnique*, 53(7), 619–631. <https://doi.org/10.1680/geot.2003.53.7.619>
- Wohlers Associates, 2019. Wohlers report 2019: 3D printing and additive manufacturing state of the industry
- Wohlers TT, Wohlers Associates, 2013. Wohlers report 2013: additive manufacturing and 3D printing state of the industry : annual worldwide progress report.
- XtreeE, 2017. X-Reef, in the Calanques national park. <https://xtreee.com/project/xreef/> (accessed on 26/01/2022).
- Xu C, Dou P, Du X, El Nagggar MH, Miyajima M, Chen S, 2020. Seismic performance of pile group-structure system in liquefiable and non-liquefiable soil from large-scale shake table tests. <https://doi.org/10.1016/j.soildyn.2020.106299>
- Zhou T, Zhu JB, 2018. Identification of a Suitable 3D Printing Material for Mimicking Brittle and Hard Rocks and Its Brittleness Enhancements. *Rock Mech Rock Eng*, 51:765–777 <https://doi.org/10.1007/s00603-017-1335-7>
- Zhou T, Zhu JB, Ju Y, Xie HP, 2019. Volumetric fracturing behavior of 3D printed artificial rocks containing single and double 3D internal flaws under static uniaxial compression. *Engng Fracture Mechanics* 205 190–204. <https://doi.org/10.1016/j.engfracmech.2018.11.030>
- Zhu JB, Zhou T, Liao ZY, Sun L, Li XB, Chen R, 2018. Replication of internal defects and investigation of mechanical and fracture behaviour of rock using 3D printing and 3D numerical methods in combination with X-ray computerized tomography. *Int. J. Rock Mechanics and Mining Sciences* 106 198–212. <https://doi.org/10.1016/j.ijrmms.2018.04.022>



GEOLAB